Texture Analysis and Physical Interpretation of Polarimetric SAR Data

Author
Xinping Deng

Thesis Advisor
Carlos López-Martínez

A thesis submitted to the Universitat Politècnica de Catalunya (UPC)
in partial fulfillment of the requirements for the degree of
DOCTOR OF PHILOSOPHY

Ph.D. program on Signal Theory and Communications
Remote Sensing Laboratory (RSLAB) Group
Barcelona, June 2016

Texture Analysis and Physical Interpretation of Polarimetric SAR Data
Thesis written by Xinping Deng

Ph.D. program on Signal Theory and Communications
This work has been supported by FPI/UPC Research Fellowship Program

献给我的父亲母亲：邓建桂，张元兰。

夫知有所待而后当，其所待者特未定也。
庸讵知吾所谓天之非人乎?
所谓人之非天乎?

——《庄子·大宗师》

The knowledge of a phenomenon awaits the confirmation of it
as correct on observations.
But the observations are not yet determined.
How do we know whether the knowledge is a true law or not?

from "Zhuangzi - Master"

Preface

The four years for the PhD in Universitat Politècnica de Catalunya is one of the most wonderful adventures in my journey of life. I really enjoy myself during this period in Barcelona. It couldn't go so smoothly without help from many people. As the thesis draws to a close, I would like to express my deep gratitude to them.

First I would like to thank the thesis advisor Carlos López-Martínez for offering me the opportunity to carry out this project. Carlos is very friendly. I appreciate his kind help to make my stay and the work comfortable. He is humorous as well. His little jokes are funny, always making the conversations and the meetings delightful. Undoubtedly Carlos is professional in SAR polarimetry. His knowledge in this field impresses me, and his insightful ideas inspire me a lot. It is a great pleasure to work with him.

I'm very lucky and grateful that I have met friends like Le Ren, Feifei, Tingting, Shanshan, Yanyan, Yuehan and Lisa. We have a nice time to taste delicious food from different places. Memories of the travels around Europe we made together are always the precious ones. I would like to thank Josema and Vanessa, and their little angel, An. It brings me a of joy being with them in the parks, in the cafeterias, or in the beach. Thanks also go to Eduard, Israel, Marc, Julio, Roselina, and David for maintaining the lab a pleasant space to work.

I would also like to take this opportunity to thank the people from Casa Bezalel, Fundació Institut Confuci de Barcelona, and Associació d'Estudiants i Investigadors Xinesos a Barcelona. It is enjoyable to celebrate the Chinese festivals, to organize outdoor activities, and many others with them.

At last, I want to thank my parents, Jiangui Deng and Yuanlan Zhang, as well as my sister, Li Deng, for always being there and providing support during this period of time.

Xinping Deng
Barcelona, June 2016

Acknowledgments

The author would like to acknowledge the following institutions and people:

- UPC (Universitat Politècnica de Catalunya) for providing the doctoral FPI fellowship (Ref. 305FPI-UPC) during the development of this thesis.
- MICINN (Ministerio de Ciencia e Innovación) under project TEC2011-28201-C02-01, and MINECO (Ministerio de Economía y Competitividad) with Project Code TIN2014-55413-C2-1-P for providing financial support to part of the research performed in the frame of this thesis.
- DLR (Deutsche Zentrum für Luft- und Raumfahrt e.V.) for the TerraSAR-X data provided in the frame of the DRA proposal MTH1971, ESA (European Space Agency) for the RADARSAT-2 data provided in the frame of the AgriSAR 2009 campaign, and JAXA (Japan Aerospace Exploration Agency) for the ALOS-2 data provided in the framework of the 4th ALOS Research Announcement for ALOS-2.
- Priv.-Doz. Dr. Andreas Reigber from the DLR for the F-SAR data, and NASA (National Aeronautics and Space Administration) for the UAVSAR data.

Abstract

This thesis is dedicated to the study of texture analysis and physical interpretation of polarimetric SAR data. As the starting point, a complete survey of the statistical models for polarimetric SAR data is conducted. All the models are classified into three categories: Gaussian distributions, texture models, and finite mixture models. The texture models, which assume that the randomness of the SAR data is due to two unrelated factors, texture and speckle, are the main subject of this study. The PDFs of the scattering vector and the sample covariance matrix in different models are reviewed.

Since many models have been proposed, how to choose the most accurate one for a test data is a big challenge. Methods which analyze different polarimetric channels separately or require a filtering of the data are limited in many cases, especially when it comes to high resolution data. In this thesis, the l_2-norms of the scattering vectors are studied, and they are found to be advantageous to extract statistical information from polarimetric SAR data. Statistics based on the l_2-norms can be utilized to determine what distribution the data actually follows.

A number of models are suggested to model the texture of polarimetric SAR data, and some are very complex. But most of them lack a physical explanation. The random walk model, which can be interpreted as a discrete analog of the SAR data focusing process, is studied with the objective to understand the data statistics from the point of view of scattering process. A simulator based on the random walk model is developed, where different variations in the scatterer types and scatterer numbers are considered. It builds a bridge between the mathematical models and underlying physical mechanisms.

It is found that both the mixture and the texture could give the same statistics such as log-cumulants of the second order and the third order. The two concepts, texture and mixture, represent two quite different scenarios. A further study was carried on to see if it is possible to distinguish them. Higher order statistics are demonstrated to be favorable in this task. They can be physically interpreted to distinguish the scattering from a single type of target from a mixture of targets.

Contents

List of Figures

List of Tables

Acronyms

BSA Backscattering Alignment

CHSP Complete Homogeneous Symmetric Polynomials

CLT Central Limit Theorem

CSA Canadian Space Agency

DLR German Aerospace Center

EM electromagnetic

ENL Equivalent Number of Looks

ESA European Space Agency

FSA Forward Scattering Alignment

GBSAR Ground Based SAR

GIG Generalized Inverse Gaussian

JAXA Japanese Aerospace Exploration Agency

JPL Jet Propulsion Laboratory

KS Kolmogorov-Smirnov

LFM Linear Frequency Modulation

MKS Mellin Kind Statistics

ML Maximum Likelyhood

MoM Method of Moment

NASA National Aeronautics and Space Administration

NICT National Institute of Information and Communications Technology

NIM Normalized Intensity Moment

PDF Probability Density Function

PolSAR Polarimetric SAR

PRF Pulse Repetition Frequency

PRI Pulse Repetition Interval

RNSS Radio Navigation Satellite Service

ROI Region Of Interest

RSLab Remote Sensing Laboratory

SAR Synthetic Aperture Radar

SIRV Spherically Invariant Random Vector

SLC Single Look Complex

SNR Signal to Noise Ratio

UPC Universitat Politècnica de Catalunya

Nomenclature

$\delta(x)$ Dirac function

$\Gamma(x)$ Gamma function

$\Gamma_d(x)$ Multivariate gamma function

$\psi^{(v)}(x)$ Polygamma function

$\psi_d^{(v)}(x)$ Multivariate extension of polygamma function

$B(a, b)$ Beta function

$g_v(x_1, x_2, \cdots)$ The combinatorial version of Faà di Bruno's formula

$I_v(z)$ Modified Bessel function of the first kind

$J_v(z)$ Bessel function of the first kind

$K_v(z)$ Modified Bessel function of the second kind

$M(a, b, z)$ Confluent hypergeometric function of the first kind, or KummerM function

$U(a, b, z)$ Confluent hypergeometric function of the second kind, or KummerU function

$W_{a,b}(z)$ Whittaker W function

${}_2F_1(a, b; c; z)$ Gauss hypergeometric function

$(\,\cdot\,)^*$ Conjugate

$(\,\cdot\,)^\dagger$ Transpose conjugate

$(\,\cdot\,)^T$ Transpose

arg Angle of complex numbers

$\mathrm{Cov}\{\cdot, \cdot\}$ Covariance

$\mathrm{E}\{\cdot\}$ Expectation

Im Imaginary part of complex numbers

Re Real part of complex numbers

$\mathrm{Tr}(\cdot)$	Matrix trace
$\mathrm{Var}\{\cdot\}$	Variance
κ_v	Log-cumulant of order v
j	Imaginary unit
m_v	Moment of order v
nim_v	Normalized intensity moment of order v
nm_v	Normalized moment of order v
$\mathbf{\Sigma}$	Covariance matrix
$\mathbf{C}_L$	Sample covariance matrix
$\mathbf{k}$	Scattering vector
$\mathbf{S}$	Scattering matrix
$\mathbf{T}$	Coherency matrix
$\mathbf{z}$	Gaussian distributed speckle vector
τ	Scalar texture parameter
d	Dimension of scattering vector
$I_{\mathbf{k}}$	Square of the l_2-norm
L	Number of looks

1

Chapter 1
Introduction

1.1 Motivation

Remote sensing is the acquisition of information about a distant object or phenomenon without direct contact with it. Human beings and many other animals may achieve this goal through their senses of sight, hearing or smell. However, they provide a very limited amount of information. This situation can be improved by exploiting the interaction with the matter of some propagated signal such as electromagnetic (EM) waves or sonic waves. Since World War I, a considerable effort has been devoted to this topic, and a large number of technologies have been developed for gathering additional data from our environment. Nowadays, the term remote sensing generally refers to a wide set of techniques dedicated to the collection information about different Earth features and their dynamics. This concept comprises the whole process of acquisition, processing and interpretation of data.

Early imaging sensors for remote sensing were camera or camera-like systems with detectors that were sensitive to either reflected solar radiation or thermal radiation emitted from the Earth's surface. Instruments measuring the radiation emitted or reflected by the target from an external source are called passive sensors. Although they are capable of providing fine spatial resolution and excellent multi-spectral details, passive sensors are inhibited by clouds and depend on solar illumination, thus limited to daylight observation. In contrast, systems having their own illumination source are called active sensors. They have the advantage of providing control over imaging factors such as power, frequency, and polarization, all of which are important to the extraction of target information [1].

However, active sensors employing microwaves usually suffer from poor spatial resolution. In order to obtain high-resolution images one has to resort either to an impractically long antenna or to very short wavelengths which makes the sensor contend with severe

attenuation in the atmosphere. Another way to achieve better resolution is signal processing. Synthetic Aperture Radar (SAR) is a technique to improve the resolution beyond the limitation of the physical antenna aperture via signal processing. The forward motion of actual antenna is used to 'synthesize' a very long antenna. The result is that SAR allows the possibility of using longer wavelengths and still achieving good resolution with antenna structures of reasonable size. This characteristic makes the SAR an extremely valuable instrument for space observation [2].

There is currently a great deal of interest in the use of polarimetry in SAR. It is known that the polarization states of the EM waves will change when they interact with the Earth's surface due to the index of permittivity, permeability, and other properties such as geometry of the observing targets. The change in polarization gives an insight to the underlying scattering mechanisms, and remote sensing tools exploiting this kind of information are known as Polarimetric SAR (PolSAR) instruments. Many PolSAR systems, including both airborne ones and spaceborne ones, have been successfully launched in the last 30 years. They provide sufficient data for a wide range of applications, such as land-use classification, soil moisture estimation, disaster monitoring, and so on. Different results reported in the literature have demonstrated the usefulness of polarimetry for the study and characterization of the Earth surface because of its ability to retrieve biophysical and geophysical information from the scene [3].

In most SAR or PolSAR systems, the size of a resolution cell is much larger than the wavelength. The measured signal is then a coherent addition of the echoes from all individual targets within that cell. Depending on the relative phases of each scattered wave, the coherent addition may be constructive or destructive, and it produces a salt-and-pepper appearance known as speckle over SAR images. Although the speckle is a real electromagnetic measure, from the point of view of an acquisition system, it is considered as noise since it can not be predicted accurately and contaminates the measure of the reflectivity. The useful information, therefore, must be extracted from the statistics of the data. Consequently, an accurate statistical model becomes very important to the extraction of target information.

Gaussian statistics for the radar returns have been frequently assumed [4, 5]. In moderate or low spatial resolution images, the number of targets in a resolution cell is large, according to the Central Limit Theorem (CLT), Gaussian statistics could give a proper approximation to the data distribution. However, as the spatial resolution improves, the analysis of real PolSAR images reveals that non-Gaussian models give a better representation, implying that processing algorithms based on such models should improve their performance [6–10]. In the last two decades, a considerable research effort has been dedicated to finding accurate and efficient non-Gaussian models for PolSAR data. The basic idea is to assume that the radar return is a product of two independent components, the speckle and the texture. The former is assumed to follow a complex Gaussian distribution, whereas the latter is a positive random variable modeling the variation of the radar cross section.

Let the texture be a scalar random variable obeying different distribution laws, the product scheme could result in a number of statistical models known as scalar texture models. They are found to be suitable in various scenes. The $\mathcal{K}$ distribution [6, 7], the $\mathcal{G}^0$ distribution [9], and the Kummer-$\mathcal{U}$ distribution [10, 11] are the ones studied extensively. The $\mathcal{K}$ distribution assumes that the texture variable follows a gamma distribution. It has

been proved to be useful in characterizing the distribution of echoes from various objects, including sea surface, forests, etc. In certain areas such as urban environment, the $\mathcal{G}^0$ distribution with a inverse gamma distributed texture variable has been demonstrated to give a more accurate representation. The Kummer-$\mathcal{U}$ distribution was recently proposed which models the texture fluctuation with a Fisher distribution with the capability to represent a large set of texture distributions. Other scalar texture models include the $\mathcal{W}$ distribution and the $\mathcal{M}$ distribution with beta and inverse beta distributed texture variable, respectively [12]. In addition, the Probability Density Function (PDF) of the texture random variable can be not explicitly specified. Texture variable is estimated for each pixel independently. This relaxes the "texture stationarity" condition required by the previous models [13].

If the electromagnetic wave sees different geometrical or dielectric properties of the target according to the wave polarization, and if those properties are spatially modulated, then the image texture should also be a function of polarization [14]. This implies that different texture parameters are required for different polarimetric channels. All these texture parameters make up a vector having the same size as the speckle component. Several models exploiting this idea are proposed in literature and they are referred to multi-texture models. For example, Lombardo et al. assume the texture parameters to follow the partially correlated gamma distribution [15–17], Khan et al. assume that the co-pol and cross-pol channels have independent textures that follow Generalized Inverse Gaussian (GIG) distributions [18], and in the work of Eltoft and Doulgeris [19–21], the texture parameters can be either independent or totally correlated, or co-pol texture parameters are identical but different from cross-pol ones.

With the currently operational spaceborne PolSAR sensors, including RADARSAT-2, TerraSAR-X and ALOS-2, high-quality images of the Earth's surface with meter resolution are available. The decrease of resolution cell dimension offers the opportunity to observe much smaller spatial features, which means exploring the structures in the images could be possible. Texture information, therefore, becomes more and more important in the analysis of these images. In order to represent the texture information accurately, statistical models with generality, robustness and low computation cost are expected. The models mentioned above could be employed, but some limitations are noticed. For example, many parameters are required to represent complex scenes, and most of those models lack a physical explanation. Thus, there is an need to create connections between the mathematical models and the scattering process.

Another way to model the statistical behavior of SAR data or PolSAR data is the so called finite mixture model [22–24], which assumes the data under analysis is a discrete mixture of different targets. This makes sense in certain scenes such as urban areas which usually consist of coherent targets like houses and roads, as well as distributed targets like trees and grass. The backscattering from the urban area represents a combination of different scattering mechanisms. Another example of mixtures is the forest area, which sometimes can be treated as a composite of bright clutters and dark ones, corresponding to the strong returns from the crowns of trees and the shadows behind them. Texture models have also been proved to be appropriate for forest areas in many reports. Therefore, whether the data should be treated as mixture or texture needs to be verified. Or saying in a different way, we have to discriminate the concept of the mixture from that of the texture.

To determine whether a statistical model is suitable for the data or not, some measurable and comparative statistics are required. The univariate Mellin Kind Statistics (MKS), also known as log-cumulants, was first suggested by Nicolas [25] to analyze the compounded distributions used to model single-channel SAR data, and later was extended to matrix variate case by Anfinsen et al. [26]. It is demonstrated that MKS are of great value to texture analysis of SAR data because contributions from the texture and the speckle can be separated. The Method of Moment (MoM) is also an important approach in statistical analysis of SAR data. For example, the normalized intensity moments are used as a measure of non-gaussianity by many authors [14, 27, 28]. Other tools for statistical analysis of PolSAR data include copulas which are employed to analyze the correlation between different polarimetric channels [29].

The MoM and the univariate MKS are applicable to single channel data. In the case of PolSAR data, different channels need to be considered separately, and the correlation information between polarimetric channels are usually discarded. The matrix variate MKS needs to be performed on sample covariance matrices. A multilook processing is required before calculating the data statistics, and information could be lost during this process. As the original data obtained by a PolSAR system is the scattering matrix, some methods extracting statistical information directly from scattering matrices or scattering vectors are necessary. Nevertheless, no effective tools to accomplish this task are found in the literature.

To summarize, although the statistics play an important role in PolSAR applications such as speckle filtering [30], segmentation [31], ground cover classification [32, 33], etc., there still exist many issues remaining to be solved in this field, with a few examples listed as follows:

- Is it possible to extract texture information from scattering vectors directly and avoid any filtering?
- What is the physical meaning of the statistical models? Or do they have any physical explanation?
- How to distinguish the texture and the mixture? And which model is better for the testing data?

Therefore, it is worthy of a further investigation. This PhD thesis is devoted to the study of statistical modeling and texture analysis of PolSAR data, with the goal of giving answers or solutions to the above questions.

1.2 Objectives of the thesis

The detailed objectives of this thesis are listed as follows.

- The first objective is to make a comprehensive survey of the statistical models for PolSAR data. In addition, a review of the methods employed to determine what distribution the data follows is requisite.

- How to compute statistics from scattering matrices or scattering vectors directly is the second objective. It is important to avoid analyzing each polarimetric channel separately, or using any filter when it comes to high spatial resolution data.

- Another objective is to find physical interpretations for different texture models, as many models are just the results of pure mathematical calculations. The random walk model, especially the multi-dimensional random walk model, will be investigated, because it provides an insight to the SAR data formation process. How to simulate PolSAR data under different circumstances also will be studied, as it is possible to verify different assumptions with simulated data.

- At last, the texture and the mixture represent two quite different scattering scenarios. Which model gives a true representation of the data needs to be clarified. Higher order statistics will be studied in order to see if they could offer an effective way to distinguish the texture from the mixture.

1.3 Structure of the thesis

This manuscript is divided into seven chapters that are described briefly in the following.

- Chapter 1 introduces the motivation of this thesis.

- Chapter 2 provides an overview of the preliminary knowledge. Some basic concepts of SAR imaging are introduced, with emphasis on the data formation process, which is the start point of the random walk model. Wave polarimetry and scattering polarimetry are also reviewed, as well as how to represent PolSAR data mathematically. In addition, the most advanced PolSAR sensors launched recently are introduced, of which the data are exploited in this thesis.

- The review of the state-of-the-art is given in Chapter 3. First, statistics of the fully developed speckle is detailed. Properties of the single look scattering vectors and the multilook sample covariance matrices are studied under the Gaussian assumption. Then, the concept of texture is explained, along with the widely studied texture models, including both the scalar texture models and the multi-texture models. At last, finite mixture models, which are widely used to analyze the heterogeneity of data, are introduced.

- In Chapter 4, a method computing statistics from the scattering vectors is proposed. It exploits the l_2-norm of the single look scattering vectors, thus considering all polarimetric channels together and avoiding any filtering of the data. The distribution of the l_2-norm is studied based on the product model. And statistics such as normalized moments and log-cumulants are also computed. Experiments using the l_2-norm for texture analysis are implemented on both simulated data and real SAR data. In that chapter, existing methods are also reviewed, including the Normalized Intensity Moment (NIM), and the log-cumulants in both cases of univariate and matrix variate.

- In Chapter 5, the random walk model is studied with the objective of finding physical explantions of texture models. The two-dimensional random walk is introduced first, which leads to the Gaussian statistics or $\mathcal{K}$ distribution by changing the distributions of scatter number. Then, a PolSAR data simulator based on the multi-dimensional random walk is detailed. Algorithms on how to simulate different scatterer types and scatterer numbers are given, as well as mixtures of targets. Experimental results on both simulated data and real SAR data are shown at the end of that chapter.
- Chapter 6 details the method on how to compute the log-cumulants of the finite mixture model. A comparison between the log-cumulants of finite mixture model with log-cumulants of texture models is drawn, which leads to an important finding that can be employed to distinguish the texture from mixture. The method is tested on both simulated data and real SAR data.
- The conclusions are summarized in Chapter 7.

2

Chapter 2

SAR Polarimetry and PolSAR Systems

SAR systems are widely used in remote sensing nowadays. It was started in 1951 by Carl Wiley, and the first focused image was obtained at the Michigan University in 1958 [34]. The capability of SAR sensors to image Earth both during the day and the night for almost all weather conditions becomes more and more attractive in Earth monitoring. As an active remote sensing tool, SAR has the advantage of providing control over such factors as power, frequency, phase, polarization, incident angle, spatial resolution and swath width, all of which are important when designing an operational system for the extraction of target information. The ability of radar to penetrate persistent cloud cover have produced improvements in newscasts, forecasts and climatologist analyses because diurnal and seasonal variances can be monitored [1].

By collecting a near-simultaneous and mutually coherent versions of the scattered field in a minimum basis set of polarizations, PolSAR instruments allow for a more complete characterization of the targets' scattering characteristics [1]. PolSAR systems measure the EM polarimetric information of the scattered wave in addition to the backscattered power, offering the surplus advantage of exploiting different responses of scatterers to different polarizations of the incident wave [3]. PolSAR data, as a result, can lead to a significant improvement in information retrieving algorithms by adding knowledge about scattering mechanisms.

Airborne PolSAR sensors were firstly developed due to their flexibility and lower cost, which helped later on the planning of much more expensive satellite missions. In 1985, the Jet Propulsion Laboratory (JPL) successfully implemented the first practical fully polarimetric AIRSAR at L-band that is mounted aboard a modified National Aeronautics

and Space Administration (NASA) DC-8 aircraft. After that, many airborne PolSAR systems flourished. Systems with higher spatial resolution such as E-SAR were developed [3]. The spaceborne PolSAR era started in 1994, when the SIR-C/X-SAR was successfully launched onboard the Space Shuttle. Recently, several fully PolSAR satellites operating at different frequencies have been successfully launched. They provide sufficient data for remote sensing the Earth's environment, such as hazard monitoring, soil moisture estimation, forest sensing, and so on [3].

This chapter provides an overview of SAR imaging and SAR polarimetry. The remainder is organized as follows. First, some basic concepts of a SAR are introduced, with emphasis on the data formation process, which is the core concept of the random walk model detailed in later chapters. Then, SAR polarimetry is reviewed, as well as PolSAR data descriptors are introduced. At last, a general review of the most advanced PolSAR sensors is also provided, including spaceborne, airborne and ground based instruments. All the SAR data used in this manuscript are from these systems.

2.1 SAR Imaging

Illustration of a typical stripmap SAR is shown in Fig. 2.1. The antenna is mounted on a platform such as an aircraft that travels along a flight path at a height of H with velocity v. It illuminates a certain area, known as footprint, on the ground as the aircraft moves. The flight path is referred to as the azimuth direction, or along-track direction. The across-track dimension perpendicular to the flight path is called slant range direction, or simply range direction, and the ground range is its projection on Earth [1–3, 34]. A SAR makes observation in both the range direction and the azimuth direction, resulting into a two-dimensional measurement.

When a radar works, the antenna illuminates an area by transmitting EM pulses of duration τ_p repeatedly at a given interval, Pulse Repetition Interval (PRI). Each pulse travels to the target area and illuminates targets at that location. The same antenna collects the reflected return echos during the pulse interval. By precisely measuring the properties such as amplitude and phase of the reflected wave, as well as the time delay, the radar is able to extract certain information of the reflecting object at a specific distance. SAR "works" because the radar pulse travels to and from the target at the speed of light, which is much faster than the speed of the aircraft [1].

The angular spread of the radar beam is determined by the antenna size. Suppose that the antenna has a length of L_a and a width of W_a, the half-power beam width in the horizontal and vertical directions are given by [34]

$$\theta_H = \frac{\lambda}{L_a}, \quad \theta_V = \frac{\lambda}{W_a} \tag{2.1}$$

where λ is the wavelength of the transmitted signal. Let γ_0 denote the look angle and R_0 the slant range to the midpoint of the footprint, the ground swath width then can be approximated by

$$W_g \approx \frac{\theta_V R_0}{\cos\gamma_0} = \frac{\lambda R_0}{W_a \cos\gamma_0}. \tag{2.2}$$

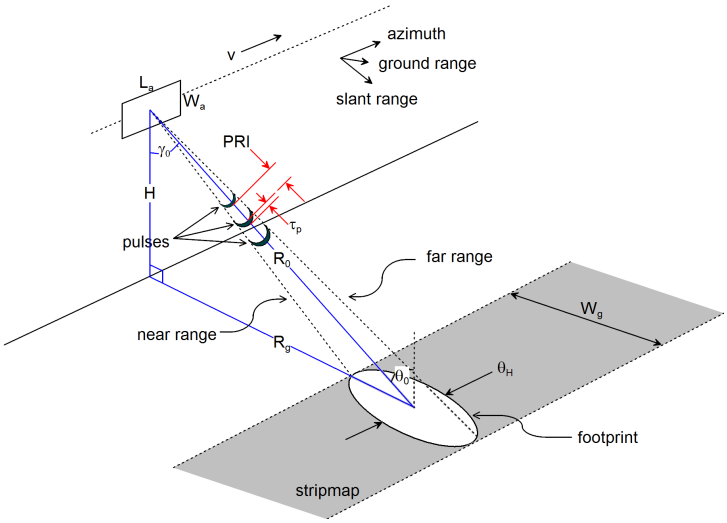

Figure 2.1: SAR imaging geometry.

An important parameter to evaluate the performance of a SAR instrument is the spatial resolution, both in the range direction and in the azimuth direction. The range resolution of a radar system is its ability to distinguish two objects separated by some minimum distance in that direction. As shown in Fig. 2.2b (top), two targets can be discriminated only if the time delay of their echos is larger than the pulse length, that is, $\Delta t \geq \tau_p$. The range resolution, therefore, is given by

$$\delta_r = \frac{c\tau_p}{2} \tag{2.3}$$

with c denoting the speed of light. The value is proportional to the pulse length, implying that a short pulse results in better resolution. Unfortunately utilizing short pulse decreases the average power, which degrades radar signal detectability and measurement precision [2, 34]. Since the average transmitted power is directly linked to the receiver Signal to Noise Ratio (SNR), it is desired to increase the pulse width while simultaneously maintaining adequate range resolution. This can be accomplished by using pulse compression technique, such as Linear Frequency Modulation (LFM) or chirp, that allows achieving the average transmitted power of a relatively long pulse, while obtaining the range resolution corresponding to a short pulse. A linear chirp waveform can be described by

$$s(t) = A \exp\left[j2\pi\left(f_c t + \frac{\beta t^2}{2}\right)\right], \quad -\frac{\tau_p}{2} \leq t \leq \frac{\tau_p}{2} \tag{2.4}$$

where A is the amplitude, f_c is the carrier frequency and β is the chirp rate. The instantaneous frequency is $f_c + \beta t$, and the bandwidth is given by $B_t = \beta\tau_p$. The echo from a point target at distance R will be a replica of the transmitted pulse with a time delay $\tau = 2R/c$. If we apply a matched filter to the received echo, the output turns out to be [35]

$$g(t) = A\tau_p \exp(j2\pi f_c t) \exp\left(-\frac{j4\pi R}{\lambda}\right) \mathrm{sinc}(\pi B_t(t-\tau)), \quad -\frac{\tau_p}{2} \leq t-\tau \leq \frac{\tau_p}{2} \tag{2.5}$$

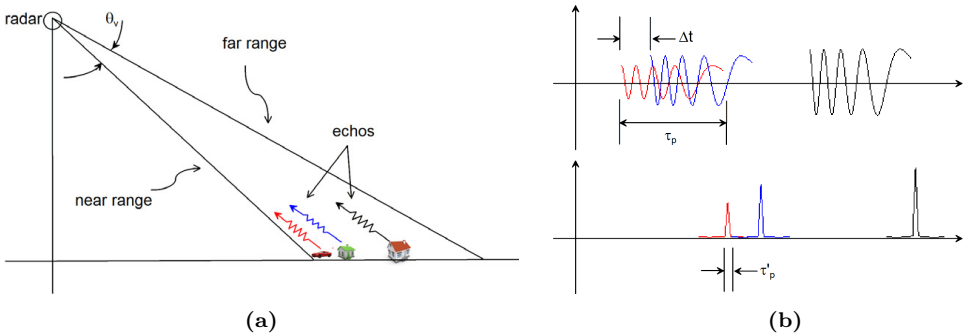

Figure 2.2: Illustration of range resolution. (a) Geometry of target scattering. (b) The received echo (top) and the result after pulse compression (bottom). If two targets are too close, the received echo will be overlapped (the red echo and the blue echo for example), meaning that the radar system will treat the echos as from one target. But after pulse compression, the overlapped echos are separated, then the radar is able to determine the ranges using the processed echos.

where $\mathrm{sinc}(x) = \sin x/x$. The length of the main lobe of this processed echo is given by $\tau_p' = 1/B_t$. A proper value for β could lead to $\tau_p' < \tau_p$. And an instant consequence is that the overlapped long echos are "compressed" and can be separated (see Fig. 2.2b). The targets then could be distinguished if we exploit the processed echo instead of the received echo, the range resolution in this case is given by

$$\delta_r = \frac{c}{2B_t}. \tag{2.6}$$

Azimuth resolution is the minimum distance on the ground in the direction parallel to the flight path at which two targets can be separately imaged. Two targets located at same slant range can be resolved only if they are not in the radar beam at the same time. The azimuth resolution of a conventional radar is determined by the width of the footprint [34]

$$\delta_a \approx R_0\theta_H = \frac{R_0\lambda}{L_a}. \tag{2.7}$$

The azimuth resolution is dependent on aperture length. In order to improve resolution, a longer antenna needs to be employed. However, the constructing and maintaining of a long antenna is impractical, especially for spaceborne sensors which are at a high altitude. To handle this problem, SAR instruments use a virtual large antenna or a virtual antenna of large "aperture" [34]. As the aircraft moves along the flight path, a target under illumination has different angles to the radar at different times, which gives rise to a changing frequency in the returns. A very narrow equivalent azimuth main lobe can be synthesized by exploiting the frequency history via signal processing techniques. The end result is as if an antenna of great length (up to a kilometer) is generated. Suppose that the distance from the radar to a target in the azimuth direction is x (see Fig. 2.3), the squint distance can be approximated by [34]

$$R \approx R_0 + \frac{x^2}{2R_0}, \quad -\frac{R_0\theta_H}{2} \le x \le \frac{R_0\theta_H}{2}. \tag{2.8}$$

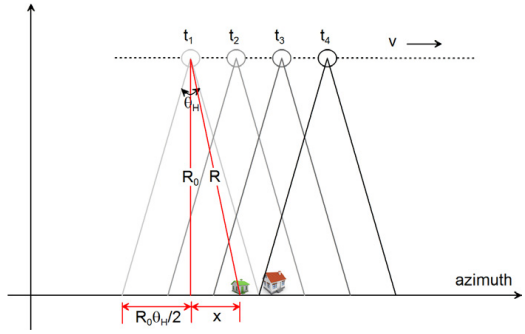

Figure 2.3: Illustration of azimuth resolution.

Substituting it into (2.5) yields

$$g(t,x) = A\tau_p \exp(j2\pi f_c t) \exp\left(-\frac{j4\pi R_0}{\lambda}\right) \exp\left(-\frac{j2\pi x^2}{\lambda R_0}\right) \mathrm{sinc}(\pi B(t-\tau)). \tag{2.9}$$

As the aircraft moves, the relative distance x changes and a Doppler frequency shift will occur in the echos from the same target. Its effect approximates to a linear chirp with chirp rate $2/\lambda R_0$. The bandwidth is given by $B_x = 2\theta_H/\lambda$. Applying a matched filter to the result again, we have the output waveform as

$$g(t,x) = A\tau_p \exp(j2\pi f_c t) \exp\left(-\frac{j4\pi R_0}{\lambda}\right) \mathrm{sinc}(\pi B_x x)\, \mathrm{sinc}(\pi B(t-\tau)) \tag{2.10}$$

and two targets can be resolved if they are located in the along-track direction of a distance greater than

$$\delta_a = \frac{1}{B_x} = \frac{L_a}{2}. \tag{2.11}$$

The signal described by (2.10) can be further demodulated to remove the carrier frequency, and the time variable can be converted to range distance, giving

$$g(r,x) = A\tau_p \exp\left(-\frac{j4\pi R_0}{\lambda}\right) \mathrm{sinc}\left(\frac{\pi x}{\delta_a}\right) \mathrm{sinc}\left(\frac{\pi r}{\delta_r}\right). \tag{2.12}$$

It is equivalent to a rectangular low-pass filter. By considering the complex reflectivity σ_s, a SAR image could be modeled as follows [34]:

$$S(r,x) = \int_{-\infty}^{\infty}\int_{-\infty}^{\infty} \sigma_s(t',x') g(r-r', x-x') dt' dx'. \tag{2.13}$$

A resolution cell in a SAR image is represented as the coherent sum of the responses from the whole cell. This is the core concept of the random walk model that will be detailed in Chapter 5.

2.2 SAR Polarimetry

Now let us consider the polarizations of the transmitted EM pulses. Polarimetry refers specifically to the vector nature of the EM waves. A PolSAR system generates EM

pulses at specified polarization states and transmits them to the Earth's surface. When the EM pulse impinges on a target, the polarization state changes due to the index of refraction, permittivity, magnetic permeability, and conductivity of the target as well as its geometry. The PolSAR system then measures the change in polarization of the backscattered pulse and extract target information [3]. Polarimetry provides a strong link to the physics of the scattering process, which allows the identification of distinct scattering mechanisms [3]. Consequently, radar polarimetry is becoming an indispensable technology in modern remote sensing. Wave polarimetry and scattering polarimetry are explained separately in the following sections.

2.2.1 Wave Polarimetry

The Maxwell's equations are the starting point to solve electromagnetic problems as they govern the generation and propagation of EM waves, as well as the interaction of these waves with matter. For EM sources in a non-conducting, lossless, isotropic media with electric permittivity ε and magnetic permeability μ, the formulation of the Maxwell's equations in differential form can be expressed as follows

$$\begin{aligned} \nabla \cdot \mathbf{D}(\mathbf{r}, t) &= \rho(\mathbf{r}, t) \\ \nabla \cdot \mathbf{B}(\mathbf{r}, t) &= 0 \\ \nabla \times \mathbf{E}(\mathbf{r}, t) &= -\frac{\partial \mathbf{B}(\mathbf{r}, t)}{\partial t} \\ \nabla \times \mathbf{H}(\mathbf{r}, t) &= \mathbf{J}(\mathbf{r}, t) + \frac{\partial \mathbf{D}(\mathbf{r}, t)}{\partial t} \end{aligned} \tag{2.14}$$

where $\mathbf{E}$ is the electric field, $\mathbf{B}$ is the magnetic field, $\mathbf{D} = \varepsilon\mathbf{E}$ is the electric displacement field, and $\mathbf{H} = \mathbf{B}/\mu$ is the magnetic field strength [36]. All of them are functions of the position $\mathbf{r}$ and the time t. EM energy comes from the current intensity $\mathbf{J}$ and the free change density ρ.

The electric field and the magnetic field described by (2.14) can be decoupled by raising their order. For source free media, i.e., $\rho = 0$ and $\mathbf{J} = 0$, the result takes the form

$$\nabla^2 \mathbf{\Phi} - \frac{1}{\varepsilon\mu} \frac{\partial^2 \mathbf{\Phi}}{\partial t^2} = 0 \tag{2.15}$$

where $\mathbf{\Phi}$ can be either $\mathbf{E}$ or $\mathbf{B}$. Equation (2.15) is usually referred as the wave equation, which has an infinite number of solutions [36]. Among those, one special solution is the constant amplitude monochromatic plane waves [36]. Considering a frequency modulation for the EM fields as described by (2.4), the plane waves can be written as

$$\begin{aligned} \mathbf{E} &= \mathrm{Re}\left\{\mathbf{E}_0 e^{-j\mathbf{k}\cdot\mathbf{r}} e^{j\theta(t)+\delta_\mathbf{r}}\right\} \\ \mathbf{B} &= \sqrt{\varepsilon\mu}\frac{\mathbf{k}}{|\mathbf{k}|} \times \mathbf{E} \end{aligned} \tag{2.16}$$

where $\mathbf{E}_0$ is the constant amplitude, $\delta_\mathbf{r}$ is the initial phase term, $\theta(t) = \omega t + \pi\beta t^2$ is the time dependence, and $\mathbf{k}$ is the propagating vector. The electric field $\mathbf{E}$ and magnetic field

B are perpendicular to each other. The wave propagates along the direction $\hat{\mathbf{k}}$ with wave number k:

$$\begin{aligned} k &= |\mathbf{k}| = \frac{2\pi}{\lambda} \\ \hat{\mathbf{k}} &= \frac{\mathbf{k}}{k} \end{aligned} \tag{2.17}$$

Equation (2.16) indicates that the electric field and magnetic field have similar forms. From now on, only the electric field will be considered, since the same analysis applies to both fields.

Let $\hat{\mathbf{h}}$ and $\hat{\mathbf{v}}$ denote the horizontal direction and the vertical direction respectively. The electric field may be represented in an orthogonal Cartesian basis $(\hat{\mathbf{h}}, \hat{\mathbf{v}}, \hat{\mathbf{z}})$ so that the direction of propagation $\hat{\mathbf{k}} = \hat{\mathbf{z}}$. The expression of the electric field given by (2.16) becomes

$$\mathbf{E} = \begin{bmatrix} E_h \\ E_v \end{bmatrix} = \begin{bmatrix} E_{0h}\cos(\theta(t) - kz + \delta_h) \\ E_{0v}\cos(\theta(t) - kz + \delta_v) \end{bmatrix}. \tag{2.18}$$

Let us consider the geometric locus by describing the electric field as a function of time at a particular point in space, saying $z = 0$. It can be shown that the field components E_h and E_v satisfy [3]

$$\left(\frac{E_h}{E_{0h}}\right)^2 + \left(\frac{E_v}{E_{0v}}\right)^2 - 2\frac{E_h E_v}{E_{0h}E_{0v}}\cos\delta = \sin^2\delta \tag{2.19}$$

where $\delta = \delta_h - \delta_v$. The above equation describes an ellipse that is called polarization ellipse, of which the shape depends neither on time nor on space position. The polarization ellipse defines the polarization state of an EM wave, that can be expressed as the so-called Jones Vector

$$\mathbf{E} = \begin{bmatrix} E_h \\ E_v \end{bmatrix} = \begin{bmatrix} E_{0h}e^{j\delta_h} \\ E_{0v}e^{j\delta_v} \end{bmatrix} \tag{2.20}$$

The polarization ellipse can be also characterized using three parameters as shown in Fig. 2.4:

1. The polarization amplitude A that can be obtained as

$$A = \sqrt{E_{0h}^2 + E_{0v}^2}. \tag{2.21}$$

2. Orientation or tilt angle $\phi \in \left[-\frac{\pi}{2}, \frac{\pi}{2}\right]$. This angel gives the orientation of the ellipse major axis respect to the horizontal direction. Its value is

$$\tan(2\phi) = \frac{2E_{0h}E_{0v}}{E_{0h}^2 - E_{0v}^2}\cos\delta \tag{2.22}$$

3. Ellipticity angle $\tau \in \left[-\frac{\pi}{4}, \frac{\pi}{4}\right]$. This angle represents the ellipse aperture in such a way that

$$|\sin(2\tau)| = \frac{2E_{0h}E_{0v}}{E_{0h}^2 + E_{0v}^2}|\sin\delta|. \tag{2.23}$$

   The sign of the ellipticity angle determines the sense in which the polarization ellipse is described: for $\tau < 0$ the polarization sense is right-handed whereas for $\tau > 0$ it is left-handed.

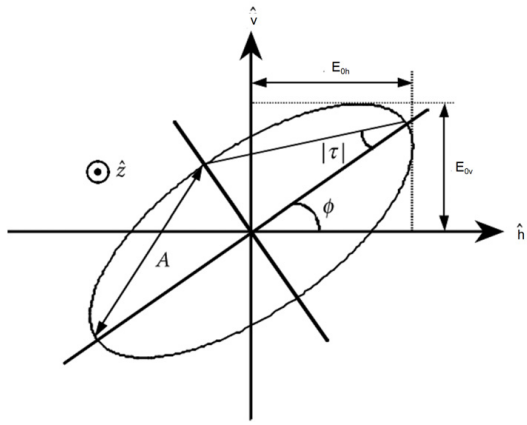

Figure 2.4: Polarization ellipse.

The two sets of field parameters, $\{E_{0h}, E_{0v}, \delta\}$ and $\{A, \phi, \tau\}$, are equivalent. The electric field given by (2.18) can be written as

$$\mathbf{E} = Ae^{j\alpha} \begin{bmatrix} \cos\phi & -\sin\phi \\ \sin\phi & \cos\phi \end{bmatrix} \begin{bmatrix} \cos\tau \\ j\sin\tau \end{bmatrix} \tag{2.24}$$

where α is the initial phase respect to the phase origin at $t = 0$.

One can identify some important particular polarization states by considering special values for the polarization ellipse parameters, including linear polarization state where $\delta = m\pi, m = 0, \pm1, \pm2, \ldots$, and circular polarization state with $\delta = m\pi/2, m = \pm1, \pm3, \ldots$ and $E_{0h} = E_{0v}$.

2.2.2 Scattering Polarimetry

One property that can characterize distant targets is the change of the polarization state that a target may induce to the incident field. Let the polarized incident wave and scattered wave be expressed as the Jones Vectors

$$\mathbf{E}^i = \begin{bmatrix} E_h^i \\ E_v^i \end{bmatrix} \quad \mathbf{E}^s = \begin{bmatrix} E_h^s \\ E_v^s \end{bmatrix} \tag{2.25}$$

It is possible to relate the incident and scattered wave by means of a 2×2 complex matrix [3]

$$\begin{bmatrix} E_h^s \\ E_v^s \end{bmatrix} = \frac{e^{-jkz}}{z} \begin{bmatrix} S_{hh} & S_{hv} \\ S_{vh} & S_{vv} \end{bmatrix} \begin{bmatrix} E_h^i \\ E_v^i \end{bmatrix} \tag{2.26}$$

where z is the distance between the target and the receiving antenna, and k is the wave number of the illuminating wave. The coefficient z^{-1} is produced by the spherical nature of the scattered wave. The phase factor e^{-jkz} represents the delay of the travel of the wave from the scatterer to the receiving antenna. The 2×2 transformation matrix is generally referred to as scattering matrix and denoted by $\mathbf{S}$. It characterizes the target

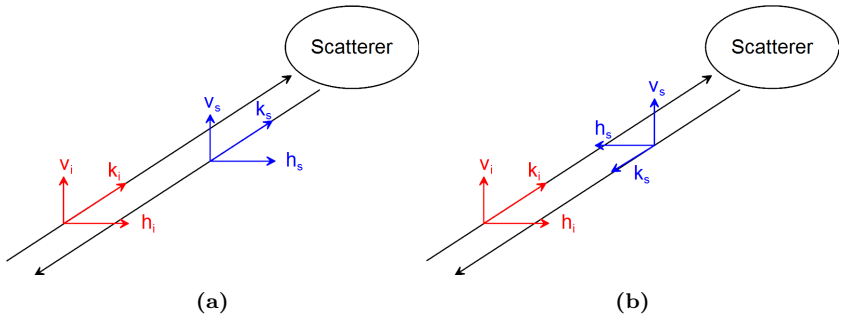

Figure 2.5: Scattering Coordinate Systems. (a) BSA. (b) FSA.

under observation with four complex-valued scattering coefficients. The diagonal elements of the scattering matrix receive the name "co-pol", since they relate the same polarization for the incident and the scattered fields. The off-diagonal elements are known as "cross-pol" terms as they relate orthogonal polarization states.

It is important to note that the definition of **S** depends on the coordinate systems. There are two principal conventions concerning the coordinate systems where the polarimetric scattering process can be considered: Forward Scattering Alignment (FSA) and Backscattering Alignment (BSA). In the FSA, the polarization states of the incident and the scattered wave are defined with respect to their propagation vectors, meaning that the coordinate systems are different since the propagation directions are different. In the BSA, the coordinate systems employed for both incident wave and scattered wave are the same, with respect to the wave radiated by the antenna. The difference lies in the way the coordinate system is selected to describe the polarization state of the scattered wave, as illustrated in Fig. 2.5. The FSA is usually used when the transmitter and the receiver are not placed at the same spatial location, for example, the bistatic radar measurements. In contrast, the BSA is often adopted in monostatic radar measurements, in which the transmitting and receiving antennas are collocated in space. Unless otherwise specified, the BSA is employed through all this manuscript. Nevertheless, the same scatterer matrices under FSA and BSA can be converted mutually using

$$\mathbf{S}_{FSA} = \begin{bmatrix} -1 & 0 \\ 0 & 1 \end{bmatrix} \mathbf{S}_{BSA} \tag{2.27}$$

The interaction between the EM waves with a reciprocal medium follows the vector reciprocity theorem, which states that if we transmit a polarization state P_A from position A, then the component polarized in the P_B direction at position B is equal to the P_A component of the scattered radiation when we illuminate the same object from B with polarization P_B [37]. The reciprocity theorem applies to ground targets generally. Although there exists a class of non-reciprocal backscatter problems, these are not common in the remote sensing of natural land and sea surface [37]. In the BSA coordinate system, the reciprocity theorem says that the cross-polar channels of the scattering matrix are equal, that is $S_{hv} = S_{vh}$. Therefore, there are only three independent complex coefficients required to characterize the scatter under observation. In this manuscript only the reciprocal medium is considered.

When the radar transmits a perfectly monochromatic wave and this wave reaches a fixed or stationary target, it results into a perfectly polarized scattered wave. The scattering process can be completely represented by the scattering matrix. This type of targets is referred to as point targets or coherent targets. Point targets have deterministic responses to the incident wave. Some important point targets, known as canonical bodies, are shown in Table 2.1 [3]. Canonical bodies are the basic elements making up a complex scene.

2.2.2.1 Scattering Vector

In many cases, it is more flexible to represent the scattering matrix as a vector which is known as scattering vector. The vectorization can be performed through [38]

$$\mathbf{k} = \frac{1}{2}\,\mathrm{Tr}(\mathbf{S}\boldsymbol{\Psi}) \tag{2.28}$$

where $\mathrm{Tr}(\cdot)$ is the matrix trace and $\boldsymbol{\Psi}$ is a 2×2 complex matrix from a basis set which are constructed as an orthonormal set under an Hermitian inner product. The lexicographic basis and Pauli basis are the most common ones in the context of radar polarimetry.

The lexicographic basis set consists of the straightforward lexicographic ordering of the elements of the scattering matrix. For a reciprocal target, it is defined as

$$\{\boldsymbol{\Psi}_l\} = \left\{ 2\begin{bmatrix}1 & 0\\ 0 & 0\end{bmatrix}, 2\sqrt{2}\begin{bmatrix}0 & 1\\ 0 & 0\end{bmatrix}, 2\begin{bmatrix}0 & 0\\ 0 & 1\end{bmatrix} \right\} \tag{2.29}$$

The scattering vector in this case can be expressed as

$$\mathbf{k}_l = \begin{bmatrix} S_{hh} \\ \sqrt{2}S_{hv} \\ S_{vv} \end{bmatrix} \tag{2.30}$$

The Pauli basis consists of the set of Pauli spin matrices usually employed in quantum mechanics

$$\{\boldsymbol{\Psi}_p\} = \left\{ \sqrt{2}\begin{bmatrix}1 & 0\\ 0 & 1\end{bmatrix}, \sqrt{2}\begin{bmatrix}1 & 0\\ 0 & -1\end{bmatrix}, 2\sqrt{2}\begin{bmatrix}0 & 1\\ 1 & 0\end{bmatrix} \right\} \tag{2.31}$$

The vectorization result under this basis set is known as Pauli scattering vector

$$\mathbf{k}_p = \frac{1}{\sqrt{2}}\begin{bmatrix} S_{hh} + S_{vv} \\ S_{hh} - S_{vv} \\ 2S_{hv} \end{bmatrix} \tag{2.32}$$

The selection of the basis to vectorize the scattering matrix depends on the final purpose of the vectorization itself. When studying the statistical behavior of the PolSAR data, the lexicographic basis is more convenient due to its simplicity. If the objective is the physical interpretation of the scattering coefficients, it is more reasonable to consider the Pauli basis. The first component in $\mathbf{k}_p$ can be interpreted as the single scattering from a sphere or plane surface, the second one represents a dihedral scattering, and the last one corresponds to an anti-symmetric helix-type scattering that transforms the incident wave into its orthogonal circular polarization state. The amplitudes of these components can be used to build a color code, as shown in Fig. 2.15 and Fig. 2.16. This representation of data is called Pauli decomposition [3] which is widely employed in the later chapters.

Table 2.1: Scattering Matrix of Point Canonical Bodies

Canonical Body	Diagram	**S**
Sphere	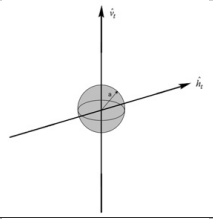	$\frac{a}{2}\begin{bmatrix}1 & 0\\ 0 & 1\end{bmatrix}$
Trihedral	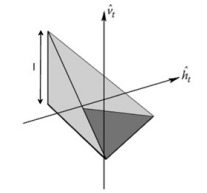	$\frac{kl^2}{\sqrt{12}\pi}\begin{bmatrix}1 & 0\\ 0 & 1\end{bmatrix}$
Dihedral	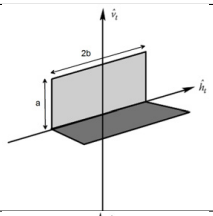	$\frac{kab}{\pi}\begin{bmatrix}1 & 0\\ 0 & -1\end{bmatrix}$
Dipol	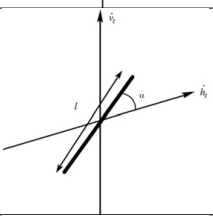	$\frac{k^2l^3}{3(\ln(4l/\alpha)-1)}\begin{bmatrix}\sin^2\alpha & -\sin\alpha\cos\alpha\\ -\sin\alpha\cos\alpha & \cos^2\alpha\end{bmatrix}$
Left-handed Helix	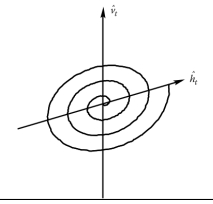	$\frac{1}{2}\begin{bmatrix}1 & j\\ j & -1\end{bmatrix}$
Right-handed Helix	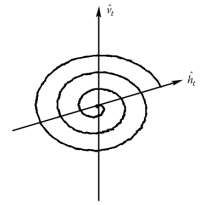	$\frac{1}{2}\begin{bmatrix}1 & -j\\ -j & -1\end{bmatrix}$

2.2.2.2 Covariance Matrix and Coherency Matrix

Targets under observation are commonly situated in a dynamically changing environment and are subjected to spatial and temporal variations, for example, forests affected by the wind and water surfaces in motion. Under this situation, despite the radar system transmits a perfectly polarized wave, the wave scattered by the target is partially polarized. The electric field vector does not longer describe an ellipse in the plane perpendicular to the propagation direction. Such scatterers are called distributed targets. The analysis of this type of targets can not be performed exactly by one target but a population of targets. More precisely, they are analyzed by introducing the concept of space and time varying stochastic processes, where the targets are described by the second order moments such as the polarimetric coherency or covariance matrices.

The covariance matrix is defined as the expectation of the outer product of the target vector with its transpose conjugate

$$\mathbf{C} = \mathrm{E}\{\mathbf{k}_l \mathbf{k}_l^\dagger\} = \begin{bmatrix} \mathrm{E}\{S_{hh}S_{hh}^*\} & \sqrt{2}\,\mathrm{E}\{S_{hh}S_{hv}^*\} & \mathrm{E}\{S_{hh}S_{vv}^*\} \\ \sqrt{2}\,\mathrm{E}\{S_{hv}S_{hh}^*\} & 2\,\mathrm{E}\{S_{hv}S_{hv}^*\} & \sqrt{2}\,\mathrm{E}\{S_{hv}S_{vv}^*\} \\ \mathrm{E}\{S_{vv}S_{hh}^*\} & \sqrt{2}\,\mathrm{E}\{S_{vv}S_{hv}^*\} & \mathrm{E}\{S_{vv}S_{vv}^*\} \end{bmatrix} \tag{2.33}$$

where $(\cdot)^\dagger$ and $(\cdot)^*$ denote the transpose conjugate and conjugate, respectively. In the same way, the coherency matrix is defined as $\mathbf{T} = \mathrm{E}\{\mathbf{k}_p \mathbf{k}_p^\dagger\}$, giving

$$\mathbf{T} = \frac{1}{2}\begin{bmatrix} \mathrm{E}\{|S_{hh}+S_{vv}|^2\} & \mathrm{E}\{(S_{hh}+S_{vv})(S_{hh}^*-S_{vv}^*)\} & 2\,\mathrm{E}\{(S_{hh}+S_{vv})S_{hv}^*\} \\ \mathrm{E}\{(S_{hh}^*+S_{vv}^*)(S_{hh}-S_{vv})\} & \mathrm{E}\{|S_{hh}-S_{vv}|^2\} & 2\,\mathrm{E}\{(S_{hh}-S_{vv})S_{hv}^*\} \\ 2\,\mathrm{E}\{(S_{hh}^*+S_{vv}^*)S_{hv}\} & 2\,\mathrm{E}\{(S_{hh}^*-S_{vv}^*)S_{hv}\} & 4\,\mathrm{E}\{|S_{hv}|^2\} \end{bmatrix} \tag{2.34}$$

The two matrices are related by the following unitary transformation

$$\mathbf{T} = \frac{1}{2}\begin{bmatrix} 1 & 0 & 1 \\ 1 & 0 & -1 \\ 0 & \sqrt{2} & 0 \end{bmatrix} \mathbf{C} \begin{bmatrix} 1 & 1 & 0 \\ 0 & 0 & \sqrt{2} \\ 1 & -1 & 0 \end{bmatrix} \tag{2.35}$$

The covariance matrix is preferred in this thesis, but all the results can be easily applied to the coherency matrix by the transformation (2.35). Table 2.2 shows some covariance matrices of simple distributed targets [3].

In practice, the number of scattering vectors used to calculate the expectation is limited. Let L denote the number of pixels to compute the average, the PolSAR data are then represented by the so-called sample covariance matrices

$$\mathbf{C}_L = \frac{1}{L}\sum_{i=1}^{L} \mathbf{k}_i \mathbf{k}_i^\dagger \tag{2.36}$$

where $\mathbf{k}_i$ is the ith scattering vector. The averaging is also called multilook processing which can be employed to reduce the speckle of PolSAR data. The L is known as the number of looks.

Table 2.2: Covariance Matrix of Distributed Canonical Bodies

Mechanism	Diagram	**C**
Volume (Forest etc.)	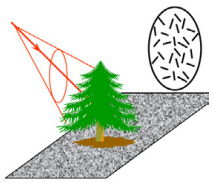	$f_v \begin{bmatrix} 1 & 0 & 1/3 \\ 0 & 2/3 & 0 \\ 1/3 & 0 & 1 \end{bmatrix}$
Reflection Symmetry	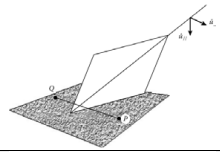	$\begin{bmatrix} C_1 & 0 & C_3 \\ 0 & C_4 & 0 \\ C_3^* & 0 & C_6 \end{bmatrix}$
Rotation Symmetry	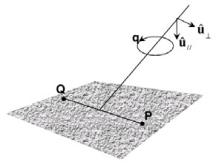	$\begin{bmatrix} C_1 & C_2 & C_3 \\ C_2^* & C_4 & -C_2^* \\ C_3^* & -C_2 & C_1 \end{bmatrix}$
Azimuth Symmetry	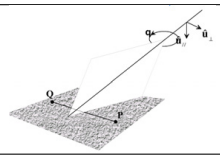	$\begin{bmatrix} C_1 & 0 & C_3 \\ 0 & C_4 & 0 \\ C_3^* & 0 & C_1 \end{bmatrix}$

2.3 PolSAR Systems

PolSAR systems probe their environment with specially designed waveforms, such as different polarization states, to identify targets of interests and extract desired information from them. The two most common polarization states employed are horizontal linear or H, and vertical linear or V. Any arbitrary polarization can be created using these two orthogonal basis [3]. Fig. 2.6 shows a typical implementation of a PolSAR antenna. On transmit, waves of different polarizations are transmitted separately, using a switch to direct energy to the different parts of the antenna in sequence. But the radar antenna is often designed to receive the different polarization components of the EM wave simultaneously [35]. The same antenna are used to transmit and receive EM waves. A polarimetric SAR implemented in this fashion actually acquires four SAR images: one each for the horizontal-horizontal (HH), horizontal-vertical (HV), vertical-horizontal (VH), and vertical-vertical (VV) combinations. The basic measurement for each pixel is, therefore, a complete scattering matrix, or four complex scattering coefficients. Data in this kind of configuration is referred as quad-pol or full-pol data. Other simpler configurations include: 1) single-pol (HH or VV or HV or VH), and 2) dual-pol (HH and HV, VV and VH, or HH and VV).

A general review of the most advanced civilian SAR sensors launched recently that offer fully polarimetric functionality are presented in the following sections. All test SAR data in this thesis are from these sensors.

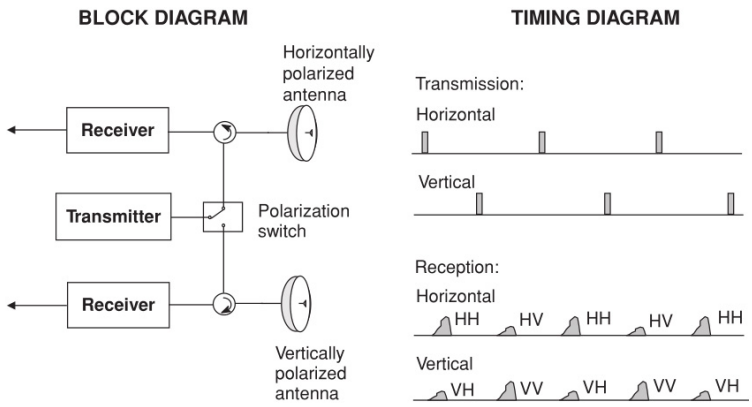

Figure 2.6: Implement of PolSAR sensors (this figure comes from [35]). A polarimetric radar is implemented by alternatively transmitting signals out of horizontally and vertically polarized antennas and receiving at both polarizations simultaneously.

2.3.1 Spaceborne Sensors

Satellite radars have the advantage of being able to collect imagery more quickly over a larger area, and provide consistent viewing geometry. Once a spaceborne imaging sensor becomes operational, the data product should be very consistent and predictable, allowing end users to develop robust applications for exploitation of the imagery.

2.3.1.1 TerraSAR-X

TerraSAR-X is a German Earth-observation satellite that uses an X-band SAR sensor to acquire images of very high spatial resolution. The system was launched on June 15, 2007, with the objective to provide high-resolution SAR data for scientific and commercial applications, such as: hydrology, geology, climatology, oceanography, environmental and disaster monitoring, and cartography (DEM generation, with TanDEM-X) [39, 40].

The satellite is in a near-polar orbit around the Earth, at an altitude of 514 kilometers, with inclination of 97.44 degrees and nominal revisit period of 11 days. TerraSAR-X can cover any point on Earth within a maximum of 4.5 days, 90% of the surface within 2 days [41]. It has three imaging modes, the Stripmap mode, the Spotlight mode and the ScanSAR mode, to meet the different requirements of spatial resolutions by various applications [42]. The X-band SAR sensor offers measurements using different polarizations, single or dual. But unfortunately, the full-polarization imaging is experimental. Full-Pol data is obtained by employing the redundant receiving antenna and splitting the receiving channel into two halves electronically [43]. TerraSAR-X can work both in the right-looking mode with incident angles defined by the full performance range, or in the left-looking mode with a wider range of incidence angles specified by the data access range. System parameters corresponding to the full-polarization imaging are summarized in Table 2.3.

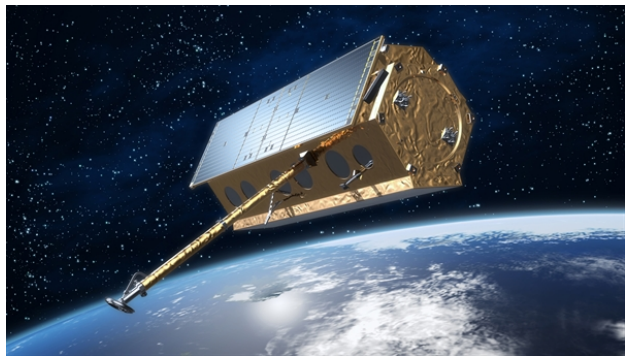

Figure 2.7: TerraSAR-X satellite. Image credit: DLR, available at `http://www.dlr.de/dlr/en/desktopdefault.aspx/tabid-10377/565_read-436/#/gallery/350`

Table 2.3: System Parameters of TerraSAR-X

Parameter	Value
Frequency	X-band (9.65 GHz)
Pulse Repetition Frequency (PRF)	2.0 KHz − 6.5 KHz
Bandwidth	150 MHz (300 MHz experimental)
Obit Altitude	514 km
Repetition Rate	11 days
Spatial Resolution (rg × az)	1.9 m × 6.6 m
Swath Width	15 km
Incidence Angle	20° − 45° (full performance) 15° − 60° (access range)

2.3.1.2 RADARSAT-2

RADARSAT-2 was successfully launched on December 14, 2007. As the Canada's next-generation commercial radar satellite, it offers powerful technical advancements that enhances marine surveillance, ice monitoring, disaster management, environmental monitoring, resource management and mapping [44, 45].

RADARSAT-2 is a follow-on mission of RADARSAT-1. They have the same orbit, 798 km altitude sun-synchronous orbit with 6 p.m. ascending node and 6 a.m. descending node [46]. The satellite has a SAR sensor operating at C-band, which has minimal interference from severe weather conditions and offers consistent and reliable data. It can operate in multiple polarization modes, including two fully polarimetric modes, Standard Quad-Pol and Fine Quad-Pol. The instrument has three fundamental imaging modes: Single Beam (or Stripmap), ScanSAR, and Splotlight. Data of different spatial resolutions are obtained in these modes [46, 47]. The RADARSAT-2 SAR sensor is very flexible. It is possible to reprogram the sensor, adding new modes for example to meet the requirements of resolution and swath width [48]. Table 2.4 shows the satellite characteristics corresponding to the full polarization modes.

Figure 2.8: RADARSAT-2 Satellite. Image credit: CSA, available at `http://www.asc-csa.gc.ca/eng/satellites/radarsat2/default.asp`.

Table 2.4: System Parameters of RADARSAT-2

Parameter	Value
Frequency	C-band (5.405 GHz)
PRF	-
Bandwidth	100 MHz
Obit Altitude	798 km
Repetition Rate	24 days
Spatial Resolution (rg × az)	5.2 m × 7.6 m (Fine Quad-Pol) 9.0 m × 7.6 m (Standard Quad-Pol)
Swath Width	25 km
Incidence Angle	$18° - 49°$

2.3.1.3 ALOS-2

The Advanced Land Observing Satellite-2 (ALOS-2), also called Daichi-2, is a Japanese satellite which was launched on May 24, 2014. As a successor of ALOS, ALOS-2 provides data continuity to be used for cartography, regional observation, disaster monitoring, and environmental monitoring [49, 50].

The satellite, in a sun-synchronous orbit at altitude 628 km, is equipped with a global-leading L-band SAR sensor, PALSAR-2 [51]. Using radio waves of long wavelength makes ALOS-2 especially advantageous to measure forests in tropical areas which are covered by clouds almost all around the year. It is possible to choose one of the three optional frequencies in L-band to avoid the interference into Radio Navigation Satellite Service (RNSS) signal [52]. The sensor also allows Stripmap, ScanSAR and Spotlight observations covering scenes of different sizes, which is the same as TerraSAR-X and RADARSAT-2. Two full-polarization imaging modes, named High-sensitive and Fine, respectively, are available, with system parameters shown in Table 2.5.

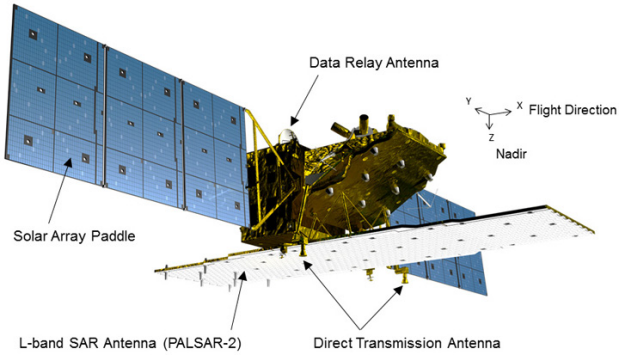

Figure 2.9: ALOS-2 satellite. Image credit: JAXA, available at `http://www.eorc.jaxa.jp/ALOS-2/en/about/overview.htm`.

Table 2.5: System Parameters of ALOS-2

Parameter	Value
Frequency	L-band (1.237, 1.258 or 1.279 GHz)
PRF	1.5 KHz − 3.0 KHz
Bandwidth	42 MHz (High-sensitive), 28 MHz (Fine)
Obit Altitude	798 km
Repetition Rate	14 days
Spatial Resolution (rg × az)	5.1 m × 4.3 m (High-sensitive) 8.7 m × 5.3 m (Fine)
Swath Width	40 km (High-sensitive), 30 km (Fine)
Incidence Angle	8° − 70°

2.3.2 Airborne Sensors

Airborne sensors are flexible to collect data from different flight paths and look directions. An airborne radar is able to make measurements anywhere and at any time as long as weather and flying conditions are acceptable, which make it a tool of great importance in disaster monitoring. In addition, any problems that may occur to the sensor can be inspected conveniently, and upgrades can be easily implemented.

2.3.2.1 F-SAR

F-SAR, as the successor of the E-SAR system developed by DLR, is among the most capable, advanced and flexible radar systems in the world. Its development was triggered by the strong demand of E-SAR users and customers for data being simultaneously acquired at different wavelengths and polarizations [53]. The new system offers very high spatial resolution, excellent radiometric accuracy, and low noise level SAR data in X-, C-, S-, L- and P-band with full polarimetry functionality. And it can obtain remote sensing images up to 4 wavelengths simultaneously (multispectral SAR) [54]. Furthermore, F-SAR supports fully reconfigurable operation. It is very easy to mount other antennas and change

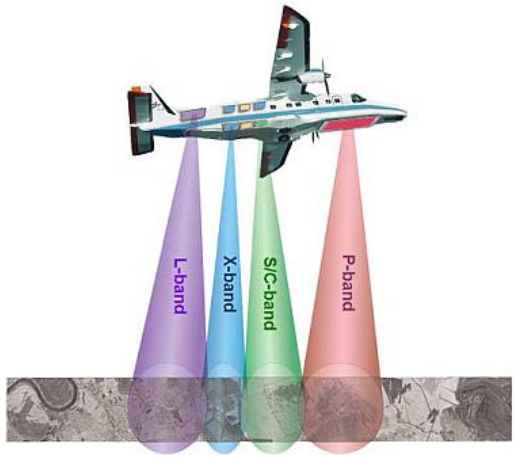

Figure 2.10: Artist's view: F-SAR acquiring data simultaneously in X-, C-, L- and P-bands. Image credit: DLR, available at `http://www.dlr.de/hr/en/desktopdefault.aspx/tabid-2326/3776_read-5691/`.

Table 2.6: System Parameters of F-SAR

	X	C	S	L	P
Frequency (GHz)	9.6	5.3	3.25	1.325	0.35/0.45
Range Resolution (m)	0.2	0.4	0.5	1.0	1.5
Azimuth Resolution (m)	0.2	0.3	0.35	0.4	1.5
Swath Width (km)	$3-5$				
Incidence Angle (deg)	$25^\circ - 60^\circ$				

antenna configuration while avoiding individual airworthiness certification procedures at the same time [53]. Though its first flight took place in November 2006, F-SAR had been under heavy development until 2013, in which year all subsystems were completed and an optimization of their performance was started [55]. A F-SAR X-band image is shown in Fig. 2.16. It can be seen that very high spatial resolution is achieved. Table 2.6 shows some radar parameters of this new system [55].

2.3.2.2 Pi-SAR2 / Pi-SAR-L2

Pi-SAR2 is an airborne X-band polarimetric and cross-track inteferometric SAR designed by National Institute of Information and Communications Technology (NICT), Japan. Its development was started in 2006 with the goal of providing images at finer resolution as well as quick data delivery for disasters, and it had been completed in 2009 [56,57]. The system provides high-resolution polarimetric data with spatial resolution of 0.3 m in the azimuth and the slant range directions. A similar instrument is the Pi-SAR-L2 developed by JAXA in 2011-2012 which operates at L-band. It has a lower spatial resolution but larger swath width [58, 59]. Both Pi-SAR2 and Pi-SAR-L2 are new versions of the Pi-SAR instrument which is a dual-frequency (X-band and L-band) airborne polarimetric

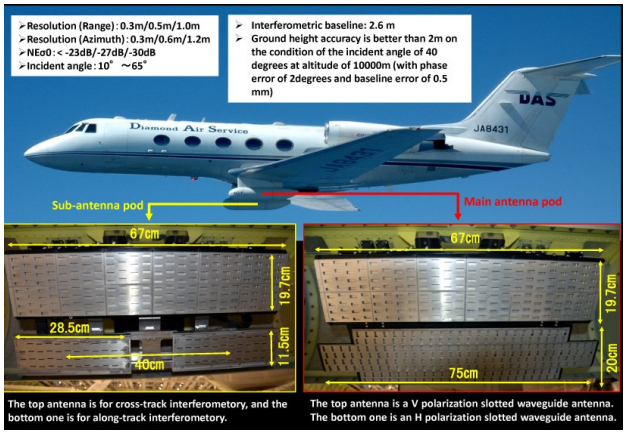

Figure 2.11: Pi-SAR2. Image credit: NICT, available at `https://pi-sar.nict.go.jp/`.

and interferometric SAR. They are mounted on the same Grumman Gulfstream 2 jet plane with a nominal altitude of about 12 km [57, 60]. Detailed radar parameters about these two sensors are shown in Table 2.7 [56, 59].

2.3.2.3 UAVSAR

UAVSAR is a pod-based L-band SAR for interferometric repeat-track observations that is developed at JPL. The radar is designed to be operable on a Unmanned Aerial Vehicle (UAV), but was initially demonstrated on a NASA Gulfstream III aircraft in 2007 [61]. The primary objective of the side-looking UAVSAR instrument is to accurately map crustal deformations associated with natural hazards, such as volcanoes and earthquakes [62]. The radar is fully polarimetric, with a range bandwidth of 80 MHz, 2 m range resolution, and supports a 16 km range swath. The UAVSAR project also serves as a technology test bed. As a modular instrument with numerous plug-and-play components, it is possible to test new technologies for airborne and spaceborne applications. For example, the P-band polarimetry capability was added to UAVSAR to study subcanopy and subsurface soil moisture for a 3-year period in 2011 [63]. Radar characteristics of UAVSAR are shown in Table 2.7 [61].

2.3.2.4 EcoSAR

EcoSAR is a state-of-the-art beamforming SAR recently developed at the NASA's Goddard Space Flight Center (GSFC) for the measurement of ecosystem structure and biomass. The airborne instrument operates at a center frequency of 435 MHz (P-band), and uses a multi-channel reconfigurable architecture to implement fully polarimetric [64]. Utilizing Radio waves with long wavelength makes the instrument very suitable to study canopy layer of forests. The finest resolution of the EcoSAR data is 0.5 m in the azimuth and 0.75 m in the slant range. The instrument architecture allows for the real-time configuration of radar parameters, including center frequency, resolution, incidence angle, and number of beams, among others. Its development was recently completed, and the first flight

Figure 2.12: UAVSAR. Image credit: JPL, available at `http://uavsar.jpl.nasa.gov/education/what-is-uavsar.html`.

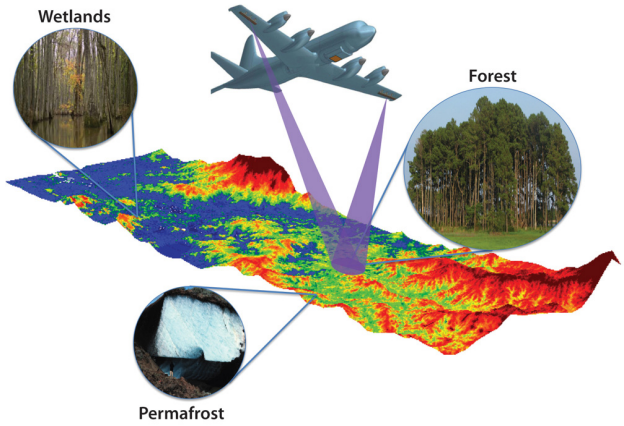

Figure 2.13: EcoSAR. Image credit: NASA, available at `http://neptune.gsfc.nasa.gov/bsb/index.php?section=301`.

campaign was successfully conducted in March 2014 over areas of Bahamas and Costa Rica [65]. Table 2.7 shows more details about this radar system [65].

2.3.3 Ground-Based Sensors

Continuous terrain monitoring of fast changes such as subsidence and landslide is difficult to implement via spaceborne or airborne SAR systems, mainly due to the lack of flexibility and low revisiting frequency. Small and simple ground-based systems that are easy to deploy wherever are needed, must be considered. Ground-based SAR instruments could offer advantages of portability, size, weight, power consumption and cost [66]. In this

Table 2.7: System Parameters of Pi-SAR2, Pi-SAR-L2, UAVSAR and EcoSAR

	Pi-SAR2	Pi-SAR-L2	UAVSAR	EcoSAR
Frequency (GHz)	9.55	1.27	1.26	0.435
Range Resolution (m)	0.3	1.72	1.67	0.75
Azimuth Resolution (m)	0.3	0.8	0.8	0.5
Swath Width (km)	7.2	20	16	4
Incidence Angle (deg)	$10° - 65°$	$7° - 60°$	$25° - 65°$	–

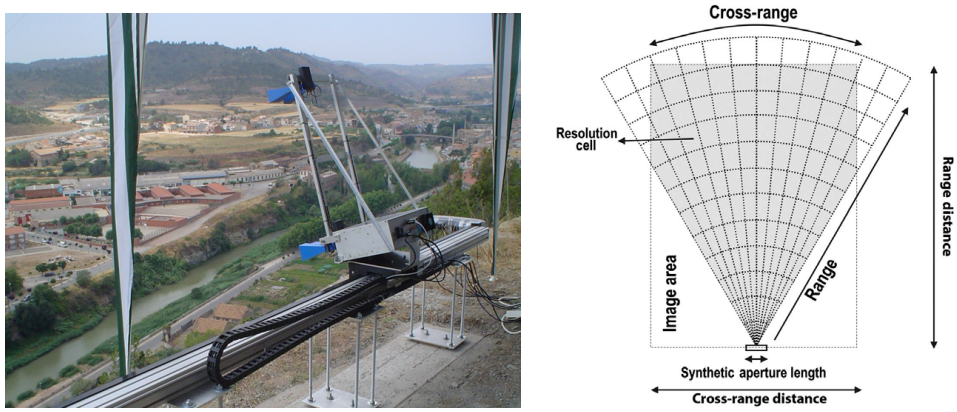

(a) **(b)**

Figure 2.14: RiskSAR instrument. (a) The deployment of RiskSAR. (b) The illustration of resolution cells of a RiskSAR measurement [67].

section, a ground-based SAR developed by Universitat Politècnica de Catalunya (UPC) is explained.

2.3.3.1 RiskSAR

RiskSAR is a polarimetric and interferometric SAR developed by the Remote Sensing Laboratory (RSLab) of UPC. It is flexible and easy to change frequency bands among L, C, X, and Ku-band using interchangeable active frequency multiplication modules. The whole radar, weighting 8.5 kg, is mounted on a linear motion rail to make a synthetic aperture up to 5.5 meters long. And it has a working range from 100 m to 10 km, with a base band signal dynamic range of around 80 dB between targets in near range and far range [66]. As it happens in all ground-based SAR systems available, there is a restriction in the cross-range resolution due to the limited length of the aperture. In fact, the cross-range resolution is not constant along the range direction. Considering the X-band of RiskSAR for example, the center frequency is 9.65 GHz with a bandwidth of 120 MHz. The range resolution reaches 1.25 m while the cross-range resolution differs from 0.75 m at near range up to roughly 5 m at a far range of 1500 m [67]. A plot of a typical measurement setup used in the RiskSAR campaigns is shown in Fig. 2.14.

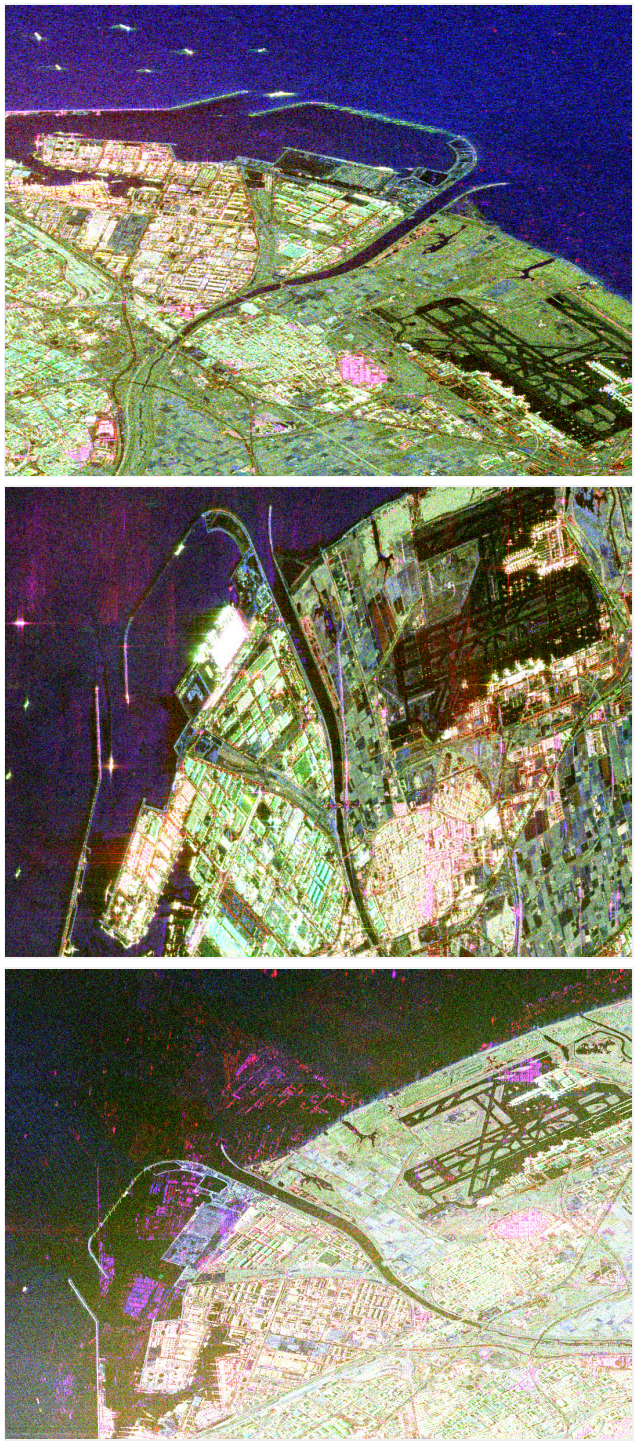

(a) **(b)** **(c)**

Figure 2.15: PolSAR data acquired by different spaceborne sensors over Barcelona, Spain. Color coding: red = $|S_{hh} + S_{vv}|$, green = $|S_{hh} - S_{vv}|$, blue = $|2S_{hv}|$. (a) TerraSAR-X Data. (b) ALOS-2 Data. (c) RADARSAT-2 Data.

(a)

(b)

Figure 2.16: PolSAR data acquired by different airborne sensors. Color coding: red = $|S_{hh} + S_{vv}|$, green = $|S_{hh} - S_{vv}|$, blue = $|2S_{hv}|$. (a) F-SAR X-band Data. (b) UAVSAR Data.

3

Chapter 3

Statistical Models for PolSAR Data

PolSAR systems are mainly employed for observation of natural scenes. Most geophysical media, forests, vegetation and water surface for instance, have a very complicated structure. As a consequence, the scattered wave has a complex behavior. It is unpractical to analyze the scattering process of each target individually due to the lack of knowledge about the detailed structure. Furthermore, the coherent interference between scattered waves makes the PolSAR image have a noise-like appearance which is known as speckle [68]. It is, therefore, more reasonable to analyze the scattering process stochastically, and knowledge of the exact statistical properties of the signal plays an important role in the applications of PolSAR data, such as speckle filtering [69–71], land-use analysis [11, 31], ground cover classification [72–74], etc.

Gaussian statistics for the radar return signals have been frequently assumed, based on the hypothesis that the spatial resolution of PolSAR images is moderate, and the speckle is fully developed [4, 5, 68]. However, the analysis of real PolSAR data reveals that non-Gaussian models give a better representation in certain regions like urban areas, forests, as well as sea surface, implying that processing algorithms based on such models should improve their performance [27, 75]. In the last two decades, a considerable research effort has been dedicated to finding accurate and efficient non-Gaussian models for PolSAR data [6–10].

This chapter provides a review of the statistical models proposed in the literature. First, statistics of the fully developed speckle will be discussed. Properties of the single look scattering vectors and the multilook sample covariance matrices are studied under the Gaussian assumption. Then, the concept of texture will be introduced, along with the

widely studied texture models, including both the scalar texture models and the multi-texture models. At last, finite mixture models, which are widely used to analyze the heterogeneity of data, are detailed.

3.1 Gaussian Statistics

The phenomenon speckle is very common in coherent imaging systems such as laser, SAR, and medical ultrasound. It is primarily due to the interference of the returning waves at the transducer aperture, where the scattered signals add coherently; that is, they add constructively and destructively depending on the relative phases of each scattered waveform [68, 76]. The effect can be clearly noticed in SAR images, as the amplitude or the intensity of the echo signal present a salt-and-pepper aspect (see Fig. 3.2a and Fig. 3.3a for example), which causes difficulties for image interpretation. Nevertheless, useful information can be also extracted from the speckle, particularly when it is linked to the dynamic speckle phenomenon, where the changes of the speckle pattern, in time, can be a measurement of the surface's activity [77]. Therefore, modeling the statistics of the speckle accurately is very important.

Under the assumption that the speckle is fully developed, it has been experimentally verified that the Gaussian statistics generally provide a good fit to SAR data, especially in homogeneous natural areas [4, 78–81]. The multivariate Gaussian distribution, which is both mathematically tractable and efficient, is proper to model the scattering vectors, when the surface roughness is relatively low, the spatial resolution is moderate, and a large number of scatterers are present [3, 68]. The Gaussian assumption indicates that the statistical properties of the data is determined by the covariance matrix. The sample covariance matrix, as a result, follows a complex Wishart distribution, which is widely used in the applications of PolSAR data. There are also some variations of the Wishart distribution that are shown to be more accurate in certain circumstances.

3.1.1 Gaussian Distribution

When a radar illuminates an area of a random surface containing many elementary scatterers, the scattering vector (Section 2.2.2.1), $\mathbf{z}$, can be modeled as having a d-dimensional complex Gaussian distribution with zero mean. The PDF is given by [82]

$$p(\mathbf{z};\boldsymbol{\Sigma}) = \frac{1}{\pi^d|\boldsymbol{\Sigma}|}\exp(-\mathbf{z}^\dagger\boldsymbol{\Sigma}^{-1}\mathbf{z}) \tag{3.1}$$

where $|\cdot|$ is the determinant operation, and $\boldsymbol{\Sigma}$ is the covariance matrix. The complex Gaussian distribution is denoted by $\mathbf{k} \sim \mathcal{CN}(0,\boldsymbol{\Sigma})$ for brevity. The real and imaginary parts of any complex element of $\mathbf{k}$ are assumed to follow a circular Gaussian distribution. For example, consider the ith element $\mathbf{z}_i = x_i + jy_i$, the joint PDF of the real and imaginary parts can be written as

$$p(x_i, y_i; \sigma_i) = \frac{1}{\pi\sigma_i^2}\exp\left(-\frac{x_i^2+y_i^2}{\sigma_i^2}\right) \tag{3.2}$$

where $\sigma_i^2 = \mathbf{\Sigma}_{ii}$. Let r_i be the amplitude and θ_i be the phase of a complex value, then the real part of $\mathbf{z}_i$ can be written as $x_i = r_i \cos\theta_i$, and the imaginary part as $y_i = r_i \sin\theta_i$. The Jacobian determinant of the transform from (x_i, y_i) to (r_i, θ_i) is given by

$$\mathbf{J} = \begin{vmatrix} \cos\theta_i & -r_i \sin\theta_i \\ \sin\theta_i & r_i \cos\theta_i \end{vmatrix} = r_i. \tag{3.3}$$

As a result, the joint PDF of the amplitude and the phase can be obtained from (3.2) after changing variables, giving

$$p(r_i, \theta_i; \sigma_i) = \frac{r_i}{\pi\sigma_i^2} \exp\left(-\frac{r_i^2}{\sigma_i^2}\right). \tag{3.4}$$

The circular Gaussian assumption implies that the phase θ_i is uniformly distributed over $(-\pi, \pi]$, and independent from the amplitude. Averaging over the phase, therefore, gives the PDF of the amplitude

$$p(r_i; \sigma_i) = \frac{2r_i}{\sigma_i^2} \exp\left(-\frac{r_i^2}{\sigma_i^2}\right). \tag{3.5}$$

Equation (3.5) is known as the Rayleigh distribution, with mean value $\sigma_i\sqrt{\pi}/2$. The intensity of the ith channel, $I_i = x_i^2 + y_i^2 = r_i^2$, can be easily proved to have a negative exponential distribution

$$p(I_i; \sigma_i) = \frac{1}{\sigma_i^2} \exp\left(-\frac{I_i}{\sigma_i^2}\right) \tag{3.6}$$

with mean value $\mathrm{E}\{I_i\} = \sigma_i^2$ and variance $\mathrm{Var}\{I_i\} = \sigma_i^4$. This distribution shows that the useful information is described by a single degree of freedom, corresponding to the mean intensity.

Besides the intensity, the joint properties of two different polarimetric channels are of great interest. Considering two polarimetric channels $\mathbf{z}_i = x_i + jy_i$ and $\mathbf{z}_k = x_k + jy_k$, the complex correlation coefficient is determined by

$$\rho e^{j\varphi} = \frac{\mathbf{\Sigma}_{ik}}{\sqrt{\mathbf{\Sigma}_{ii}\mathbf{\Sigma}_{kk}}} \tag{3.7}$$

and the joint PDF of the real parts and imaginary parts of the two channels can be derived from (3.1), which is given as follows [83]

$$\begin{aligned} p(x_i, y_i, x_k, y_k) = & \frac{1}{\pi^2\psi^2(1-\rho^2)} \exp\left(-\frac{\sigma_k^2(x_i^2+y_i^2) + \sigma_i^2(x_k^2+y_k^2)}{\psi^2(1-\rho^2)}\right. \\ & \left. + \frac{2\psi\rho[(x_i x_k + y_i y_k)\cos\varphi + (x_k y_i - x_i y_k)\sin\varphi]}{\psi^2(1-\rho^2)}\right) \end{aligned} \tag{3.8}$$

where $\sigma_i^2 = \mathbf{\Sigma}_{ii}$, $\sigma_k^2 = \mathbf{\Sigma}_{kk}$ and $\psi = \sigma_i\sigma_k$. Write the complex values in the polar form, i.e., $r_i e^{j\theta_i} = x_i + jy_i$ and $r_k e^{j\theta_k} = x_k + jy_k$, by changing variables from (x_i, y_i, x_k, y_k) to $(r_i, \theta_i, r_k, \theta_k)$, the previous distribution becomes

$$p(r_i, \theta_i, r_k, \theta_k) = \frac{r_i r_k}{\pi^2\psi^2(1-\rho^2)} \exp\left(-\frac{\sigma_k^2 r_i^2 + \sigma_i^2 r_k^2 - 2\psi r_i r_k \rho\cos(\theta_i - \theta_k - \varphi)}{\psi^2(1-\rho^2)}\right). \tag{3.9}$$

We are interested in the distributions of the product of the two amplitudes $z = r_i r_k$, and the phase difference $\phi = \theta_i - \theta_k$, since their values reflect the correlation between different polarimetric channels. It can be shown that the Jacobian determinant of the transform from $(r_i, r_k, \theta_i, \theta_k)$ to (r_i, z, θ_i, ϕ) is $-1/r_i$. Thus the following distribution can be obtained after changing variables

$$p(r_i, z, \theta_i, \phi) = \frac{z}{\pi^2 \psi^2 (1-\rho^2)} \frac{1}{r_i} \exp\left(- \frac{\sigma_k^2 r_i^2 + \frac{\sigma_i^2 z^2}{r_i^2} - 2\psi\rho z \cos(\phi - \varphi)}{\psi^2(1-\rho^2)} \right) \tag{3.10}$$

from which the joint PDF of z and ϕ can be further derived by integrating over θ_i and r_i and employing the equality (3.87)

$$p(z, \phi) = \frac{2z}{\pi\psi^2(1-\rho^2)} \exp\left(\frac{2\rho z \cos(\phi - \varphi)}{\psi(1-\rho^2)} \right) K_0\left(\frac{2z}{\psi(1-\rho^2)} \right). \tag{3.11}$$

Here K_v is the modified Bessel function of the second kind of order v [84]. The marginal distribution of the product of the amplitudes, subsequently, is found to be

$$p(z) = \frac{4z}{\psi^2(1-\rho^2)} I_0\left(\frac{2\rho z}{\psi(1-\rho^2)} \right) K_0\left(\frac{2z}{\psi(1-\rho^2)} \right) \tag{3.12}$$

where $I_0(z)$ is the modified Bessel function of the first kind [84] resulting from the integral identity (3.88). Similarly, integrating (3.11) over the amplitudes and following the identity (3.89) gives the marginal distribution of the phase difference

$$p(\phi) = \frac{1-\rho^2}{2\pi(1-\beta^2)} \left\{ \frac{\beta}{\sqrt{\beta^2 - 1}} \ln(-\beta + \sqrt{\beta^2 - 1}) + 1 \right\} \tag{3.13}$$

with $\beta = \rho\cos(\phi - \varphi)$. Note that $-\beta + \sqrt{\beta^2 - 1}$ is a complex number since β is less than 1. Therefore, it can be represented in the polar form, e.g., $-\beta + \sqrt{\beta^2 - 1} = \exp(j(\pi - \arccos\beta))$, and as a result, (3.13) becomes

$$p(\phi) = \frac{1-\rho^2}{2\pi(1-\beta^2)} \left\{ \frac{\beta(\pi - \arccos\beta)}{\sqrt{1-\beta^2}} + 1 \right\}. \tag{3.14}$$

The PDFs shown in (3.12) and (3.14) can be also found in [83, 85].

The Gaussian assumption implies that the statistics of the PolSAR data is completely determined by the covariance matrix. The properties described by the multivariate distribution (3.1) can be analyzed separately by the intensity (3.6), the product of amplitudes (3.12) and the phase difference (3.14). To demonstrate this, two homogeneous Region Of Interest (ROI)s over the crops area of a RADARSAT-2 image are analyzed, as shown in Fig. 3.2. The histograms of the intensity, product of amplitudes and phase difference are plotted, as well as the corresponding PDFs computed using the estimated parameters. It shows that the Gaussian assumption is valid in the test areas.

3.1.2 Wishart Distribution

SAR data are frequently multilook processed for speckle reduction. Under the Gaussian assumption, the sample covariance matrix $\mathbf{C}_L$ defined in Section 2.2.2.2 follows a complex

Wishart distribution, $\mathbf{C}_L \sim \mathcal{CW}(L, \mathbf{\Sigma})$, with PDF given by [82]

$$p(\mathbf{C}_L; L, \mathbf{\Sigma}) = \frac{L^{Ld}|\mathbf{C}_L|^{L-d}\exp(-L\ \mathrm{Tr}(\mathbf{\Sigma}^{-1}\mathbf{C}_L))}{\Gamma_d(L)|\mathbf{\Sigma}|^L} \tag{3.15}$$

where L is the number of looks, and $\mathrm{Tr}(\cdot)$ denotes the matrix trace. The normalization factor $\Gamma_d(L)$ is defined as

$$\Gamma_d(L) = \pi^{d(d-1)/2}\prod_{i=1}^{d}\Gamma(L-i+1) \tag{3.16}$$

with $\Gamma(\cdot)$ referring to the gamma function. The random variables of this distribution are the diagonal terms of $\mathbf{C}_L$ and the real and imaginary parts of the upper (or lower) off-diagonal terms. For d-dimensional radar signal, the total number of independent variables is d^2.

Considering only one polarimetric channel, from (3.15), we have the distribution of the intensity as

$$p(I_i; L, \sigma_i) = \frac{1}{\Gamma(L)}\left(\frac{L}{\sigma_i^2}\right)^L I_i^{L-1}\exp\left(-\frac{L}{\sigma_i^2}I_i\right). \tag{3.17}$$

It is known as the gamma distribution with mean value $\mathrm{E}\{I_i\} = \sigma_i^2$ and variance $\mathrm{Var}\{I_i\} = \sigma_i^4/L$ [86]. The number of looks can be estimated using the mean and the variance of the intensity

$$\hat{L} = \frac{\mathrm{E}^2\{I_i\}}{\mathrm{Var}\{I_i\}}. \tag{3.18}$$

When L is equal to 1, the gamma distribution reduces to the exponential distribution (3.6). The variances of the two different distributions show that the multilook process reduces the speckle by scaling down the fluctuation magnitude with a factor $1/L$.

For two polarimetric channels, saying channel i and channel k, the sample covariance matrix can be written as

$$\mathbf{C}_L = \begin{bmatrix} I_i & R_{ik} + jI_{ik} \\ R_{ik} - jI_{ik} & I_k \end{bmatrix}. \tag{3.19}$$

Let $\rho e^{j\varphi}$ represent the complex correlation coefficient, the joint distribution of I_i, I_k, R_{ik} and I_{ik} can be derived from (3.15), giving

$$\begin{aligned} p(I_i, I_k, R_{ik}, I_{ik}) =& \frac{L^{2L}(I_iI_k - R_{ik}^2 - I_{ik}^2)^{L-2}}{\pi\Gamma(L)\Gamma(L-1)\psi^{2L}(1-\rho^2)^L}\times \\ & \exp\left(-L\frac{\sigma_i^2I_k + \sigma_k^2I_i - 2\rho\psi(R_{ik}\cos\varphi - jI_{ik}\sin\varphi)}{\psi^2(1-\rho^2)}\right) \end{aligned} \tag{3.20}$$

where $\sigma_i^2 = \mathbf{\Sigma}_{ii}$, $\sigma_k^2 = \mathbf{\Sigma}_{kk}$, and $\psi = \sigma_i\sigma_k$. Write the off-diagonal element in the polar form, $ze^{j\phi} = R_{ik} + jI_{ik}$, by changing variables from $(I_i, I_k, R_{ik}, I_{ik})$ to (I_i, I_k, z, ϕ), the following result can be obtained

$$\begin{aligned} p(I_i, I_k, z, \phi) =& \frac{zL^{2L}(I_iI_k - z^2)^{L-2}}{\pi\Gamma(L)\Gamma(L-1)\psi^{2L}(1-\rho^2)^L}\times \\ & \exp\left(-L\frac{\sigma_i^2I_k + \sigma_k^2I_i - 2z\rho\psi\cos(\phi-\varphi)}{\psi^2(1-\rho^2)}\right). \end{aligned} \tag{3.21}$$

The determinant of $\mathbf{C}_L$ must be greater than 0, therefore, we have $I_i I_k - z^2 > 0$. Integrating I_i over $(z^2/I_k, \infty)$ using (3.90) and then I_k over $(0, \infty)$ using (3.87) gives

$$p(z,\phi) = \frac{2L^{L+1}z^L}{\pi\Gamma(L)\psi^{L+1}(1-\rho^2)} \exp\left(\frac{2Lz\rho\cos(\phi-\varphi)}{\psi(1-\rho^2)}\right) K_{L-1}\left(\frac{2Lz}{\psi(1-\rho^2)}\right) \tag{3.22}$$

Subsequently, the marginal distribution of the amplitude can be obtained following the integral identity (3.88)

$$p(z) = \frac{4L^{L+1}z^L}{\Gamma(L)\psi^{L+1}(1-\rho^2)} I_0\left(\frac{2Lz\rho}{\psi(1-\rho^2)}\right) K_{L-1}\left(\frac{2Lz}{\psi(1-\rho^2)}\right) \tag{3.23}$$

and the distribution of the phase difference by identity (3.91)

$$p(\phi) = \frac{(1-\rho^2)^L}{2\sqrt{\pi}(1-\beta)^{2L}} \frac{\Gamma(2L)}{\Gamma(L)\Gamma(L+\frac{3}{2})} {}_2F_1\left(2L, L-\frac{1}{2}, L+\frac{3}{2}, \frac{\beta+1}{\beta-1}\right). \tag{3.24}$$

where $\beta = \rho\cos(\phi-\varphi)$, and ${}_2F_1(a,b;c;z)$ is the Gauss hypergeometric function [84].

Again, the statistical properties of the the multilook data can be analyzed separately using (3.17), (3.23), and (3.24). Fig. 3.3 shows a testing area of an ALOS-2 data over the ocean, where sample covariance matrices are obtained using two different multilook processing window size, 3×3 and 5×5. As it can be seen, the histograms fit the corresponding PDF very well. The variance of the data reduces as increasing the multilook window size, or increasing the number of looks. The Wishart distribution is widely used in the modeling of PolSAR data [4, 70, 87, 88], and there are several variations that make the model more accurate or efficient.

3.1.2.1 Relaxed Wishart Model

Compared with the multivariate complex Gaussian distribution, the Wishart distribution depends on an additional parameter, L, the number of looks. Assume that the multilook processing has different contributions to different types of targets, Anfinsen et al. proposed a refined model called relaxed Wishart distribution [89], in which the number of looks L is treated as a variable shape parameter. In other words, the number of looks is assumed to be distinct in different areas. It is observed that varying L gives a better representation of the data than using a constant L over all regions [89].

3.1.2.2 Wishart-Kotz Distribution

Another variation of the Wishart distribution is the Wishart-Kotz model [90, 91], which exhibits the heavy tails needed to fit the data found in high resolution PolSAR images. In addition, there are no special mathematical functions involved that limit the usefulness by inflicting high computational cost and numerical instability. The sample covariance matrix in the Wishart-Kotz model is assumed to follow a Wishart-Kotz type I distribution with PDF defined as [90]

$$p(\mathbf{C}_L; L, \boldsymbol{\Sigma}, \rho, \beta) = \frac{c|\mathbf{C}_L|^{L-d}}{|\boldsymbol{\Sigma}|^L} (\mathrm{Tr}(\boldsymbol{\Sigma}^{-1}\mathbf{C}_L))^{\beta-1} \exp(-[L\ \mathrm{Tr}(\boldsymbol{\Sigma}^{-1}\mathbf{C}_L)]^\rho) \tag{3.25}$$

with additional parameters ρ and β, and a normalization constant factor c

$$c = \frac{\rho L^{\beta+Ld-1}\Gamma(Ld)}{\Gamma_d(L)\Gamma(\frac{\beta+Ld-1}{\rho})}. \tag{3.26}$$

Here $\Gamma_d(L)$ is the same as that in Wishart model, see (3.16). The Wishart-Kotz distribution is a generalization of the Wishart distribution, which reduces to the latter when $\rho = 1$ and $\beta = 1$.

3.2 Texture Model

As the image resolution increases, the analysis of real PolSAR images reveals that non-Gaussian models give a better representation of the natural areas like forests and rough sea surface [6, 7, 27, 74, 92]. It is widely accepted that the randomness of the radar images is commonly due to two unrelated factors, texture and speckle. The texture models the natural spatial variation of the radar cross section, whereas the speckle, following a complex Gaussian distribution, represents the polarimetric information. The texture and the speckle are incorporated with a product operation which leads to a doubly stochastic model called product model [93]. It has been shown to be successful for modeling and prediction purposes in SAR data [6, 7, 27].

The properties of the speckle are detailed in the previous section. This section illustrates how to model the texture statistically. There are two main manners to manage this: 1) consider the texture as a scalar random variable, or 2) consider it as a vector having the same dimension as the speckle component. They lead to the so called scalar texture model and multi-texture model, respectively. Furthermore, the texture random variable is assumed to be positive with unity mean, therefore, it models the variation of the radar cross section only, leaving the intensities to the speckle component [4, 26]. The statistical properties could be described by a certain distribution, or just a stochastic process without a specific PDF.

3.2.1 Scalar Texture Model

The scalar texture model assumes that the texture component in the product model is a positive scalar random variable. The scattering vector in this case can be written as

$$\mathbf{k} = \sqrt{\tau}\mathbf{z} \tag{3.27}$$

where τ is the texture parameter with mean value equal to 1, and $\mathbf{z}$ is the speckle vector, following a multivariate Gaussian distribution (3.1). The scalar texture model is also referred to as scale mixture of Gaussian [74], or Spherically Invariant Random Vector (SIRV) [13, 94, 95]. For the multilook data, the sample covariance matrix can be expressed as

$$\mathbf{C}_L = \frac{1}{L}\sum_{i=1}^{L}\tau_i\mathbf{z}_i\mathbf{z}_i^\dagger = \frac{\tau}{L}\sum_{i=1}^{L}\mathbf{z}_i\mathbf{z}_i^\dagger \tag{3.28}$$

under the assumption that the texture has a higher spatial correlation than the speckle and the texture parameter is constant over the multilook processing window [7].

For a known τ, (3.27) implies that the scattering vector $\mathbf{k}$ follows a complex Gaussian distribution (Section 3.1.1) with PDF given by

$$p(\mathbf{k}|\tau;\mathbf{\Sigma}) = \frac{1}{\pi^d|\mathbf{\Sigma}|}\frac{1}{\tau^d}\exp\left(-\frac{\mathbf{k}^\dagger\mathbf{\Sigma}^{-1}\mathbf{k}}{\tau}\right) \tag{3.29}$$

where $\mathbf{\Sigma} = E\{\mathbf{k}\mathbf{k}^\dagger\}$ is the covariance matrix. And the distribution of the sample covariance matrix is given by

$$p(\mathbf{C}_L|\tau;L,\mathbf{\Sigma}) = \frac{L^{Ld}|\mathbf{C}_L|^{L-d}}{\Gamma_d(L)|\mathbf{\Sigma}|^L}\frac{1}{\tau^{Ld}}\exp\left(-\frac{L\ \mathrm{Tr}(\mathbf{\Sigma}^{-1}\mathbf{C}_L)}{\tau}\right) \tag{3.30}$$

which is known as the Wishart distribution detailed in Section 3.1.2.

If the PDF of the texture random variable is not explicitly specified, τ can be viewed as an unknown deterministic parameter from pixel to pixel [13]. According to the concept of SIRV, an approximate Maximum Likelyhood (ML) estimator for the texture parameter of each pixel is found to be [13, 94]

$$\begin{aligned}\hat{\tau}_i &= \frac{\mathbf{k}_i^\dagger\hat{\mathbf{\Sigma}}^{-1}\mathbf{k}_i}{d}\\ \hat{\mathbf{\Sigma}} &= \frac{1}{N}\sum_{i=1}^{N}\frac{\mathbf{k}_i\mathbf{k}_i^\dagger}{\hat{\tau}_i}\end{aligned} \tag{3.31}$$

where $\hat{\tau}_i$ is the texture parameter of ith pixel, d is the dimension of the target vector, and N is the number of pixels in the neighborhood. The problem can be solved recursively by [13, 94, 95]

$$\hat{\mathbf{\Sigma}}_{k+1} = \frac{d}{N}\sum_{i=1}^{N}\frac{\mathbf{k}_i\mathbf{k}_i^\dagger}{\mathbf{k}_i^\dagger\hat{\mathbf{\Sigma}}_k^{-1}\mathbf{k}_i} \tag{3.32}$$

where k is the number of iteration. The initialization and the criterion to stop the recursive process are detailed in [13]. This estimator is referred to as fixed point estimator [13].

On the contrary, if the texture random variable is specified by a distribution, averaging all possible τ gives the unconditional or marginal PDF of the scattering vector

$$p(\mathbf{k};\mathbf{\Sigma}) = \int_0^\infty p(\mathbf{k}|\tau;\mathbf{\Sigma})p(\tau)d\tau \tag{3.33}$$

which is analytically solvable for some choices of $p(\tau)$. The PDF of the sample covariance matrix can be obtained similarly by

$$p(\mathbf{C}_L;L,\mathbf{\Sigma}) = \int_0^\infty p(\mathbf{C}_L|\tau;L,\mathbf{\Sigma})p(\tau)d\tau. \tag{3.34}$$

A number of models have been proposed in the literature by introducing different distributions for the texture component, including the $\mathcal{K}$ distribution [7], the $\mathcal{G}^0$ distribution [8,9], the Kummer-$\mathcal{U}$ distribution [10], the $\mathcal{W}$, and the $\mathcal{M}$ distribution [12], to represent different scenes of PolSAR data.

3.2.1.1 $\mathcal{K}$ Distribution

The $\mathcal{K}$ distribution, assuming that the texture is gamma distributed, is widely used to model forests, sea surface, and it can be arguably regarded as one of the most successful radar models [6, 7, 27, 74]. The gamma distribution is given by [86]

$$p(x;\alpha,\theta) = \frac{1}{\Gamma(\alpha)\theta^{\alpha}} x^{\alpha-1} \exp\left(-\frac{x}{\theta}\right) \tag{3.35}$$

with shape parameter α and scale parameter θ. The mean value is $\mu = \alpha\theta$. Let $\tau = \frac{x}{\mu}$ to ensure the mean value of the texture is equal to 1, the texture distribution can be written as

$$p(\tau;\alpha) = \frac{\alpha^{\alpha}}{\Gamma(\alpha)} \tau^{\alpha-1} \exp(-\alpha\tau). \tag{3.36}$$

See Fig. 3.1a for examples of the PDF plots. The PDF of the scattering vector $\mathbf{k}$ can be obtained by substituting the texture distribution into (3.33) and employing the integral equality (3.87)

$$p(\mathbf{k};\alpha,\boldsymbol{\Sigma}) = \frac{1}{\pi^d|\boldsymbol{\Sigma}|} \frac{2\alpha^{\frac{\alpha+d}{2}}}{\Gamma(\alpha)} (\mathbf{k}^{\dagger}\boldsymbol{\Sigma}^{-1}\mathbf{k})^{\frac{\alpha-d}{2}} K_{\alpha-d}\left(2\sqrt{\alpha\mathbf{k}^{\dagger}\boldsymbol{\Sigma}^{-1}\mathbf{k}}\right). \tag{3.37}$$

By the same procedure, inserting (3.36) into (3.34), we have the PDF of the sample covariance matrix as follows

$$\begin{aligned} p(\mathbf{C}_L;\alpha,L,\boldsymbol{\Sigma}) =& \frac{L^{Ld}|\mathbf{C}_L|^{L-d}}{\Gamma_d(L)|\boldsymbol{\Sigma}|^L} \frac{2\alpha^{\frac{\alpha+Ld}{2}}}{\Gamma(\alpha)} \left(L\ \mathrm{Tr}(\boldsymbol{\Sigma}^{-1}\mathbf{C}_L)\right)^{\frac{\alpha-Ld}{2}} \\ & \times K_{\alpha-Ld}\left(2\sqrt{\alpha L\ \mathrm{Tr}(\boldsymbol{\Sigma}^{-1}\mathbf{C}_L)}\right). \end{aligned} \tag{3.38}$$

3.2.1.2 $\mathcal{G}$ and $\mathcal{G}^0$ Distributions

It is shown that the $\mathcal{G}$ distribution and the $\mathcal{G}^0$ distribution have a good representation in extremely heterogeneous regions such as urban areas [9]. Especially, the $\mathcal{G}^0$ distribution has the same number of parameters as the $\mathcal{K}$ distribution, but without complex special functions like the Bessel function which requires intensive computations [8, 9].

The $\mathcal{G}$ distribution assumes that the texture parameter obeys the GIG law which is characterized by the PDF [8, 96]

$$p(x;a,b,p) = \frac{1}{2K_p(\sqrt{ab})} \left(\frac{a}{b}\right)^{\frac{p}{2}} x^{p-1} \exp\left(-\frac{1}{2}\left(\frac{b}{x} + ax\right)\right) \tag{3.39}$$

where $a > 0$, $b > 0$ and p is a real parameter. The mean value of this distribution is $\mu = \sqrt{\frac{b}{a}} \frac{K_{p+1}(\sqrt{ab})}{K_p(\sqrt{ab})}$. Letting $\tau = \frac{x}{\mu}$ gives

$$p(\tau;a,b,p) = \frac{1}{2} \frac{K_{p+1}^p(\sqrt{ab})}{K_p^{p+1}(\sqrt{ab})} \tau^{p-1} \exp\left(-\frac{\sqrt{ab}}{2}\left(\frac{K_p(\sqrt{ab})}{K_{p+1}(\sqrt{ab})}\frac{1}{\tau} + \frac{K_{p+1}(\sqrt{ab})}{K_p(\sqrt{ab})}\tau\right)\right) \tag{3.40}$$

which can be further rewritten as follows by replacing $\sqrt{ab}$ with ω

$$p(\tau;\omega,p)=\frac{1}{2}\frac{K_{p+1}^{p}(\omega)}{K_{p}^{p+1}(\omega)}\tau^{p-1}\exp\left(-\frac{\omega}{2}\left(\frac{K_p(\omega)}{K_{p+1}(\omega)}\frac{1}{\tau}+\frac{K_{p+1}(\omega)}{K_p(\omega)}\tau\right)\right). \tag{3.41}$$

Substituting (3.41) into (3.33) and (3.34), and calculating the integral using (3.87) leads to

$$\begin{aligned}p(\mathbf{k};\omega,p,\mathbf{\Sigma})=&\frac{1}{\pi^d|\mathbf{\Sigma}|}\frac{1}{\eta^p K_p(\omega)}\left(\eta^2+\frac{2\eta}{\omega}\mathbf{k}^\dagger\mathbf{\Sigma}^{-1}\mathbf{k}\right)^{\frac{p-d}{2}}\\&\times K_{p-d}\left(\sqrt{\omega^2+\frac{2\omega}{\eta}\mathbf{k}^\dagger\mathbf{\Sigma}^{-1}\mathbf{k}}\right)\end{aligned} \tag{3.42}$$

and

$$\begin{aligned}p(\mathbf{C}_L;\omega,p,L,\mathbf{\Sigma})=&\frac{L^{Ld}|\mathbf{C}_L|^{L-d}}{\Gamma_d(L)|\mathbf{\Sigma}|^L}\frac{1}{\eta^p K_p(\omega)}\left(\eta^2+\frac{2\eta}{\omega}L\ \mathrm{Tr}(\mathbf{\Sigma}^{-1}\mathbf{C}_L)\right)^{\frac{p-Ld}{2}}\\&\times K_{p-Ld}\left(\sqrt{\omega^2+\frac{2\omega}{\eta}L\ \mathrm{Tr}(\mathbf{\Sigma}^{-1}\mathbf{C}_L)}\right)\end{aligned} \tag{3.43}$$

where $\eta=\frac{K_p(\omega)}{K_{p+1}(\omega)}$. The above expressions are the PDFs of the scattering vector and the sample covariance matrix following $\mathcal{G}$ distributions [8, 97].

The $\mathcal{G}^0$ distribution can be obtained from the $\mathcal{G}$ distribution by letting $a\to 0$. Representing the modified Bessel function $K_v(z)$ using (3.92), (3.39) becomes

$$\begin{aligned}p(x;a,b,p)=&\frac{2^{p-1}\Gamma\left(p+\frac{1}{2}\right)}{b^p\sqrt{\pi}}x^{p-1}\exp\left(-\frac{1}{2}\left(\frac{b}{x}+ax\right)\right)\\&\times\left(\int_1^\infty e^{-\sqrt{ab}t}(t^2-1)^{p-\frac{1}{2}}dt\right)^{-1}.\end{aligned} \tag{3.44}$$

If $a\to 0$, $p=-\lambda$, $b=2\beta$, then the PDF of the GIG distribution is reduced to

$$p(x;\lambda,\beta)=\frac{\beta^\lambda}{\Gamma(\lambda)}x^{-\lambda-1}\exp\left(-\frac{\beta}{x}\right). \tag{3.45}$$

after calculating the integral via (3.93). Equation (3.45) is known as the inverse gamma distribution, or the reciprocal of the gamma distribution (see Fig. 3.1a for examples), with mean value $\mu=\frac{\beta}{\lambda-1}$. Let $\tau=\frac{x}{\mu}$ to ensure the mean value of the texture τ is equal to 1, the PDF becomes

$$p(\tau;\lambda)=\frac{(\lambda-1)^\lambda}{\Gamma(\lambda)}\tau^{-\lambda-1}\exp\left(-\frac{\lambda-1}{\tau}\right). \tag{3.46}$$

The PDFs of the scattering vector and the sample covariance matrix of the $\mathcal{G}^0$ distribution can be obtained by plugging the texture distribution into (3.33) and (3.34), and calculating the integral by (3.95), giving

$$p(\mathbf{k};\lambda,\mathbf{\Sigma})=\frac{1}{\pi^d|\mathbf{\Sigma}|}\frac{\Gamma(\lambda+d)(\lambda-1)^\lambda}{\Gamma(\lambda)}\left(\lambda-1+\mathbf{k}^\dagger\mathbf{\Sigma}^{-1}\mathbf{k}\right)^{-\lambda-d} \tag{3.47}$$

and

$$p(\mathbf{C}_L;\lambda,L,\boldsymbol{\Sigma}) = \frac{L^{Ld}|\mathbf{C}_L|^{L-d}}{\Gamma_d(L)|\boldsymbol{\Sigma}|^L}\frac{\Gamma(\lambda+Ld)(\lambda-1)^\lambda}{\Gamma(\lambda)} \times \left(\lambda-1+L\ \mathrm{Tr}(\boldsymbol{\Sigma}^{-1}\mathbf{C}_L)\right)^{-\lambda-Ld} \tag{3.48}$$

Another extreme case of the GIG distribution is the gamma distribution when $b \to 0$, which leads to the $\mathcal{K}$ distribution [8].

3.2.1.3 Kummer-$\mathcal{U}$ Distribution

Assuming that the texture parameter follows a Fisher distribution, also known as the F-distribution or the Fisher-Snedecor distribution, with PDF given by [86]

$$p(x;d_1,d_2) = \frac{1}{B(\frac{d_1}{2},\frac{d_2}{2})}\left(\frac{d_1}{d_2}\right)^{\frac{d_1}{2}} x^{\frac{d_1}{2}-1}\left(1+\frac{d_1}{d_2}x\right)^{-\frac{d_1+d_2}{2}} \tag{3.49}$$

where $d_1 > 0$ and $d_2 > 0$, the scattering vector or the sample covariance matrix are Kummer-$\mathcal{U}$ distributed, with the ability to model different types of textures, because the Fisher distribution covers a large range of distributions [10, 32]. The mean value of the Fisher distribution is $\mu = \frac{d_2}{d_2-2}$. Let $\tau = \frac{x}{\mu}$, $\xi = d_1/2$, and $\zeta = d_2/2$, we have the distribution for the texture as

$$p(\tau;\xi,\zeta) = \frac{\Gamma(\xi+\zeta)}{\Gamma(\xi)\Gamma(\zeta)}\frac{\xi}{\zeta-1}\left(\frac{\xi}{\zeta-1}\tau\right)^{\xi-1}\left(\frac{\xi}{\zeta-1}\tau+1\right)^{-\xi-\zeta}. \tag{3.50}$$

Inserting the texture distribution into (3.33), the PDF of the scattering vector can be calculated by

$$p(\mathbf{k};\xi,\zeta,\boldsymbol{\Sigma}) = \frac{\Gamma(\xi+\zeta)}{\Gamma(\xi)\Gamma(\zeta)\pi^d|\boldsymbol{\Sigma}|}\left(\frac{\xi}{\zeta-1}\right)^{\xi} \times \int_0^\infty \tau^{\xi-1-d}\left(\frac{\xi}{\zeta-1}\tau+1\right)^{-\xi-\zeta}\exp\left(-\frac{\mathbf{k}^\dagger\boldsymbol{\Sigma}^{-1}\mathbf{k}}{\tau}\right)d\tau \tag{3.51}$$

Replacing τ by $\frac{\zeta-1}{\xi}t^{-1}$, and using (3.96) to calculate the integral results into the distribution of the scattering vector

$$p(\mathbf{k};\xi,\zeta,\boldsymbol{\Sigma}) = \frac{1}{\pi^d|\boldsymbol{\Sigma}|}\frac{\Gamma(\xi+\zeta)\Gamma(\zeta+d)}{\Gamma(\xi)\Gamma(\zeta)}\left(\frac{\xi}{\zeta-1}\right)^{d} \times U\left(d+\zeta,d-\xi+1,\frac{\xi}{\zeta-1}\mathbf{k}^\dagger\boldsymbol{\Sigma}^{-1}\mathbf{k}\right) \tag{3.52}$$

where $U(a,b,z)$ is the hyper-geometric function of the second kind [84]. By the same procedure, the distribution of the sample covariance matrix can be obtained as

$$p(\mathbf{C}_L;\xi,\zeta,L,\boldsymbol{\Sigma}) = \frac{L^{Ld}|\mathbf{C}_L|^{L-d}}{\Gamma_d(L)|\boldsymbol{\Sigma}|^L}\frac{\Gamma(\xi+\zeta)\Gamma(\zeta+Ld)}{\Gamma(\xi)\Gamma(\zeta)}\left(\frac{\xi}{\zeta-1}\right)^{Ld} \times U\left(Ld+\zeta,Ld-\xi+1,\frac{\xi}{\zeta-1}L\ \mathrm{Tr}(\boldsymbol{\Sigma}^{-1}\mathbf{C}_L)\right) \tag{3.53}$$

As a matter of fact, Fisher distributions are the Pearson VI solutions and cover a large range of distributions. It is not only confined to urban scenes, but also fits reasonably in forest and agricultural fields [10,32]. The behavior of the head and tail of the distribution can be controlled by the two parameters ξ and ζ.

3.2.1.4 $\mathcal{W}$ Distribution

The $\mathcal{W}$ distribution assumes the texture to follow a beta distribution [12], which is given by [86]

$$p(x;\alpha,\beta)=\frac{1}{B(\alpha,\beta)}x^{\alpha-1}(1-x)^{\beta-1},\quad x\in[0,1] \tag{3.54}$$

The mean value of the beta distribution is $\mu=\frac{\alpha}{\alpha+\beta}$. Let $\tau=\frac{x}{\mu}$, $\xi=\alpha$, $\zeta=\alpha+\beta$, the distribution of the normalized texture can be written as

$$p(\tau;\xi,\zeta)=\frac{\Gamma(\zeta)}{\Gamma(\xi)\Gamma(\zeta-\xi)}\frac{\xi}{\zeta}\left(\frac{\xi}{\zeta}\tau\right)^{\xi-1}\left(1-\frac{\xi}{\zeta}\tau\right)^{\zeta-\xi-1},\quad \tau\in[0,\frac{\zeta}{\xi}] \tag{3.55}$$

The distribution of the scattering vector in this case can be calculated by

$$\begin{aligned}p(\mathbf{k};\xi,\zeta,\mathbf{\Sigma})=&\frac{\Gamma(\zeta)}{\Gamma(\xi)\Gamma(\zeta-\xi)\pi^d|\mathbf{\Sigma}|}\left(\frac{\xi}{\zeta}\right)^{\zeta-1}\times\\&\int_0^{\frac{\zeta}{\xi}}\tau^{\xi-1-d}\left(\frac{\zeta}{\xi}-\tau\right)^{\zeta-\xi-1}\exp\left(-\frac{\mathbf{k}^\dagger\mathbf{\Sigma}^{-1}\mathbf{k}}{\tau}\right)d\tau\end{aligned} \tag{3.56}$$

which leads to the following result according to the integral identity (3.97)

$$\begin{aligned}p(\mathbf{k};\xi,\zeta,\mathbf{\Sigma})=&\frac{1}{\pi^d|\mathbf{\Sigma}|}\frac{\Gamma(\zeta)}{\Gamma(\xi)}\left(\frac{\xi}{\zeta}\right)^{\frac{\xi+d-1}{2}}\left(\mathbf{k}^\dagger\mathbf{\Sigma}^{-1}\mathbf{k}\right)^{\frac{\xi-d-1}{2}}\times\\&\exp\left(-\frac{\xi}{2\zeta}\mathbf{k}^\dagger\mathbf{\Sigma}^{-1}\mathbf{k}\right)W_{\frac{d+1+\xi-2\zeta}{2},\frac{\xi-d}{2}}\left(\frac{\xi}{\zeta}\mathbf{k}^\dagger\mathbf{\Sigma}^{-1}\mathbf{k}\right)\end{aligned} \tag{3.57}$$

where $W_{a,b}(z)$ is Whittaker W function [84]. The distribution of the sample covariance matrix can be obtained by the same way

$$\begin{aligned}p(\mathbf{C}_L;\xi,\zeta,L,\mathbf{\Sigma})=&\frac{L^{Ld}|\mathbf{C}_L|^{L-d}}{\Gamma_d(L)|\mathbf{\Sigma}|^L}\frac{\Gamma(\zeta)}{\Gamma(\xi)}\left(\frac{\xi}{\zeta}\right)^{\frac{\xi+Ld-1}{2}}\left(L\ \mathrm{Tr}(\mathbf{\Sigma}^{-1}\mathbf{C}_L)\right)^{\frac{\xi-Ld-1}{2}}\times\\&\exp\left(-\frac{\xi}{2\zeta}L\ \mathrm{Tr}(\mathbf{\Sigma}^{-1}\mathbf{C}_L)\right)W_{\frac{Ld+1+\xi-2\zeta}{2},\frac{\xi-Ld}{2}}\left(\frac{\xi}{\zeta}L\ \mathrm{Tr}(\mathbf{\Sigma}^{-1}\mathbf{C}_L)\right)\end{aligned} \tag{3.58}$$

3.2.1.5 $\mathcal{M}$ Distribution

Another possible distribution for the texture is the beta prime distribution, also known as inverted beta distribution, with PDF given by [86]

$$p(x;\alpha,\beta)=\frac{1}{B(\alpha,\beta)}x^{\alpha-1}(1+x)^{-\alpha-\beta},\quad x>0 \tag{3.59}$$

The mean value can be calculated by $\mu = \frac{\alpha}{\beta-1}$. Again, scale the random variable to ensure the mean value is equal to 1 by letting $\tau = \frac{\beta-1}{\alpha+\beta-1}(1+x)$, the above distribution becomes

$$p(\tau;\xi,\zeta) = \frac{\Gamma(\zeta)}{\Gamma(\xi)\Gamma(\zeta-\xi)}\frac{\zeta-1}{\xi-1}\left(\frac{\zeta-1}{\xi-1}\tau\right)^{-\zeta}\left(\frac{\zeta-1}{\xi-1}\tau-1\right)^{\zeta-\xi-1}, \quad \tau > \frac{\xi-1}{\zeta-1} \tag{3.60}$$

where the parameters are changed to $\zeta = \alpha+\beta$, $\xi = \beta$. Equation (3.60) is the texture distribution of the $\mathcal{M}$ distribution [12]. According to the product model, the distribution of the scattering vector can be calculated by

$$\begin{aligned} p(\mathbf{k};\xi,\zeta,\mathbf{\Sigma}) =& \frac{\Gamma(\zeta)}{\Gamma(\xi)\Gamma(\zeta-\xi)\pi^d|\mathbf{\Sigma}|}\left(\frac{\xi-1}{\zeta-1}\right)^{\xi} \times \\ & \int_{\frac{\xi-1}{\zeta-1}}^{\infty} \tau^{-\zeta-d}\left(\tau-\frac{\xi-1}{\zeta-1}\right)^{\zeta-\xi-1}\exp\left(-\frac{\mathbf{k}^\dagger\mathbf{\Sigma}^{-1}\mathbf{k}}{\tau}\right)d\tau \end{aligned} \tag{3.61}$$

Employing the integral identity (3.98), we have the PDF of the scattering vector as

$$p(\mathbf{k};\xi,\zeta,\mathbf{\Sigma}) = \frac{1}{\pi^d|\mathbf{\Sigma}|}\frac{\Gamma(\zeta)\Gamma(\xi+d)}{\Gamma(\xi)\Gamma(\zeta+d)}\left(\frac{\zeta-1}{\xi-1}\right)^{d} M\left(\xi+d,\zeta+d,-\frac{\zeta-1}{\xi-1}\mathbf{k}^\dagger\mathbf{\Sigma}^{-1}\mathbf{k}\right) \tag{3.62}$$

and the PDF of the sample covariance matrix as

$$\begin{aligned} p(\mathbf{C}_L;\xi,\zeta,L,\mathbf{\Sigma}) =& \frac{L^{Ld}|\mathbf{C}_L|^{L-d}}{\Gamma_d(L)|\mathbf{\Sigma}|^L}\frac{\Gamma(\zeta)\Gamma(\xi+Ld)}{\Gamma(\xi)\Gamma(\zeta+Ld)}\left(\frac{\zeta-1}{\xi-1}\right)^{Ld} \\ & \times M\left(\xi+Ld,\zeta+Ld,-\frac{\zeta-1}{\xi-1}L\ \mathrm{Tr}(\mathbf{\Sigma}^{-1}\mathbf{C}_L)\right) \end{aligned} \tag{3.63}$$

Here $M(a,b,z)$ is the confluent hypergeometric function of the first kind, also known as the KummerM function [84]. The $\mathcal{W}$ distribution and the $\mathcal{M}$ distribution are able to model data with low variance but extreme skewness, which is particularly relevant to data with textural variability after a speckle filtering [12].

3.2.1.6 Wishart-Generalized Gamma Distribution

The Wishart-Generalized Gamma (WGΓ) distribution employs the generalized gamma distribution to model the texture. The generalized gamma distribution has a more compact form and a larger variety of alternative distributions, with the gamma, the Weibull, the Rayleigh, and the exponential distributions being its special cases, and is of greater flexibility in the statistical modeling compared with the gamma and the Fisher distributions [98]. The PDF of the generalized gamma distribution is given by [86]

$$p(x;v,\theta,k) = \frac{v}{\theta\Gamma(k)}\left(\frac{x}{\theta}\right)^{kv-1}\exp\left(-\left(\frac{x}{\theta}\right)^{v}\right), \quad v>0,\theta>0,k>0 \tag{3.64}$$

which reduces to the gamma distribution (3.35) when $v=1$. The mean value is given by $\mu = \theta\Gamma(k+\frac{1}{v})/\Gamma(k)$. Scaling the mean value to 1, the PDF for the texture is obtained

$$p(\tau;v,k) = \frac{v\beta^{kv}}{\Gamma(k)}\tau^{kv-1}e^{-(\beta\tau)^v} \tag{3.65}$$

where $\beta = \Gamma(k + \frac{1}{v})/\Gamma(k)$. Examples of the PDFs can be found in Fig. 3.1b. The distribution of the scattering vector $\mathbf{k}$ then can be calculated by

$$p(\mathbf{k}; v, k, \boldsymbol{\Sigma}) = \frac{v\beta^{kv}}{\Gamma(k)\pi^d|\boldsymbol{\Sigma}|} \int_0^\infty \tau^{kv-d-1} \exp\left(-(\beta\tau)^v - \frac{\mathbf{k}^\dagger\boldsymbol{\Sigma}^{-1}\mathbf{k}}{\tau}\right) d\tau. \tag{3.66}$$

There is no closed form expression for the above equation, but it can be solved numerically [98]. The distribution of the sample covariance matrix can be calculated by

$$\begin{aligned} p(\mathbf{C}_L; v, k, L, \boldsymbol{\Sigma}) =& \frac{v\beta^{kv} L^{LD} |\mathbf{C}_L|^{L-d}}{\Gamma(k) I(L,d) |\boldsymbol{\Sigma}|^L} \\ & \times \int_0^\infty \tau^{kv-Ld-1} \exp\left(-(\beta\tau)^v - \frac{L \operatorname{Tr}(\boldsymbol{\Sigma}^{-1}\mathbf{C}_L)}{\tau}\right) d\tau. \end{aligned} \tag{3.67}$$

It is reported that the WGΓ distribution could provide better fitness than the $\mathcal{K}$ and Kummer-$\mathcal{U}$ distributions for different land cover types of homogeneous, heterogeneous, and extremely heterogeneous terrains [98].

3.2.1.7 Generalized $\mathcal{K}$ Distribution

The well-known gamma distribution sometimes cannot fit the texture distribution accurately in very heterogeneous areas. In order to improve the flexibility of the model, it is assumed that the texture follows a Laguerre expansion of the gamma distribution [99], with its PDF given by

$$p(\tau; \alpha, \mu) = \frac{\tau^{\alpha-1}}{\Gamma(\alpha)} \left(\frac{\alpha}{\mu}\right) \exp\left(-\frac{\alpha\tau}{\mu}\right) \sum_{u=0}^{\infty} \xi_u \frac{\Gamma(\alpha) u!}{\Gamma(u+\alpha)} L_u^{\alpha-1}\left(\frac{\alpha\tau}{\mu}\right) \tag{3.68}$$

where μ, the mean value, is normally assumed to be equal to 1, and

$$\xi_u = \sum_{k=0}^{u} (-1)^k \binom{u+\alpha-1}{u-k} \frac{1}{k!} \left(\frac{\alpha}{\mu}\right)^k E\{x^k\}. \tag{3.69}$$

The Laguerre polynomial $L_u^{\alpha-1}(x)$ is given by

$$L_u^{\alpha-1}(x) = \sum_{k=0}^{u} (-1)^k \binom{u+\alpha-1}{u-k} \frac{x^k}{k!}. \tag{3.70}$$

The PDF of the sample covariance matrix in this case can be expressed as

$$\begin{aligned} p(\mathbf{C}_L; \alpha, \mu, L, \boldsymbol{\Sigma}) =& \frac{L^{Ld}|\mathbf{C}_L|^{L-d}}{\Gamma_d(L)|\boldsymbol{\Sigma}|^L} \frac{\alpha^\alpha}{\Gamma(\alpha)\mu^\alpha} \times \sum_{u=0}^{\infty} \xi_u \frac{\Gamma(\alpha)u!}{\Gamma(u+\alpha)} \sum_{k=0}^{u} (-1)^k \\ & \frac{2}{k!} \frac{(u+\alpha-1)!}{(u-k)!(\alpha-1+k)!} \left(\frac{\alpha}{\mu}\right)^k \left(\frac{L\mu \operatorname{Tr}(\boldsymbol{\Sigma}^{-1}\mathbf{C}_L)}{\alpha}\right)^{\frac{\alpha+k-Ld}{2}} \\ & K_{\alpha+k-Ld}\left(2\sqrt{\frac{\alpha}{\mu} L \operatorname{Tr}(\boldsymbol{\Sigma}^{-1}\mathbf{C}_L)}\right) \end{aligned} \tag{3.71}$$

which is a weighted combination of a series of $\mathcal{K}$ distributions based on a Laguerre polynomial expansion. It shows that the generalized $\mathcal{K}$ distribution gives a better approximation than the $\mathcal{K}$ distribution when there exist strong scatterers in the scene [99].

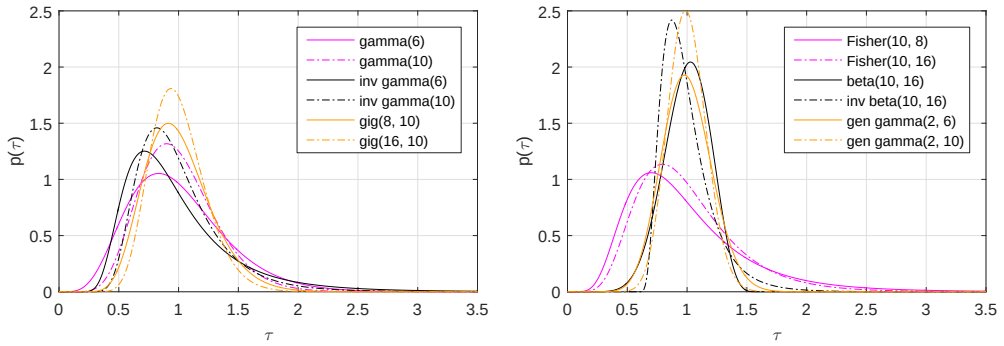

(a) **(b)**

Figure 3.1: PDFs of different texture distributions. (a) PDFs of gamma, inverse gamma and GIG distributions. (c) PDFs of Fisher, beta, inverted beta, and generalized gamma distributions.

3.2.2 Multi-texture Model

In the scalar texture model, different polarimetric channels are assumed to have a common texture variable. However, if the electromagnetic wave sees different geometrical or dielectric properties of the target, and if those properties are spatially modulated, then the texture of each channel should be different [14]. For example, in scattering from forest areas, volume scattering will affect the cross-pol component stronger than the copol channels, whereas surface scattering will have the opposite effect [19]. The scalar texture model must, therefore, be extended to take into consideration the different radar cross section modulations in polarimetric channels. One solution is to allow for a vector component of the radar cross section in the product model. This kind of models are called multi-texture model.

Under the assumption of reciprocity, there are only three independent complex coefficients required to characterize the scatter under observation. The multi-texture model then can be formulated as [17, 19, 20, 100]

$$\mathbf{k} = \mathbf{\Lambda}^{1/2}\mathbf{z} \tag{3.72}$$

where $\mathbf{z}$ represents the speckle, following a multivariate Gaussian distribution (see Section 3.1.1), and $\mathbf{\Lambda}$ is a diagonal matrix containing texture variables for each channel

$$\mathbf{\Lambda} = \begin{bmatrix} \tau_{hh} & 0 & 0 \\ 0 & \tau_{hv} & 0 \\ 0 & 0 & \tau_{vv} \end{bmatrix}. \tag{3.73}$$

The texture parameters are assumed to be positive, and we have $\mathrm{E}\{\mathbf{\Lambda}\}$ equal to $\mathbf{I}$, the identity matrix. Assuming that the texture variables are constant on the scale of the multilook processing window, the sample covariance matrix can be written as

$$\mathbf{C}_L = \frac{1}{L}\sum_{i=1}^{L}\mathbf{k}_i\mathbf{k}_i^T = \mathbf{\Lambda}^{1/2}\mathbf{W}\mathbf{\Lambda}^{1/2} \tag{3.74}$$

where $\mathbf{W}$ is Wishart distributed, see Section 3.1.2.

Provided that the distributions of the texture variables are known, the PDF of the scattering vector can be calculated using

$$p(\mathbf{k};\mathbf{\Sigma}) = \int_{\Omega^+} p(\mathbf{k}|\mathbf{\Lambda};\mathbf{\Sigma})p(\mathbf{\Lambda})d\mathbf{\Lambda} \tag{3.75}$$

where Ω^+ is the set of all diagonal matrices with non-negative entries. After changing variable by $\mathbf{z} = \mathbf{\Lambda}^{-1/2}\mathbf{k}$, the conditional distribution of $\mathbf{k}$ on $\mathbf{\Lambda}$ can be obtained from (3.1), giving

$$p(\mathbf{k}|\mathbf{\Lambda};\mathbf{\Sigma}) = \frac{1}{\pi^d|\mathbf{\Sigma}||\mathbf{\Lambda}|}\exp\left(-\mathbf{k}^\dagger\mathbf{\Lambda}^{-1/2}\mathbf{\Sigma}^{-1}\mathbf{\Lambda}^{-1/2}\mathbf{k}\right). \tag{3.76}$$

By the similar way, we have the distribution of the sample covariance matrix as [19, 100]

$$p(\mathbf{C}_L;L,\mathbf{\Sigma}) = \int_{\Omega^+} p(\mathbf{C}_L|\mathbf{\Lambda};L,\mathbf{\Sigma})p(\mathbf{\Lambda})d\mathbf{\Lambda} \tag{3.77}$$

where

$$p(\mathbf{C}_L|\mathbf{\Lambda};L,\mathbf{\Sigma}) = \frac{L^{Ld}|\mathbf{C}_L|^{L-d}}{\Gamma_d(L)|\mathbf{\Sigma}|^L|\mathbf{\Lambda}|^L}\exp\left(-L\ \mathrm{Tr}(\mathbf{\Sigma}^{-1}\mathbf{\Lambda}^{-1/2}\mathbf{C}_L\mathbf{\Lambda}^{-1/2})\right). \tag{3.78}$$

Different texture variables for the multi-texture model can be: 1) totally dependent, in which case it reduces to the scalar texture model, 2) independent from each other, that is, texture variables follow different distributions with different parameters, or 3) partially correlated [15, 17]. In many cases, it is reasonable to assume copol channels have the same texture but different from that of the cross-pol channels, which is usually referred to as dual-texture model [18, 19, 100]. For reciprocal media with reflection symmetry for example, the PDF of the sample covariance matrix can be expanded as [100]

$$\begin{aligned} p(\mathbf{C}_L;L,\mathbf{\Sigma}) =& \frac{L^{3L}|\mathbf{C}_L|^{L-3}}{I(L,3)|\mathbf{\Sigma}|^L}\int_0^\infty \exp\left(-L\frac{q_{22}c_{22}}{T_x}\right)\frac{p(T_x)}{T_x^L}dT_x\times \\ & \int_0^\infty \exp\left(-L\frac{q_{11}c_{11}+q_{13}c_{31}+q_{31}c_{13}+q_{33}c_{33}}{T_{co}}\right)\frac{p(T_{co})}{T_{co}^{2L}}dT_{co} \end{aligned} \tag{3.79}$$

where q_{ij} and c_{ij} denote the (i,j)th entry of matrix $\mathbf{C}_L$ and $\mathbf{\Sigma}$ respectively. The texture of the copol channels is represented by T_{co} and that of the cross-pol channel by T_x.

3.2.2.1 Correlated $\mathcal{K}$ Distribution

The correlated $\mathcal{K}$ distribution assumes that the texture variables of different polarimetric channels are partially correlated, each following a gamma distribution [15, 17]. Unfortunately, there is no explicit expression for the joint distribution of the texture variables, or the correlated gamma distribution. The texture of polarimetric channel i, specified by the PDF (3.36) with parameter α, is given by [15]

$$\tau_i = \frac{1}{2\alpha}\sum_{k=1}^{2\alpha}[g_i^{(k)}]^2 \tag{3.80}$$

where $g_i^{(k)}$ is the ith element of the vector $\mathbf{g}^{(k)}, k = 1, \cdots, 2\alpha$, which is Gaussian distributed with zero mean, variance one, and correlation matrix $\mathbf{T}$. The correlation properties of the texture variables is also specified by $\mathbf{T}$. The characteristic function of the vector containing all texture variables is [15]

$$C(\boldsymbol{\omega}) = \frac{1}{|\mathbf{I} + j(1/\alpha)\mathbf{T}\mathbf{W}|^{\alpha}} \tag{3.81}$$

where $\mathbf{W}$ is a diagonal matrix having the entry (i, i) equal to the ith element of the characteristic function variable $\boldsymbol{\omega}$. This model requires that all polarimetric channels have the same half-integer distribution parameter α, e.g., 0.5, 1.5, 2.5 and so on.

3.2.2.2 Dual-Texutre $\mathcal{G}$ Distribution

The dual-texture $\mathcal{G}$ distribution is derived by considering different texture variables for copol and cross-pol channels. The copol and cross-pol texture variables are modelled by the GIG distribution (3.39) separately, which yields a more flexible multivariate distribution [18]. Under the assumption of reciprocity and reflection symmetry, the statistical properties of the single look complex data is characterized by the distribution [18]

$$p(\mathbf{k}; \boldsymbol{\Sigma}, \boldsymbol{\theta}) = \frac{1}{\pi^d |\boldsymbol{\Sigma}|} \prod_{i=1}^{2} \frac{(\eta_i^2 + 2\eta_i s_i/\omega_i)^{\frac{p_i - d + i}{2}}}{\eta_i^{p_i} K_{p_i}(\omega_i)} K_{p_i - d + i}\left(\sqrt{\omega_i^2 + 2\omega_i s_i/\eta_i}\right) \tag{3.82}$$

where $\boldsymbol{\theta} = \{\omega, p_i, \eta_i\}$ consists of all parameters for the GIG texture distributions (see Section 3.2.1.2), $s_1 = z_{11}c_{11} + z_{13}c_{31} + z_{31}c_{13} + z_{33}c_{33}$, and $s_2 = z_{22}c_{22}$, with z_{ij} and c_{ij} indexing entries of $\mathbf{Z} = \mathbf{k}\mathbf{k}^{\dagger}$ and $\boldsymbol{\Sigma}$ respectively.

3.3 Finite Mixture Model

The heterogeneity that appears in PolSAR data may result from the mixture of different targets. For instance, from an urban area which usually consists of different objects like houses, trees and roads, the backscattering is a combination of different scattering mechanisms. The forest areas sometimes can be treated as a mixture of bright clutters and dark ones, corresponding to the strong returns from the crowns of trees and the shadows behind them. To represent this type of data, a simple model would be inappropriate. Finite mixture models, instead, could achieve reasonable level of accuracy [22–24].

Assume that the region under analysis can be modeled by a mixture of K components, then the overall PDF of the data can be written as a weighted sum of the probabilities of each component [101]

$$p(\mathbf{x}; \boldsymbol{\theta}) = \sum_{k=1}^{K} w_k p_k(\mathbf{x}; \boldsymbol{\theta}_k) \tag{3.83}$$

where $\boldsymbol{\theta}$ is a vector collecting all the parameters of the distribution and the mixing proportions obey

$$\sum_{k=1}^{K} w_k = 1, \; w_k \geq 0. \tag{3.84}$$

It has been shown that for complicated regions with more irregular histograms (multimodal, spiky), the finite mixture model is more accurate than a single distribution [22–24].

There are many options for the distributions of the mixing components, but here we mainly focus on the mixture of Wishart distributed components. For different mixing components, the number of looks are the same. The PDF, therefore, can be written as

$$p(\mathbf{C}_L; L, \boldsymbol{\theta}) = \frac{L^{Ld}|\mathbf{C}_L|^{L-d}}{\Gamma_d(L)} \sum_{k=0}^{K} \frac{w_k \exp(-L\ \mathrm{Tr}(\boldsymbol{\Sigma}_k^{-1}\mathbf{C}_L))}{|\boldsymbol{\Sigma}_k|^L} \tag{3.85}$$

where $\boldsymbol{\theta} = \{\boldsymbol{\Sigma}_k, k = 1, \cdots, K\}$ and $\Gamma_d(L)$ is given by (3.16). The PDF of the ith channel intensity, which is also a finite mixture, is found to be

$$p(I_i; L, \boldsymbol{\theta}) = \frac{I_i^{L-1}}{\Gamma(L)} \sum_{k=0}^{K} \left(\frac{L}{\sigma_{k,i}^2}\right)^L \exp\left(-\frac{L}{\sigma_{k,i}^2} I_i\right) \tag{3.86}$$

where $\sigma_{k,i}^2 = [\boldsymbol{\Sigma}_k]_{ii}$. The most interesting property of a mixture density is that the shape of the density is extremely flexible. A mixture density may be multimodal, or even if it is unimodal, may exhibit considerable skewness or additional humps. For this reason, finite mixture distributions offer a flexible way to describe rather heterogeneous data by summarizing the characteristics of the data in terms of the number and the spread of the mixture components [101].

Integral Identities

Some integral identities used in this chapter are listed out here.

1. [102, p.368, Eq 3.471-9]

$$\int_0^\infty x^{v-1} \exp\left(-\frac{\beta}{x} - \alpha x\right) dx = 2\left(\frac{\beta}{\alpha}\right)^{v/2} K_v\left(2\sqrt{\beta\alpha}\right) \qquad \mathrm{Re}\,\beta > 0, \mathrm{Re}\,\alpha > 0 \tag{3.87}$$

   K_v is the modified Bessel function of the second kind of order v.

2. [102, p.340, Eq 3.339]

$$\int_0^\pi \exp(z\cos x) dx = \pi I_0(z) \tag{3.88}$$

   $I_0(z)$ is the modified Bessel function of the first kind.

3. [102, p.702, Eq 6.624-1]

$$\begin{aligned}\int_0^\infty x e^{-\alpha x} K_0(\beta x) dx =& \frac{1}{\alpha^2 - \beta^2} \\ &\times \left\{ \frac{\alpha}{\sqrt{\alpha^2 - \beta^2}} \ln\left(\frac{\alpha}{\beta} + \sqrt{\left(\frac{\alpha}{\beta}\right)^2 - 1}\right) - 1 \right\}\end{aligned} \tag{3.89}$$

4. [102, p.347, Eq 3.382-2]

$$\int_u^\infty (x-u)^v e^{-\mu x} dx = \mu^{-v-1} e^{-u\mu} \Gamma(v+1), \quad u > 1, \operatorname{Re} v > -1, \operatorname{Re} \mu > 0 \tag{3.90}$$

5. [102, p.700, Eq 6.621-3]

$$\begin{aligned} \int_0^\infty x^{\mu-1} e^{-\alpha x} K_v(\beta x) dx =& \frac{\sqrt{\pi}(2\beta)^v}{(\alpha+\beta)^{\mu+v}} \frac{\Gamma(\mu+v)\Gamma(\mu-v)}{\Gamma(\mu+1/2)} \\ & \times {}_2F_1\left(\mu+v, v+\frac{1}{2}; \mu+\frac{1}{2}; \frac{\alpha-\beta}{\alpha+\beta}\right) \\ & \operatorname{Re}\mu > |\operatorname{Re} v|, \operatorname{Re}(\alpha+\beta) > 0 \end{aligned} \tag{3.91}$$

${}_2F_1(a, b; c; z)$ is the Gauss hypergeometric function.

6. [102, p.917, Eq 8.432-3]

$$K_v(z) = \frac{\left(\frac{z}{2}\right)^v \Gamma\left(\frac{1}{2}\right)}{\Gamma\left(v+\frac{1}{2}\right)} \int_1^\infty e^{-zt} (t^2-1)^{v-\frac{1}{2}} dt, \quad \operatorname{Re}\left(v+\frac{1}{2}\right) > 0, |\arg z| < \frac{\pi}{2} \tag{3.92}$$

7. [102, p.325, Eq 3.252-3]

$$\begin{aligned} \int_1^\infty x^{\mu-1}(x^p-1)^{v-1} =& \frac{1}{p} B\left(1-v-\frac{\mu}{p}, v\right) \\ & p > 0, \operatorname{Re} v > 0, \operatorname{Re}\mu < p(1-\operatorname{Re} v) \end{aligned} \tag{3.93}$$

8. The gamma function is defined as

$$\Gamma(t) = \int_0^\infty x^{t-1} e^{-x} dx. \tag{3.94}$$

Let $x = \frac{\beta}{y}$ where $\beta > 0$, we have the following equation after changing variables

$$\int_0^\infty y^{-t-1} \exp\left(-\frac{\beta}{y}\right) dy = \Gamma(t)\beta^{-t} \tag{3.95}$$

9. [84, p505, Eq 13.2.5]

$$\int_0^\infty e^{-zt} t^{a-1} (1+t)^{b-a-1} dt = \Gamma(a) U(a, b, z) \tag{3.96}$$

U is the confluent hypergeometric function of the second kind, or KummerU function.

10. [102, p367, Eq 3.471-2]

$$\begin{aligned} \int_0^u x^{v-1}(u-x)^{\mu-1} \exp\left(-\frac{\beta}{x}\right) dx =& \beta^{\frac{v-1}{2}} u^{\frac{2\mu+v-1}{2}} \Gamma(\mu) \\ & \times \exp\left(-\frac{\beta}{2u}\right) W_{\frac{1-2\mu-v}{2}, \frac{v}{2}}\left(\frac{\beta}{u}\right) \\ & \operatorname{Re}\mu > 0, \operatorname{Re}\beta > 0, \mu > 0 \end{aligned} \tag{3.97}$$

W is Whittaker W function.

11. [102, p368, Eq 3.471-5]

$$\begin{aligned}\int_u^\infty x^{v-1}(x-u)^{\mu-1}\exp\left(\frac{\beta}{x}\right)dx =& B(1-\mu-v,\mu)u^{\mu+v-1} \\ &\times M\left(1-\mu-v,1-v,\frac{\beta}{u}\right) \\ &0<\operatorname{Re}\mu<\operatorname{Re}(1-v), u>0\end{aligned} \tag{3.98}$$

M is the confluent hypergeometric function of the first kind, also known as the KummerM function.

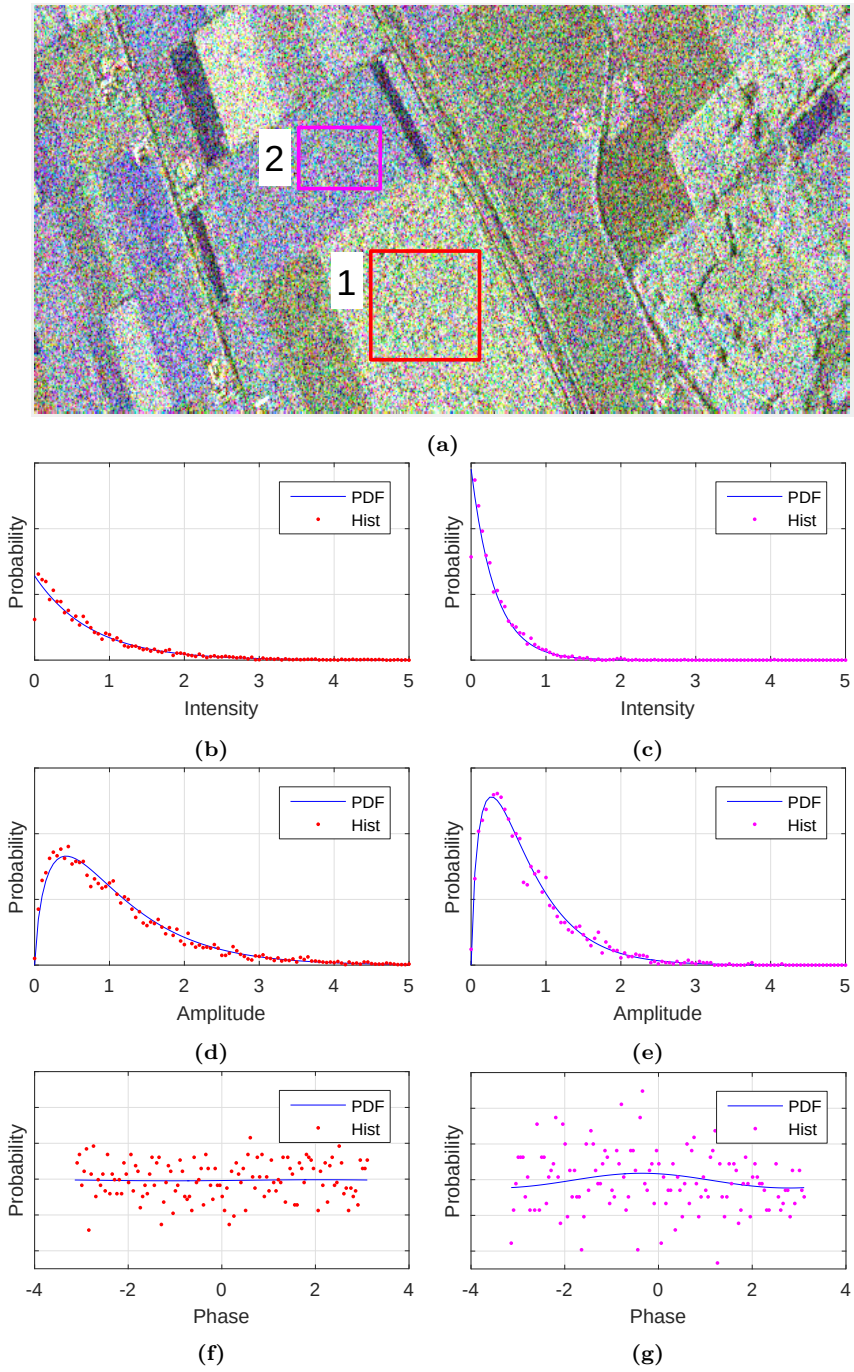

Figure 3.2: Histograms of two homogeneous areas of a RADARSAT-2 image and PDFs under Gaussian assumption. (a) Pauli decomposition (Section 2.2.2) of the RADARSAT-2 data and two ROIs. (b) and (c), Histograms and PDFs of the S_{hh} intensity. (d) and (e), Histograms and PDFs of the amplitude product of S_{hh} channel and S_{hv} channel. (f) and (g), Histograms and PDFs of phase difference between S_{hh} channel and S_{hv} channel.

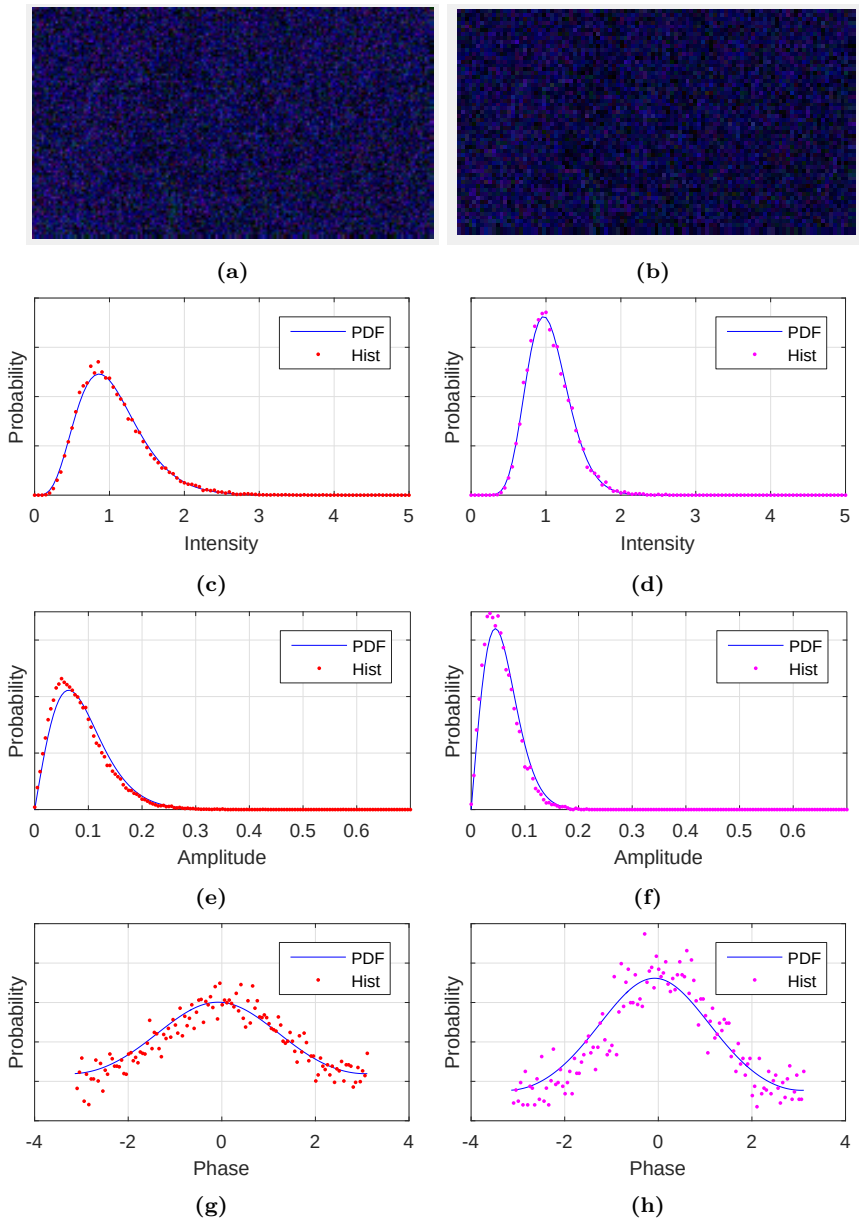

Figure 3.3: Histograms of a homogeneous area in a ALOS-2 image and PDFs under Gaussian assumption. The first column shows the results using a 3×3 filtering and the second column the results using a 5×5 filtering. (a) and (b), Pauli decomposition. (c) and (d), Histograms and PDFs of the S_{hh} intensity. (e) and (f), Histograms and PDFs of the amplitude product of S_{hh} channel and S_{hv} channel. (g) and (h), Histograms and PDFs of the phase difference between the S_{hh} channel and S_{hv} channel.

4

Chapter 4
Statistics for Texture Analysis

As shown in the previous chapter, there are many models proposed to represent the statistical behavior of PolSAR data. How to determine the actual distribution of the data correctly is a critical challenge. Some comparative statistics, as well as tools to visualize the fit of the models to data, are required. There are three widely employed approaches.

The most intuitive way is to calculate the histogram, or empirical PDF of the data, and then compare it with the theoretical distribution channel by channel [4, 8]. To quantify the difference, measures such as Kolmogorov-Smirnov (KS) distance and correlation coefficient can be employed [10, 22], where the KS distance is an estimate of the discrepancy between the empirical distribution function of the samples and the cumulative distribution function of the reference distribution, and the correlation coefficient provides a simple quantitative measure of the similarity between two distributions. Methods based on the empirical PDF, however, depend on the bin size of the histogram, and the comparison of PDFs is not visually effective.

Another important approach is the MoMs. Especially, the NIMs are used to measure the heterogeneity of SAR data in many works by scaling the mean value of the intensity to unity [14, 75, 103, 104]. One can calculate the NIMs of different orders from data samples, and compare them with those of a specific model to see if the model is proper. In the case of PolSAR data, the comparison is accomplished for each polarimetric channel separately. How to combine results of different channels needs to be carefully considered. Furthermore, the method based on NIMs exploits only the intensities of the data, regardless of the correlation between polarimetric channels.

At last, the MKS, also known as log-cumulants, can be used to examine the fit of a distribution to the PolSAR data [10, 12, 26]. They were first proposed by Nicolas [25] to analyze the compounded distributions used to model single-channel SAR data, and later was extended to the case of covariance matrix by Anfinsen et al. [26]. It is demonstrated that MKS are of great value for the analysis of PolSAR data, and that they can be used to derive estimators for distribution parameters with low bias and variance. However, to obtain the sample covariance matrices, a multilooking process of the scattering vectors is required, which may change the distribution of the original data, especially when it comes to high spatial resolution images.

There are some limitations of the mentioned approaches due to the multidimensionality of the PolSAR data. In this chapter, the use of the l_2-norm [105], or Span, of the scattering vectors is suggested for texture analysis, with the following benefits:

- The polarimetric channels are not analyzed separately, and the correlations between polarimetric channels are considered.
- No filter is required which may average out the texture or give rise to mixture in certain scenes like urban areas.
- No estimation of the Equivalent Number of Looks (ENL), which is a challenging task in the analysis of PolSAR data, is needed.
- The Span is polarimetrically invariant, the statistics of the Span are consistent when the scattering vectors are expressed in different polarization basis.

The idea is to map the multidimensional signal to a scalar using the l_2-norm, of which the statistics take into account both the intensities of the polarimetric channels and the correlations between them. Results on both simulated data and real SAR data show that this approach brings advantages in several aspects compared with the method of NIM or matrix variate log-cumulants.

This chapter is organized as follows. First of all, related knowledge is reviewed, including the NIM, and the log-cumulants in the cases of both univariate and matrix variate. Then, the distribution of the l_2-norm is studied based on the scalar texture model, as well as statistics such as normalized moments and log-cumulants. At last, experiments exploiting the l_2-norm are implemented on both simulated data and real SAR data. Conclusions are given at the end.

4.1 Statistical Techniques

The PDF contains all information needed to understand a distribution. An intuitive way to test the fit of a distribution to the samples is the comparison of the PDF and the histogram. In practice, however, this kind of comparison is not effective, especially when it comes to multi-dimenisional signals. Instead, statistics derived from the PDF are of great advantage in this task. This section provides a review of two widely used statistics to analyze the texture of SAR or PolSAR data, the NIMs and the log-cumulants. Several

scalar texture models (Section 3.2.1) are analyzed thanks to their mathematical tractability, including the $\mathcal{K}$, $\mathcal{G}^0$, Kummer-$\mathcal{U}$, $\mathcal{W}$ and $\mathcal{M}$ distribution, with texture following the gamma, inverse gamma, Fisher, beta and beta prime distribution, respectively.

4.1.1 Normalized Intensity Moments

One way to quantitatively evaluate the non-Gaussian behavior of the data is to compute the NIM [75, 103]

$$nim_v\{I\} = \frac{m_v\{I\}}{m_1^v\{I\}} \tag{4.1}$$

where $m_v\{I\}$ refers to the vth order moment of the intensity, and $m_1^v\{I\}$ is the vth power of the mean intensity of a polarimetric channel. On the one hand, for Gaussian distributed data, the intensity, denoted by I_g, follows an exponential distribution [3], and the NIM of the vth order is given by

$$nim_v\{I_g\} = \Gamma(v+1). \tag{4.2}$$

On the other hand, over texture areas modeled by the product model (3.27), the NIM can be factorized into two parts

$$nim_v\{I\} = \frac{m_v\{\tau\}m_v\{I_g\}}{m_1^v\{\tau\}m_1^v\{I_g\}} = m_v\{\tau\}nim_v\{I_g\} \tag{4.3}$$

because the texture component and speckle one are independent, and the mean value of the texture parameter is equal to 1 (Section 3.2). It can be shown that $m_v\{\tau\} \geq 1$ holds for all the texture distributions in Table 4.1. Therefore, the nim_v of textured data is larger than that of Gaussian distributed data when $v > 1$.

The NIM of the second order is widely used. It follows that the second order NIM of the exponential distribution is $nim_2\{I_g\} = 2$, and $nim_2\{I\} > 2$ for all texture distributions in Table 4.1. Therefore, we can determine whether the data can be modeled by a Gaussian distribution or not simply by comparing the $nim_2\{I\}$ estimated from data with 2: if the difference between the estimated value and 2 is very large, the data shows non-gaussianity. The method of NIM requires to analyze the different polarimetric channels separately, as shown in Fig. 4.1, where the moments of the intensity calculated from an ALOS-2 image and a TerraSAR-X image are depicted. Test sites over the sea area are chosen. As we can see, the ALOS-2 data follows a Gaussian distribution, while the TerraSAR-X data shows non-gaussian behavior. In addition, the moments of different polarimetric channels may be different, see Fig. 4.1c for example.

4.1.2 Univariate Log-Cumulants

The Mellin transform is widely used in computer science and signal processing [106]. It is demonstrated that the statistics derived from the Mellin transform can be employed to design estimators for the distribution parameters with low bias and variance [25, 26]. Let $p(x)$ be a function defined on the positive real axis $0 < x < \infty$, the Mellin transform is the operation mapping the function p into the function ϕ defined on the complex plane by the relation [106]:

$$\phi_x(s) = \int_0^\infty x^{s-1}p(x)dx. \tag{4.4}$$

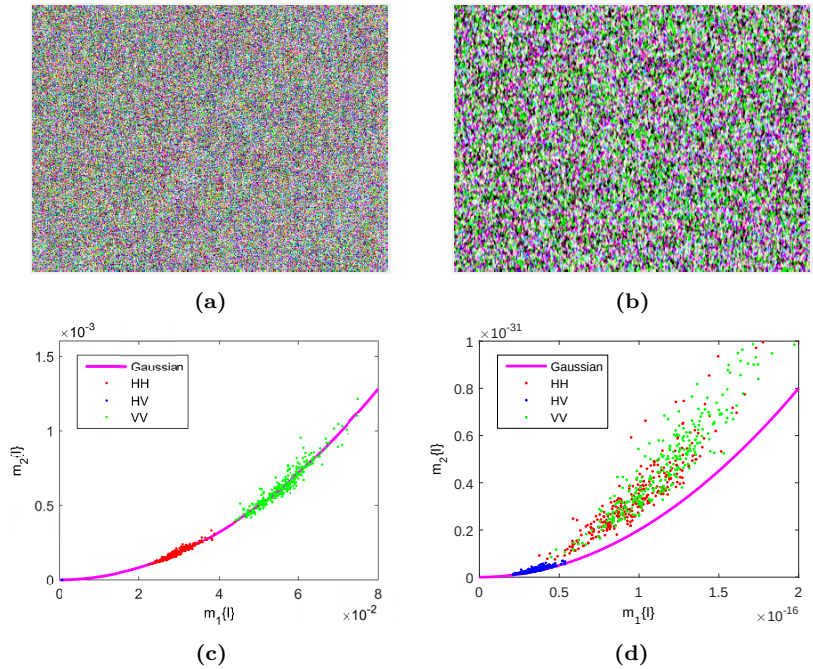

Figure 4.1: Intensity moments on ALOS-2 data and TerraSAR-X data. Both test sites are over the sea area. The test sites are divided into patches of 20×20 pixels, and an estimation of the mean value $m_1\{I\}$ as well as the second order $m_2\{I\}$ are computed for each patch, plotted as a point. (a) Test site of the ALOS-2 data. (b) Test site of the TerraSAR-X data. (c) Moments of the ALOS-2 data. (d) Moments of the TerraSAR-X data.

The function $\phi_x(s)$ is also known as the Mellin kind characteristic function [26], which can be viewed as the $(s-1)$th order moment of a positive random variable. Writing x^{s-1} as $e^{(s-1)\ln x}$ and expanding it using the Taylor series [102], the Mellin Transform can be further written as a formal power series [107]

$$\phi_x(s) = \sum_{v=0}^{\infty} \frac{(s-1)^v}{v!} \mu_v\{x\} \tag{4.5}$$

where the coefficients are known as log-moments [25, 26]

$$\mu_v\{x\} = \int_0^{\infty} (\ln x)^v p(x) dx. \tag{4.6}$$

Let $\varphi_x(s) = \ln \phi_x(s)$, then $\varphi_x(s)$ is called the Mellin kind characteristic function of the second kind [26], that can also be formulated as a formal power series according to the composition of formal power series [107]

$$\varphi_x(s) = \sum_{v=0}^{\infty} \frac{(s-1)^v}{v!} \kappa_v\{x\} \tag{4.7}$$

with coefficients as log-cumulants [25, 26]

$$\kappa_v\{x\} = \mu_v\{x\} - \sum_{k=1}^{v-1} \binom{v-1}{k} \mu_k\{x\}\kappa_{v-k}\{x\}. \tag{4.8}$$

The above equation is known as the combinatorial version of Faà di Bruno's formula, which is denoted by the function $g_v(\mu_1\{x\}, \cdots, \mu_v\{x\})$ in the remainder of this chapter. It shows that the log-cumulants are polynomials of the log-moments. As a matter of fact, the log-moments (or log-cumulants) are the moments (or cumulants) of the random variable mapped at the logarithmic scale, so the rules between the moments and the cumulants also apply to the log-moments and the log-cumulants, for example, we also have

$$\mu_v\{x\} = B_v(\kappa_1\{x\}, \cdots, \kappa_v\{x\}) \tag{4.9}$$

where $B_v(\cdot)$ is the vth complete Bell polynomials [108]. More details about the moments and the cumulants can be found in [109].

According to (4.5) and (4.7), the log-moments and the log-cumulants can be calculated using

$$\mu_v\{x\} = \left.\frac{d^v}{ds^v}\phi_x(s)\right|_{s=1} \tag{4.10}$$

$$\kappa_v\{x\} = \left.\frac{d^v}{ds^v}\varphi_x(s)\right|_{s=1} \tag{4.11}$$

And from independent and identically distributed samples $\{x_i, i = 1, \cdots, N\}$, the log-cumulants can be estimated using the Faà di Bruno's formula, $\hat{\kappa}_v\{x\} = g_v(\hat{\mu}_1\{x\}, \cdots, \hat{\mu}_v\{x\})$ where $\hat{\mu}_v\{x\}$ is the estimated log-moments

$$\hat{\mu}_v\{x\} = \frac{1}{N}\sum_{i=1}^{N}(\ln x)^v. \tag{4.12}$$

We can determine whether a statistical model is proper for the data or not by comparing the theoretical log-cumulants with the estimated ones. A plot called log-cumulant diagram is presented in [25, 26] to visualize the comparison by plotting $\kappa_3\{x\}$ against $\kappa_2\{x\}$ in a plane, where different distributions take up different parts. Table 4.1 shows the log-cumulants of several well known texture distributions making up a complete coverage of the diagram [12], see Fig. 4.2. By plotting the estimated values in the same diagram and checking in which part the values fall, we are able to examine what distribution the data follow.

Furthermore, log-cumulants can be employed to derive parameter estimators. Since the log-cumulants are functions of distribution parameters (see Table 4.1 for example), the parameters can be estimated simply by solving the following equation [110]

$$f(\boldsymbol{\theta}) = \kappa_v\{x\} - \hat{\kappa}_v\{x\} = 0. \tag{4.13}$$

For all texture distributions in Table 4.1, two equations are enough to get a solution of the parameters. Normally the second order and the third order log-cumulants are employed. Though the univariate log-cumulants have many advantages, they are only suitable for analyzing the polarimetric channels one by one. It is worthy reminding that the estimator of the log-cumulants based on the Faà di Bruno's formula is biased [111, 112].

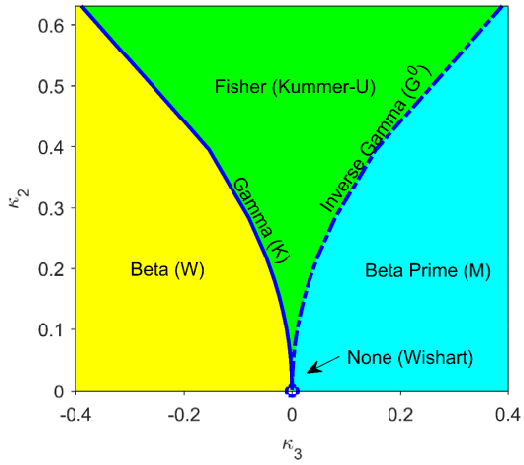

Figure 4.2: A complete coverage of log-cumulant κ_2-κ_3 space. In this diagram, different texture distributions shown in Table 4.1 are plotted. The compound models are called the $\mathcal{K}$, $\mathcal{G}^0$, Kummer-$\mathcal{U}$, $\mathcal{W}$ and $\mathcal{M}$ distributions.

4.1.3 Matrix Variate Log-Cumulants

The univariate log-cumulant is extended to the matrix case by Anfinsen et al. to analyze the sample covariance matrices of PolSAR data [26] with the advantage of considering all the polarimetric channels together. Define the Mellin kind matrix variate characteristic function as

$$\phi_{\mathbf{X}}(s) = \int_{\Omega_+} |\mathbf{X}|^{s-d} p(\mathbf{X}) d\mathbf{X} \tag{4.14}$$

with d denoting the dimension of the sample covariance matrix and Ω_+ the space of positive semi-definite Hermitian matrices, then, the vth-order log-moment and vth-order log-cumulant can be calculated by

$$\begin{aligned} \mu_v\{\mathbf{X}\} &= \frac{d^v}{ds^v}\phi_{\mathbf{X}}(s)\Big|_{s=d} \\ \kappa_v\{\mathbf{X}\} &= \frac{d^v}{ds^v}\varphi_{\mathbf{X}}(s)\Big|_{s=d} \end{aligned} \tag{4.15}$$

where $\varphi_{\mathbf{X}}(s) = \ln \phi_{\mathbf{X}}(s)$. The properties of the univariate log-cumulants and the matrix variate log-cumulants are very similar. The relations (4.8) and (4.9) also apply to the matrix variate log-cumulants [26].

By inserting the PDF of sample covariance matrix as expressed by (3.34) into (4.15), the matrix variate log-cumulant of the sample covariance matrices under the product model assumption can be obtained as [26]

$$\kappa_v\{\mathbf{C}_L\} = \kappa_v\{\mathbf{T}\} + \kappa_v\{\mathbf{Z}_L\}. \tag{4.16}$$

It is a combination of the contribution from the texture and that from the speckle. For the same texture distribution, the matrix variate log-cumulant is an amplified version of

the univariate one [26]

$$\kappa_v\{\mathbf{T}\} = d^v \kappa_v\{\tau\}. \tag{4.17}$$

Some examples of $\kappa_v\{\tau\}$ can be found in Table 4.1. The contribution from the speckle is given by [26]

$$\kappa_v\{\mathbf{Z}_L\} = \psi_d^{(v-1)}(L) + \delta(v-1)(\ln|\mathbf{\Sigma}| - d\ln L) \tag{4.18}$$

where $\mathbf{\Sigma}$ is the covariance matrix, $\delta(\cdot)$ is the Dirac function, and $\psi_d^{(v)}(L)$ is the multivarite extension of the polygamma function defined as

$$\psi_d^{(v)}(L) = \sum_{i=0}^{d-1} \psi^{(v)}(L) \tag{4.19}$$

with $\psi^{(v)}(L) = \frac{d^{v+1}}{dL^{v+1}} \ln\Gamma(L)$ denoting the polygamma function.

The estimation of matrix variate log-cumulants is the same as illustrated in the previous section. For both univariate and matrix variate cases, the covariance of the estimated log-moments is given by [110]

$$\mathrm{Cov}\{\hat{\mu}_v, \hat{\mu}_\nu\} = \frac{1}{N}(\mu_{v+\nu} - \mu_v\mu_\nu). \tag{4.20}$$

Here the curly brackets are omitted because the log-moments can be either univariate or matrix variate, and notations for the log-cumulant in the following text are treated in the same way. As the log-cumulants are the polynomials of the log-moments, once we know the covariances of the log-moments, the variance of the estimated log-cumulant can be calculated using [110]

$$\mathrm{Var}\{\hat{\kappa}_v\} = \nabla g_v^T \mathbf{M}_v \nabla g_v \tag{4.21}$$

where $\mathbf{M}_v$ is the covariance matrix of the log-moments with entries $[\mathbf{M}_v]_{ij} = \mathrm{Cov}(\hat{\mu}_i, \hat{\mu}_j)$, and ∇g_v is the vector of the partial differentials of g_v

$$\nabla g_v = \left[\frac{\partial g_v}{\partial \mu_1}, \cdots, \frac{\partial g_v}{\partial \mu_v}\right]^T. \tag{4.22}$$

The estimation variance depends on the sample size. When the sample size N is not very large, we can employ the bootstrap algorithm [113] to show the statistical behavior of the estimated values. The idea is to resample N times randomly, with replacement, from the original samples to build a new data set called a bootstrap sample. Statistics are then calculated from this bootstrap sample. By generating a large number, saying M, of independent bootstrap samples, we will obtain M estimated statistics, which can be used for further analysis like parameter estimation. The number of bootstrap samples, M, can be very large. With a large number of samples, the estimation error will be reduced. As shown in Fig. 4.3, when increasing the sample size, the estimated values from bootstrap samples (represented by the + marks) become less widely spread in the log-cumulant diagram.

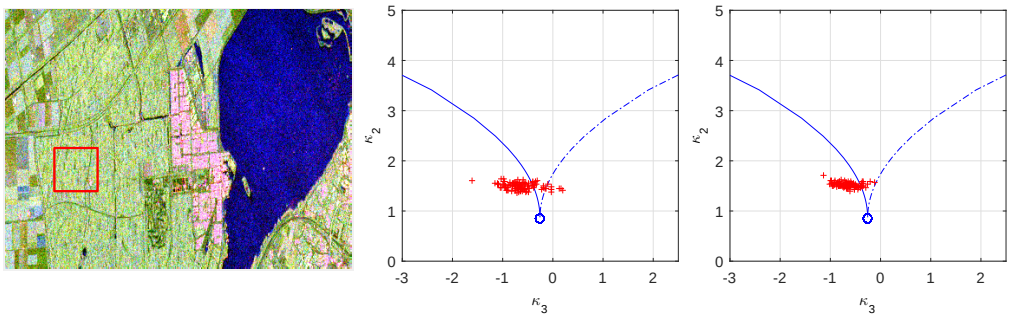

(a) **(b)** **(c)**

Figure 4.3: Matrix variate log-cumulants over a forest region of RADARSAT-2 data. The test region covers 50×50 pixels. Different number of samples, 1200 and 2500, are used to calculate the log-cumulants. 100 bootstrap samples for each test are drawn, each represented by a + mark in (b) and (c). (a) Test region. (b) Log-cumulants estimated using 1200 samples. (c) Log-cumulants estimated using 2500 samples.

Table 4.1: Texture Distributions and Properties

Distribution	Moments $m_v\{\tau\}$	Log-Cumulants $\kappa_v\{\tau\}$
Gamma	$\left(\frac{1}{a}\right)^v \frac{\Gamma(v+\alpha)}{\Gamma(\alpha)}$	$\psi^{(v-1)}(\alpha) - \delta(v-1)\ln\alpha$
Inverse Gamma	$(\alpha-1)^v \frac{\Gamma(\alpha-v)}{\Gamma(\alpha)}$ $\alpha > v$	$(-1)^v\psi^{(v-1)}(\alpha) + \delta(v-1)\ln(\alpha-1)$
Fisher	$\left(\frac{\zeta-1}{\xi}\right)^v \frac{\Gamma(\xi+v)\Gamma(\zeta-v)}{\Gamma(\xi)\Gamma(\zeta)}$ $\zeta > v$	$\psi^{(v-1)}(\xi) + (-1)^v\psi^{(v-1)}(\zeta)$ $+\delta(v-1)\ln\frac{\zeta-1}{\xi}$
Beta	$\left(\frac{\zeta}{\xi}\right)^v \frac{\Gamma(\xi+v)\Gamma(\zeta)}{\Gamma(\xi)\Gamma(\zeta+v)}$	$\psi^{(v-1)}(\xi) - \psi^{(v-1)}(\zeta) + \delta(v-1)\ln\frac{\zeta}{\xi}$
Beta Prime	$\left(\frac{\xi-1}{\zeta-1}\right)^v \frac{\Gamma(\zeta)\Gamma(\xi-v)}{\Gamma(\xi)\Gamma(\zeta-v)}$ $\xi > v, \zeta > v$	$(-1)^v(\psi^{(v-1)}(\xi) - \psi^{(v-1)}(\zeta))$ $+\delta(v-1)\ln\frac{\xi-1}{\zeta-1}$

Notes: $\psi^{(v)}(\cdot)$ is the polygamma function defined as $\psi^{(v)}(x) = \frac{d^{v+1}}{dx^{v+1}}\ln\Gamma(x)$, and $\delta(\cdot)$ is the Dirac function.

4.2 Norm Statistics

4.2.1 Distribution

The l_2-norm, denoted by $\|\mathbf{k}\|_2 = \sqrt{\mathbf{k}^\dagger\mathbf{k}}$, is a non-negative mapping from the d-dimensional complex space $\mathbb{C}^d$ to the set of non-negative real numbers $\mathbb{R}^+$ [105]. The square of the l_2-norm, which can be written as

$$I_{\mathbf{k}} = \mathbf{k}^\dagger\mathbf{k} \tag{4.23}$$

is mainly studied in this chapter, since the square root operation can be avoided. Nevertheless, the statistics of the l_2-norm can be obtained from those of $I_{\mathbf{k}}$ by transformations. $I_{\mathbf{k}}$ is also known as the Span of a scattering vector, which can be interpreted as the total scattered power from a target. It is polarimetrically invariant, independent from the choice of the polarization basis in which the scattering matrix is decomposed. Therefore, the statistics of the Span are consistent when the scattering vectors are expressed in different polarization basis. As a matter of fact, the Span is also employed in some other works [3, 13]. Assuming that the scattering vector can be modeled by the product model (3.27), the square of the l_2-norm can be further rewritten as

$$I_{\mathbf{k}} = \tau I_{\mathbf{z}} \tag{4.24}$$

where $I_{\mathbf{z}} = \mathbf{z}^{\dagger}\mathbf{z}$, independent from τ, is the square l_2-norm of the speckle vector.

Based on the assumption that the speckle vector $\mathbf{z}$ follows a multivariate complex Gaussian distribution with PDF as (3.1), it can be proved that the PDF of $I_{\mathbf{z}}$ is given by (see Appendix A.1)

$$p(I_{\mathbf{z}}) = \sum_{i=1}^{d} \frac{p_i}{\lambda_i} \exp\left(-\frac{I_{\mathbf{z}}}{\lambda_i}\right) \tag{4.25}$$

where $\lambda_i, i = 1, \cdots, d$ are the eigenvalues of the covariance matrix $\mathbf{\Sigma}$, and p_i are the corresponding weights

$$p_i = \frac{\lambda_i^{d-1}}{\prod_{j=1, j\neq i}^{d}(\lambda_i - \lambda_j)}. \tag{4.26}$$

The distribution is known as hyperexponential distribution [114], or mixed exponential distribution, a weighted sum of exponential distributions. The eigenvalues are assumed to be distinct. When there exist repeated eigenvalues, we have to substitute the corresponding exponential distribution for a gamma distribution. One can refer to [115] for more details. In this chapter, the case where there are distinct eigenvalues is mainly discussed.

Provided that the distribution of the texture parameter $p(\tau)$ is known, the PDF of $I_{\mathbf{k}}$ can be calculated by

$$p(I_{\mathbf{k}}; \mathbf{\Sigma}) = \sum_{i=1}^{d} \int \frac{p_i}{\lambda_i} \exp\left(-\frac{I_{\mathbf{k}}}{\tau\lambda_i}\right) \frac{1}{\tau} p(\tau) d\tau. \tag{4.27}$$

For instance, when the texture parameter is gamma, inverse gamma or Fisher distributed, the PDFs can be calculated as shown in Table 4.2. These distributions are univariate ones. Therefore, it is much easier to use them for texture analysis than those of the sample covariance matrix or scattering vector.

4.2.2 Normalized Moments

It is known that the moments of a mixture model is a weighted average of those of the mixing components [101]. The vth order moment of the speckle $I_{\mathbf{z}}$, therefore, can be written as the combination of the vth order moments of exponential distributions [86]

$$m_v\{I_{\mathbf{z}}\} = \Gamma(v+1) \sum_{i=1}^{d} p_i \lambda_i^v \tag{4.28}$$

Table 4.2: Distribution of the l_2-Norm

Texture	PDF of the l_2-Norm, $p(I_{\mathbf{k}})$
Gamma	$\frac{2\alpha^{\frac{\alpha+1}{2}}}{\Gamma(\alpha)} \sum_{i=1}^{d} \frac{p_i}{\lambda_i} \left(\frac{I_{\mathbf{k}}}{\lambda_i}\right)^{\frac{\alpha-1}{2}} K_{\alpha-1}\left(2\sqrt{\alpha \frac{I_{\mathbf{k}}}{\lambda_i}}\right)$
Inverse Gamma	$\alpha(\alpha-1)^{\alpha} \sum_{i=1}^{d} \frac{p_i}{\lambda_i} \left(\alpha - 1 + \frac{I_{\mathbf{k}}}{\lambda_i}\right)^{-\alpha-1}$
Fisher	$\frac{\Gamma(\xi+\zeta)}{\Gamma(\xi)} \frac{\xi\zeta}{\zeta-1} \sum_{i=1}^{d} \frac{p_i}{\lambda_i} U\left(1+\zeta, 2-\xi, \frac{\xi}{\zeta-1}\frac{I_{\mathbf{k}}}{\lambda_i}\right)$
Beta	$\frac{\Gamma(\zeta)}{\Gamma(\xi)} \left(\frac{\xi}{\zeta}\right)^{\frac{\xi}{2}} \sum_{i=1}^{d} \frac{p_i}{\lambda_i} \left(\frac{I_{\mathbf{k}}}{\lambda_i}\right)^{\frac{\xi-2}{2}} \exp\left(-\frac{\xi}{2\zeta}\frac{I_{\mathbf{k}}}{\lambda_i}\right) W_{\frac{2+\xi-2\zeta}{2}, \frac{\xi-1}{2}}\left(\frac{\xi}{\zeta}\frac{I_{\mathbf{k}}}{\lambda_i}\right)$
Beta Prime	$\frac{(\zeta-1)\xi}{\zeta(\xi-1)} \sum_{i=1}^{d} \frac{p_i}{\lambda_i} M\left(\xi+1, \zeta+1, -\frac{\zeta-1}{\xi-1}\frac{I_{\mathbf{k}}}{\lambda_i}\right)$

Notes: K_v is the modified Bessel function of the second kind of order v, U is the confluent hypergeometric function of the second kind (Kummer U function), W is the Whittaker W function, and M is the confluent hypergeometric function of the first kind (Kummer M function).

with λ_i denoting the eigenvalues, and p_i given by (4.26). Let $h_v(\lambda_1, \cdots, \lambda_d) = \sum_{i=1}^{d} p_i \lambda_i^v$, as shown in [116], it can be further rewritten as

$$h_v(\lambda_1, \cdots, \lambda_d) = \sum_{1 \le i_1 \le \cdots \le i_v \le d} \lambda_{i_1} \cdots \lambda_{i_v} \tag{4.29}$$

which is known as the Complete Homogeneous Symmetric Polynomials (CHSP) [117]. Some examples of the CHSP when $d = 3$ are listed as follows

$$h_1(\lambda_1, \lambda_2, \lambda_3) = \lambda_1 + \lambda_2 + \lambda_3 \tag{4.30}$$

$$h_2(\lambda_1, \lambda_2, \lambda_3) = \lambda_1^2 + \lambda_2^2 + \lambda_3^2 + \lambda_1\lambda_2 + \lambda_1\lambda_3 + \lambda_2\lambda_3 \tag{4.31}$$

$$\begin{aligned} h_3(\lambda_1, \lambda_2, \lambda_3) = {} & \lambda_1^3 + \lambda_2^3 + \lambda_3^3 + \lambda_1^2\lambda_2 + \lambda_1^2\lambda_3 + \lambda_2^2\lambda_1 \\ & + \lambda_2^2\lambda_3 + \lambda_3^2\lambda_1 + \lambda_3^2\lambda_2 + \lambda_1\lambda_2\lambda_3 \end{aligned} \tag{4.32}$$

Various calculations become easier based on (4.29) as there are only multiplications and additions. For instance, the asymptotic limits when there are repeated eigenvalues can be easily computed.

When the covariance matrix $\mathbf{\Sigma}$ is scaled by a factor, the moments shown in (4.28) will change accordingly. To eliminate this effect and make the moments under circumstances of different covariance matrices comparative, we normalize the eigenvalues by

$$\tilde{\lambda}_i = \frac{\lambda_i}{\sum_{k=1}^{d} \lambda_k} \tag{4.33}$$

and substitute them for the eigenvalues in (4.28), the normalized moment of the vth order is obtained

$$nm_v\{I_{\mathbf{z}}\} = \Gamma(v+1) h_v(\tilde{\lambda}_1, \cdots, \tilde{\lambda}_d) \tag{4.34}$$

which is found to be the fraction of the vth order moment and the vth power of the mean

$$nm_v\{I_{\mathbf{z}}\} = \frac{m_v\{I_{\mathbf{z}}\}}{m_1^v\{I_{\mathbf{z}}\}}. \tag{4.35}$$

In the case of $d = 1$, the normalized moment is reduced to the NIM of single channel data as expressed by (4.1).

For Gaussian distributed speckle, the vth order normalized moment is not a fixed value, it varies in a range instead. The value reveals the polarimetric information to some extent. Let $\tilde{\lambda}_i = 1/d, i = 1, \cdots, d$, meaning that the polarimetric scattering Entropy is equal to 1 [3], the smallest value of the normalized moment is obtained from (4.29)

$$\min\{nm_v\{I_{\mathbf{z}}\}\} = \frac{\Gamma(v+d)}{d^v\Gamma(d)}. \tag{4.36}$$

When the polarimetric scattering Entropy is equal to 0 ($\tilde{\lambda}_i = 1$ and $\tilde{\lambda}_j = 0, \forall j \neq i$), the normalized moments will reach the upper boundary

$$\max\{nm_v\{I_{\mathbf{z}}\}\} = \Gamma(v+1). \tag{4.37}$$

Taking into account the texture part, the vth order moment of the l_2-norm of the total scattering vector can be written as

$$m_v\{I_{\mathbf{k}}\} = m_v\{\tau\}m_v\{I_{\mathbf{z}}\} \tag{4.38}$$

since the texture and the speckle in (4.24) are independent. Under the assumption that the mean value of texture parameter is equal to 1, the normalized moments of $I_{\mathbf{k}}$ are then

$$nm_v\{I_{\mathbf{k}}\} = \frac{m_v\{I_{\mathbf{k}}\}}{m_1^v\{I_{\mathbf{k}}\}} = m_v\{\tau\}nm_v\{I_{\mathbf{z}}\}. \tag{4.39}$$

Different distributions for the texture parameter will result into different values. As a consequence, the normalized moments could be employed to reveal the texture information, besides the polarimetric information of PolSAR data.

Given N independent and identically distributed samples $\{\mathbf{k}_i, i = 1, \cdots, N\}$, the sample moments can be estimated using

$$\hat{m}_v\{I_{\mathbf{k}}\} = \frac{1}{N}\sum_{i=1}^{N}(\mathbf{k}_i^\dagger\mathbf{k}_i)^v \tag{4.40}$$

and the normalized moments by

$$n\hat{m}_v\{I_{\mathbf{k}}\} = \frac{\hat{m}_v\{I_{\mathbf{k}}\}}{\hat{m}_1^v\{I_{\mathbf{k}}\}}. \tag{4.41}$$

This estimator is biased [118, 119]. As shown in Appendix A.2, the bias is of the order $O(1/N)$

$$B = \frac{1}{2N}(v(v+1)\cdot nm_2\{I_{\mathbf{k}}\}nm_v\{I_{\mathbf{k}}\} - 2v\cdot nm_{v+1}\{I_{\mathbf{k}}\} - v(v-1)\cdot m_v\{I_{\mathbf{k}}\}). \tag{4.42}$$

When the sample size N is large, the mean value and the variance of $n\hat{m}_v\{I_{\mathbf{k}}\}$ can be approximated by

$$\mathrm{E}\left\{n\hat{m}_v\{I_{\mathbf{k}}\}\right\} \approx \frac{m_v\{I_{\mathbf{k}}\}}{m_1^v\{I_{\mathbf{k}}\}} = nm_v\{I_{\mathbf{k}}\} \tag{4.43}$$

$$\begin{aligned}\mathrm{Var}\left\{n\hat{m}_v\{I_{\mathbf{k}}\}\right\} \approx \frac{1}{N}[&nm_{2v}\{I_{\mathbf{k}}\} - (v-1)^2 \cdot nm_v^2\{I_{\mathbf{k}}\} \\ &-2v \cdot nm_v\{I_{\mathbf{k}}\}nm_{v+1}\{I_{\mathbf{k}}\} + v^2 \cdot nm_2\{I_{\mathbf{k}}\}nm_v^2\{I_{\mathbf{k}}\}]\end{aligned} \tag{4.44}$$

See Appendix A.2 for more details. Simple goodness-of-fit tests can be designed with the estimator and the estimation variance.

4.2.3 Log-Cumulants

As shown in the previous section, the moments can be viewed as functions of the order v, which are distinct for different distributions. They can be employed to identify data models therefore. Letting $v = s - 1$ and computing the logarithm on both sides of (4.38) gives the following relation:

$$\varphi_{I_{\mathbf{k}}}(s) = \varphi_{\tau}(s) + \varphi_{I_{\mathbf{z}}}(s) \tag{4.45}$$

where $\varphi_x(s)$ is the Mellin kind characteristic function of the second kind (Section 4.1.2). The log-cumulant can be obtained further by calculating the vth order differential and setting $s = 1$

$$\kappa_v\{I_{\mathbf{k}}\} = \kappa_v\{\tau\} + \kappa_v\{I_{\mathbf{z}}\}. \tag{4.46}$$

It is an addition of the values from the texture part and the speckle part. The log-cumulants of the texture part are well studied in [25, 26], and the results of some widely studied distributions for the texture are listed in Table 4.1. For the speckle part, (4.28) shows that the Mellin kind characteristic function of the second kind is

$$\varphi_{I_{\mathbf{z}}}(s) = \ln\Gamma(s) + \ln h_{s-1}(\lambda_1, \cdots, \lambda_d), \tag{4.47}$$

and the log-cumulants can be calculated by (see Appendix A.3)

$$\kappa_v\{I_{\mathbf{z}}\} = \psi^{(v-1)}(1) + \beta_v \tag{4.48}$$

where $\psi^{(v)}(\cdot)$ is the polygamma function (4.19), and β_v is solved recursively using

$$\beta_v = \tilde{h}(v) - \sum_{k=1}^{v-1} \binom{v-1}{k} \tilde{h}(k)\beta_{v-k} \tag{4.49}$$

with $\tilde{h}(v) = \sum_{i=1}^{d} p_i(\ln\lambda_i)^v$. A great advantage of the log-cumulants for texture analysis is that the contribution of the texture and the speckle can be separated using the logarithm operation [26]. The log-cumulants of the l_2-norm are calculated from the scattering vectors directly. As a result, no filtering is required to obtain the sample covariance matrices, where the procedure may change the statistical properties of the original data.

To test the fit of a model to PolSAR data using the log-cumulants, we can employ the biased estimator based on the Faà di Bruno's formula as shown in Section 4.1.2, or the unique unbiased estimator with minimum variance, k-statistics [109, 111]. Given N

independent and identically distributed samples $\{\mathbf{k}_i, i = 1, \cdots, N\}$, the k-statistics of the first three orders are given by [109]

$$\hat{\kappa}_1\{I_\mathbf{k}\} = \frac{M_1}{N} \tag{4.50}$$

$$\hat{\kappa}_2\{I_\mathbf{k}\} = \frac{NM_2 - M_1^2}{N(N-1)} \tag{4.51}$$

$$\hat{\kappa}_3\{I_\mathbf{k}\} = \frac{2M_1^3 - 3NM_1M_2 + N^2M_3}{N(N-1)(N-2)} \tag{4.52}$$

where M_v is the sums of the vth powers

$$M_v = \sum_{i=1}^{N} \left[\ln(\mathbf{k}_i^\dagger \mathbf{k}_i)\right]^v. \tag{4.53}$$

The variance of the first three k-statistics are given by [109]

$$\mathrm{Var}\{\hat{\kappa}_1\{I_\mathbf{k}\}\} = \frac{\kappa_2\{I_\mathbf{k}\}}{N} \tag{4.54}$$

$$\mathrm{Var}\{\hat{\kappa}_2\{I_\mathbf{k}\}\} = \frac{\kappa_4\{I_\mathbf{k}\}}{N} + \frac{2\kappa_2^2\{I_\mathbf{k}\}}{N-1} \tag{4.55}$$

$$\mathrm{Var}\{\hat{\kappa}_3\{I_\mathbf{k}\}\} = \frac{\kappa_6\{I_\mathbf{k}\}}{N} + \frac{9\kappa_2\{I_\mathbf{k}\}\kappa_4\{I_\mathbf{k}\}}{N-1} + \frac{9\kappa_3^2\{I_\mathbf{k}\}}{N-1} + \frac{6N\kappa_2^3\{I_\mathbf{k}\}}{(N-1)(N-2)} \tag{4.56}$$

In addition, the covariance of the second order and third order k-statistics is [109]

$$\mathrm{Cov}\{\hat{\kappa}_2\{I_\mathbf{k}\}, \hat{\kappa}_3\{I_\mathbf{k}\}\} = \frac{\kappa_5\{I_\mathbf{k}\}}{N} + \frac{6\kappa_2\{I_\mathbf{k}\}\kappa_3\{I_\mathbf{k}\}}{N-1}. \tag{4.57}$$

K-statistics of higher orders can be found in Appendix A.4 or [109]. The second order and third order log-cumulants are widely used to determine the texture distribution. Let $\boldsymbol{\kappa} = [\kappa_2\{I_\mathbf{k}\}, \kappa_3\{I_\mathbf{k}\}]^T$ and $\hat{\boldsymbol{\kappa}} = [\hat{\kappa_2}\{I_\mathbf{k}\}, \hat{\kappa_3}\{I_\mathbf{k}\}]^T$, then the covariance matrix of $\hat{\boldsymbol{\kappa}}$ is

$$\mathbf{K} = \begin{bmatrix} \mathrm{Var}\{\hat{\kappa}_2\{I_\mathbf{k}\}\} & \mathrm{Cov}\{\hat{\kappa}_2\{I_\mathbf{k}\}, \hat{\kappa}_3\{I_\mathbf{k}\}\} \\ \mathrm{Cov}\{\hat{\kappa}_2\{I_\mathbf{k}\}, \hat{\kappa}_3\{I_\mathbf{k}\}\} & \mathrm{Var}\{\hat{\kappa}_3\{I_\mathbf{k}\}\} \end{bmatrix}. \tag{4.58}$$

Consider the test statistic

$$Q_p = (\hat{\boldsymbol{\kappa}} - \boldsymbol{\kappa})^T \mathbf{K}^{-1} (\hat{\boldsymbol{\kappa}} - \boldsymbol{\kappa}), \tag{4.59}$$

the asymptotic distribution follows as [110]

$$Q_p \xrightarrow{D} \chi^2(2) \tag{4.60}$$

where $\chi^2(p)$ is the χ^2 distribution with degrees of freedom equal to p. The PDF is given by [86]

$$p(x; p) = \frac{x^{p/2-1} e^{-x/2}}{2^{p/2}\Gamma(p/2)}. \tag{4.61}$$

For a significance level α_c, we can calculate the acceptance region of the $\hat{\boldsymbol{\kappa}}$, saying z_{α_c}, via $p(Q_p > z_{\alpha_c}) = \alpha_c$. The comparison of the theoretical log-cumulants with the estimated ones thus can be quantitatively evaluated.

Table 4.3: KS Distance of Simulated Data

	None	Gamma	InvGamma	Fisher	Beta	Beta'
KS1	0.0040	0.0020	0.0065	0.0069	0.0072	0.0021
KS2	0.0040	0.0574	0.0683	0.0889	0.0249	0.0237

4.3 Experimental Results

Experiments on both simulated data and real SAR data are designed. With the former, we can validate the distributions and statistics of the l_2-norm derived in the previous section, whereas the latter aims to demonstrate the applications as well as advantages of the l_2-norm to SAR data analysis.

4.3.1 Simulated Data

First, experiments are carried out to validate the PDFs in Table 4.2. Simulated data with different texture distributions are tested, including the gamma distribution (`Gamma`), the inverse gamma distribution (`InvGamma`), the Fisher distribution (`Fisher`), the beta distribution (`Beta`) and the beta prime distribution (`Beta'`), as well as constant values (`None`). The parameters for the gamma and inverse gamma distributions are $\alpha = 8$, and $\xi = 8, \zeta = 12$ for the other three ones. All the data share the same covariance matrix

$$\mathbf{C}_1 = 10^{-3} \times \begin{bmatrix} 161 & -7-4j & 39-j \\ -7+4j & 82 & -4+4j \\ 39+j & -4-4j & 100 \end{bmatrix} \tag{4.62}$$

which is estimated from a forest area of an AirSAR image acquired over the Netherlands.

The PDFs in Table 4.2 are calculated, and compared with the histograms of the simulated data. The result is shown in Fig. 4.4, where the solid lines stand for the PDFs, and the points represent the histograms. It shows that the histograms conform to the corresponding PDFs closely, and different distributions can be discriminated by the PDFs, though not effectively. This is also validated by the KS distance, which is defined as

$$KS = \sup_x |F_n(x) - F(x)|. \tag{4.63}$$

Here $F(x)$ is the cumulative distribution function, F_n is the empirical distribution for n independently and identically distributed observations, and sup is the supremum of the set of distances. The results are shown in Table 4.3. The first row refers to the distances between the histograms and the corresponding PDFs (`KS1`), and as a reference, the second row shows the distances from the histograms to Gaussian PDF (`KS2`). As it can be seen, the `KS1` is smaller than 0.01 for all the simulated data, while `KS2` is larger than 0.02 for data with textures. The values confirm that the histograms can be employed for texture analysis. It is necessary to remind that the KS distance depends on the bin size to calculate the histogram, therefore, the results are meaningful only when the bin size is same.

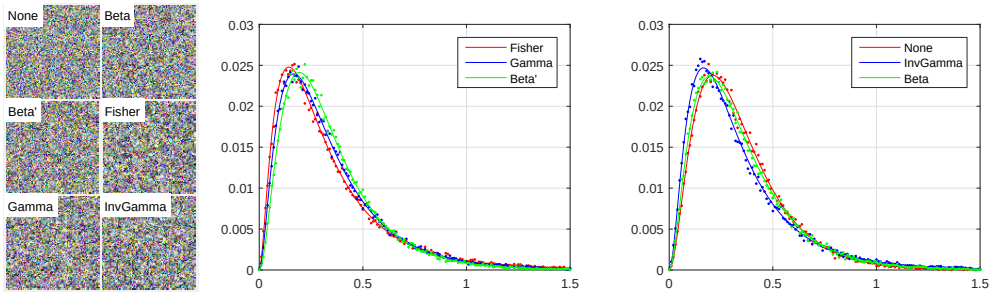

Figure 4.4: Histograms and PDFs of the l_2-norms. The solid lines represent the PDFs in Table 4.2, and the points the histograms of simulated data. (a) Simulated data. (b) Gamma, Fisher, and beta prime distributed texture. (c) Inverse gamma, beta distributed texture as well as non-texture.

The Entropy given by the covariance matrix $\mathbf{C}_1$ in (4.62) is 0.9275, which is high as the correlation coefficients between polarimetric channels are very small. By keeping the intensities and increasing the correlation, another two covariance matrices, with Entropy 0.6940 and 0.5187 respectively, are obtained

$$\mathbf{C}_2 = 10^{-3} \times \begin{bmatrix} 161 & 79.6 - 46j & 39 - j \\ 79.6 + 46j & 82 & -4 + 4j \\ 39 + j & -4 - 4j & 100 \end{bmatrix} \tag{4.64}$$

$$\mathbf{C}_3 = 10^{-3} \begin{bmatrix} 161 & 79.6 - 46j & 39 - j \\ 79.6 + 46j & 82 & 51.2 + 51.2j \\ 39 + j & -51.2 - 51.2j & 100 \end{bmatrix} \tag{4.65}$$

Gaussian distributed data are simulated using these covariance matrices, each containing 40000 samples. The normalized moments up to the fifth order are shown in Fig. 4.5b, in which the theoretical values are represented by lines, and estimated ones by asterisks. It shows that the estimated values fit the theoretical ones very well, and data with different Entropy are distinguished in the plot, laying between the two boundaries representing Entropy 0 and Entropy 1. Table 4.4 shows the distances between the estimated normalized moments and theoretical ones, $d = |nm_v - n\hat{m}_v|$, as well as the square root of the estimation variance, $\sigma = \sqrt{\mathrm{Var}\{n\hat{m}_v\}}$. Based on the 3σ rule, we can judge that the data is characterized by the corresponding distribution, as all $d < 3\sigma$. In addition, it shows that the estimation variance of higher order normalized moments, the fifth order for example, is very large, therefore, higher orders should be avoided to data analysis unless the sample size is very large.

Normalized moments are also tested on simulated data with different texture distributions, including the gamma, the inverse gamma and the Fisher distribution. Texture distribution parameters (see Table 4.1) are given by $\alpha = 8$ and $\xi = 8, \zeta = 12$, and covariance matrix by (4.62). The result is shown in Fig. 4.5c. The values of Gaussian distributed data is also plotted as a reference. The quantitative assessment based on the estimation variance is shown in Table 4.5. Similar results are obtained and it demonstrates again

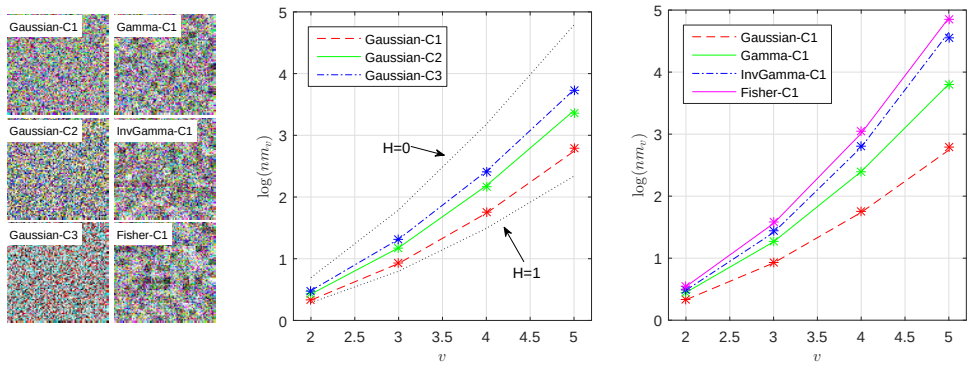

(a) **(b)** **(c)**

Figure 4.5: Normalized moments of the l_2-norms on simulated data. The theoretical values are represented by lines, and estimated ones by asterisks. (a) Pauli decomposition of simulated data. (b) Gaussian distributed data with different Entropy. (c) Data with different textures but the same covariance matrix (Entropy of 0.9275).

Table 4.4: Estimation Variance and Distance on Homogeneous Data

Tests	Distance	$v=2$	$v=3$	$v=4$	$v=5$
$\mathbf{C}_1$	d	0.0025	0.0189	0.1236	0.7691
	3σ	0.0106	0.0638	0.3395	1.9337
$\mathbf{C}_2$	d	0.0005	0.0126	0.1513	1.3032
	3σ	0.0153	0.1073	0.6927	4.8918
$\mathbf{C}_3$	d	0.0010	0.0143	0.0981	0.5775
	3σ	0.0182	0.1379	0.9769	7.6351

Table 4.5: Estimation Variance and Distance on Textured Data

Tests	Distance	$v=2$	$v=3$	$v=4$	$v=5$
Gamma	d	0.0013	0.0080	0.0077	0.6125
	3σ	0.0196	0.1701	1.5148	16.7464
InvGamma	d	0.0160	0.1074	0.3839	8.1539
	3σ	0.0301	0.4614	-	-
Fisher	d	0.0193	0.1490	0.7832	3.3680
	3σ	0.0335	0.4588	9.2493	436.6224

that the normalized moments can be employed to determine the distribution of SAR data. That textured data have a larger normalized moment than Gaussian distributed data can be also observed. In Table 4.5, the variance of the 4th and 5th order normalized moments for the inverse gamma distributed texture is not defined, as the variance involves 8th and 10th order moments which do not exist when $\alpha = 8$, see the expression in Table 4.1.

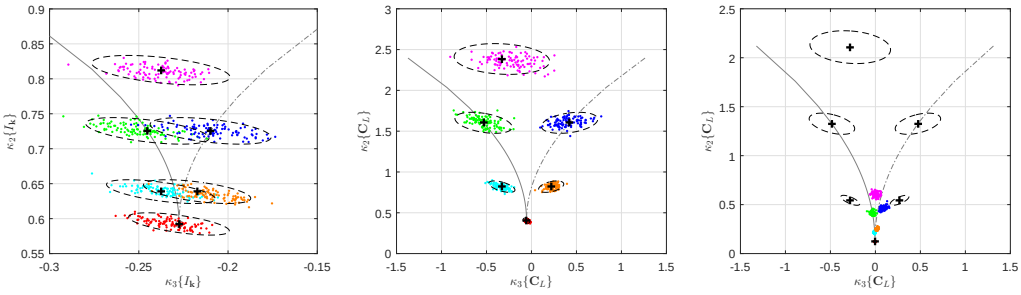

(a) **(b)** **(c)**

Figure 4.6: Log-cumulants of the second and the third order. The point clouds represent the estimated values using bootstrap, and the + markers represent the theoretical values. (a) Log-cumulants of the l_2-norms. (b) Matrix variate log-cumulants with 3×3 filtering window. (c) Matrix variate log-cumulants with 5×5 filtering window.

In addition to the normalized moments, the log-cumulants of the l_2-norms are calculated. Again, simulated data with texture distributions in Table 4.1, as well as non-texture data, are tested. The result is shown in Fig. 4.6a. For each trial, 100 κ_3-κ_2 pairs are estimated using the bootstrap method [26], with each bootstrap sample consisting of 20000 pixels. The estimated pairs are plotted in the log-cumulant diagram (point clouds), and are compared with the theoretical values (the + markers). The acceptance regions with significance level $\alpha_c = 0.05$ are also depicted (the black ellipses). As we can see, the estimated log-cumulants are congruent with the theoretical ones, as there are only several points falling out of the ellipses.

Multilook processing is applied to the scattering vectors using two different window sizes, 3×3 and 5×5 pixels, and with the obtained sample covariance matrices, matrix variate log-cumulants are estimated. The results are shown in Fig. 4.6b and Fig. 4.6c. As the correlation length of the simulated texture is 3 pixel, the sample matrix variate log-cumulants are different completely. With a window size smaller or equal than the correlation length, the estimated statistics are in agreement with the theoretical ones. While a large window size will average out the texture significantly, resulting in Gaussian statistics. Therefore, with the matrix variate log-cumulants, the choice of the window size is critical in some circumstances.

From Fig. 4.6a and Fig. 4.6b, we can see that the matrix variate log-cumulants are well separated for different distributions, while the log-cumulants based on the l_2-norm are overlapped for some distributions. This is because the matrix variate log-cumulants of the texture part are scaled by a non-linear function of the order as shown in (4.17), and the difference between distributions is amplified. From this point of view, the matrix variate log-cumulants are of advantage when the multilook window size is properly chosen.

4.3.2 Real SAR Data

Real SAR data including RADARSAT-2 Fine Quad-Pol data (`RST2`) as well as F-SAR X-band full-pol data (`FSAR`) from the DLR are analyzed using the l_2-norm. The two data

have quite different spatial resolutions, $11.1m \times 7.6m$ (Range $\times$ Azimuth) for the RST2 data, and $0.25m \times 0.25m$ for the FSAR data. Original data are in the single look complex format.

Three ROIs over the crops area from each data are tested, see Fig. 4.7c and Fig. 4.7d. For the RST2 data, each ROI covers 50×50 pixels. It can be seen that the ROIs are represented by very different colors from the Pauli decomposition, implying that the polarimetric information they convey are different. The ROIs in the FSAR data are much larger, each covers 200×200 pixels. Compared with the appearance of the RST2 data, the differences among these ROIs are not so significant. The Pauli decomposition shows that the ROIs in both image are very homogeneous, no appreciable texture is observed.

The normalized moments are computed on all ROIs, and the values are compared with those of Gaussian distributions, since the normalized moments can be used to evaluate the non-gaussianity as demonstrated before. Because the true covariance matrices are not known, they are estimated using the fixed point estimator (3.32) which is proved to be robust on both homogeneous and textured areas. The results are shown in Fig. 4.7c and Fig. 4.7d. As we can see, the normalized moments estimated from the RST2 data fit those calculated using the covariance matrix very well, and they are well separated between the boundaries representing Entropy 0 and Entropy 1. It is rational to conclude that these ROIs can be modeled by Gaussian distributions. In contrast, the result on the FSAR data shows different behaviors. First of all, all the ROIs seem to have similar Entropy. Applications such as classification based on the Entropy, as a consequence, may not work. Secondly, there are large discrepancies between the estimated values and the theoretical values for all ROIs. Apparently, Gaussian distributions are not accurate any more. Statistical information, or texture information, is of great value to identify different types of crops in this case.

Further validations using the log-cumulants based on the l_2-norm are performed, see Fig. 4.8a and Fig. 4.8b. Here only the impact from the texture part is shown by removing the contribution of the speckle part in (4.46). This is because the contribution from the speckle part is not the same for different ROIs since the covariance matrices of these ROIs are different. The acceptance regions of Gaussian distributions with significance level $\alpha_c = 0.05$ are also plotted. Fig. 4.8a shows that most of the points fall inside the corresponding ellipse, indicating that Gaussian distributions are proper for these ROIs. For the FSAR data, it seems that the ROI 1 and ROI 3 can be modeled by beta prime distributed textures, whereas the inverse gamma distribution is proper for the ROI 2. That the width of the acceptance regions depends on the number of samples gives rise to the large difference in the sizes of the ellipses in Fig. 4.8a and Fig. 4.8b, as there are much more pixels in the ROIs of the FSAR data than the RST2 ROIs.

The matrix variate log-cumulants are also computed for the FSAR data, after applying a multilook process to the scattering vectors with a 5×5 sliding window. Each bootstrap sample contains 500 sample covariance matrices. And the ENL is estimated as 6.4885. From Fig. 4.8c, we can see that most points from ROI 2 and ROI 3 fall inside the black ellipse, which refers to the acceptance regions of a Wishart distribution with significance level $\alpha_c = 0.05$. It demonstrates again that the non-gaussianity can be removed during the multilook processing. To obtain the correct statistical properties, filtering should be avoided as much as possible.

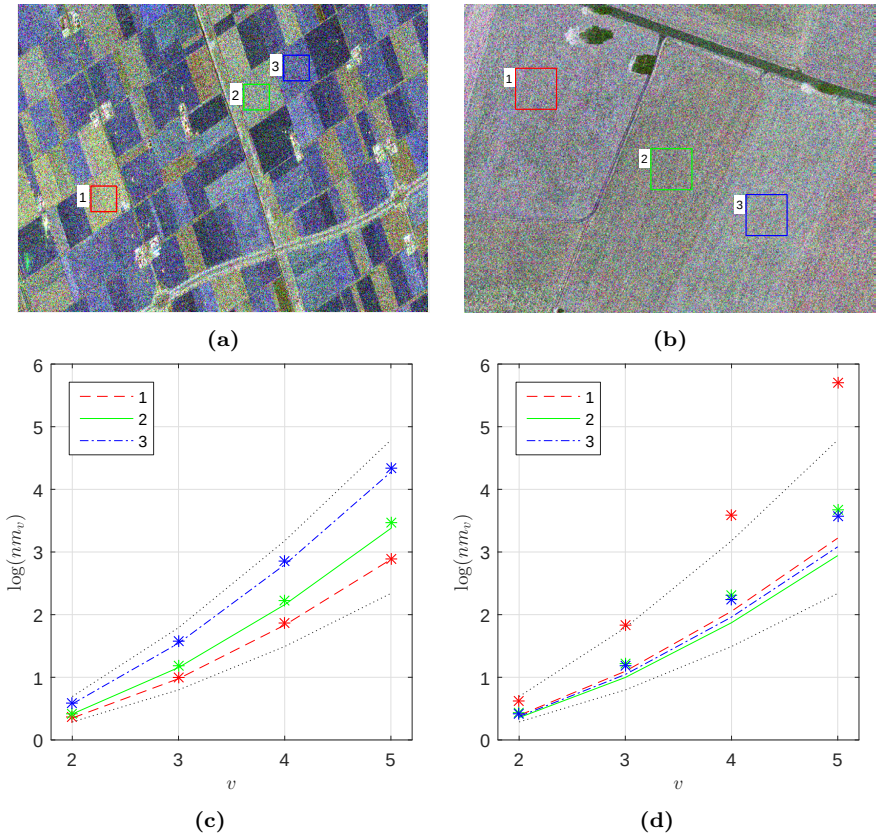

Figure 4.7: Normalized moments on `RST2` data (the first column) and `FSAR` data (the second column). The theoretical values are represented by lines, and estimated ones by asterisks. (a) and (b), Pauli decomposition and test areas. (c) and (d), Normalized moments both calculated using the covariance matrix and estimated from the data samples.

The calculation of matrix variate log-cumulants involves the estimation of the ENL, which is a difficult task in the analysis of PolSAR data. One needs to select a Gaussian distributed homogeneous area manually, and then use the trace moment-based estimator or log-determinant moment-based estimator [120]. Another option is the texture-invariant estimator [121] suggested by Liu et al., which can be applied on textured data. But it requires that the texture is constant in the multilook window, which is not guaranteed in all circumstances, the crops area of the `FSAR` data for example. On the contrary, the log-cumulants of the l_2-norms depends on the covariance matrix instead of the ENL, which can be estimated either on homogeneous area or textured area using a sample mean estimator or the fixed point estimator (3.32).

Apart from the crops areas, two forest sites from the `FSAR` data are analyzed, one is with short trees, and the other with high trees. Six ROIs of 200×200 pixels are selected for each test site, see Fig. 4.9. The Pauli decomposition shows that the test regions are very heterogeneous due to the alternative appearance of the strong backscattering from the crowns of trees and the weak one from the shadows.

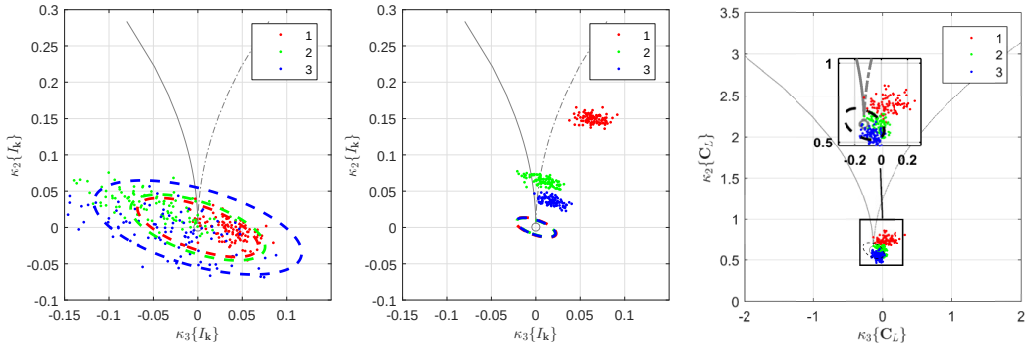

(a) **(b)** **(c)**

Figure 4.8: Log-cumulants of the l_2-norms on the `RST2` data and `FSAR` data. Estimated values are plotted as points and the acceptance regions as ellipses. (a) Log-cumulants of the l_2-norms on `RST2` data after removing the effect of the speckle part. (b) Log-cumulants of the l_2-norms on `FSAR` data after removing the effect of the speckle part. (c) Matrix variate log-cumulant of the sample covariance matrices on `FSAR` data after a 5×5 filtering.

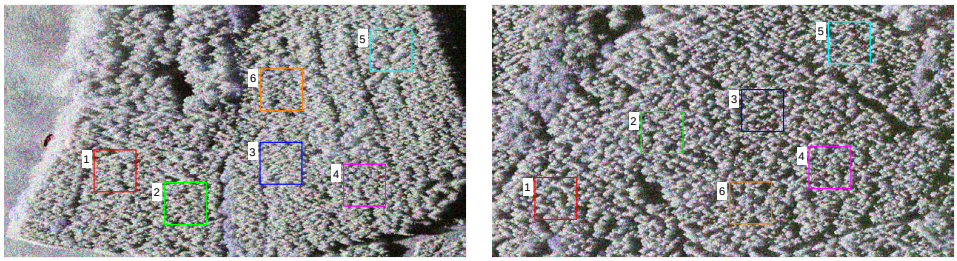

(a) **(b)**

Figure 4.9: Test sites of forest areas on the `FSAR` data. Two different types of forest are tested. (a) Pauli decomposition and test areas of the first site. (b) Pauli decomposition and test areas of the second site.

Log-cumulants of the l_2-norms, as well as matrix variate log-cumulants are calculated. Fig. 4.10a and Fig. 4.10b show the values of the the first site, and those of the second site are in Fig. 4.10c and Fig. 4.10d. It seems that the textures of all the ROIs can be modeled by Fisher distributions. The absolute values of κ_2 and κ_3 are very large. This implies that there exist strong fluctuations in the radar cross sections over these areas. We can also see that different ROIs from the same test site have similar results, for example, the κ_2 of the first site is less than 1.5 and the κ_3 is less than 0, which are well separated from the second site, where the κ_2 is larger than 1.5 and κ_3 larger than 0. This means the forests can be further classified into different types using statistical information. The textures are not affected too much by the multilook processing, see Fig. 4.10a and Fig. 4.10b for example. That the window size of the filtering, 5×5 pixels, is smaller than the size of trees could be the reason.

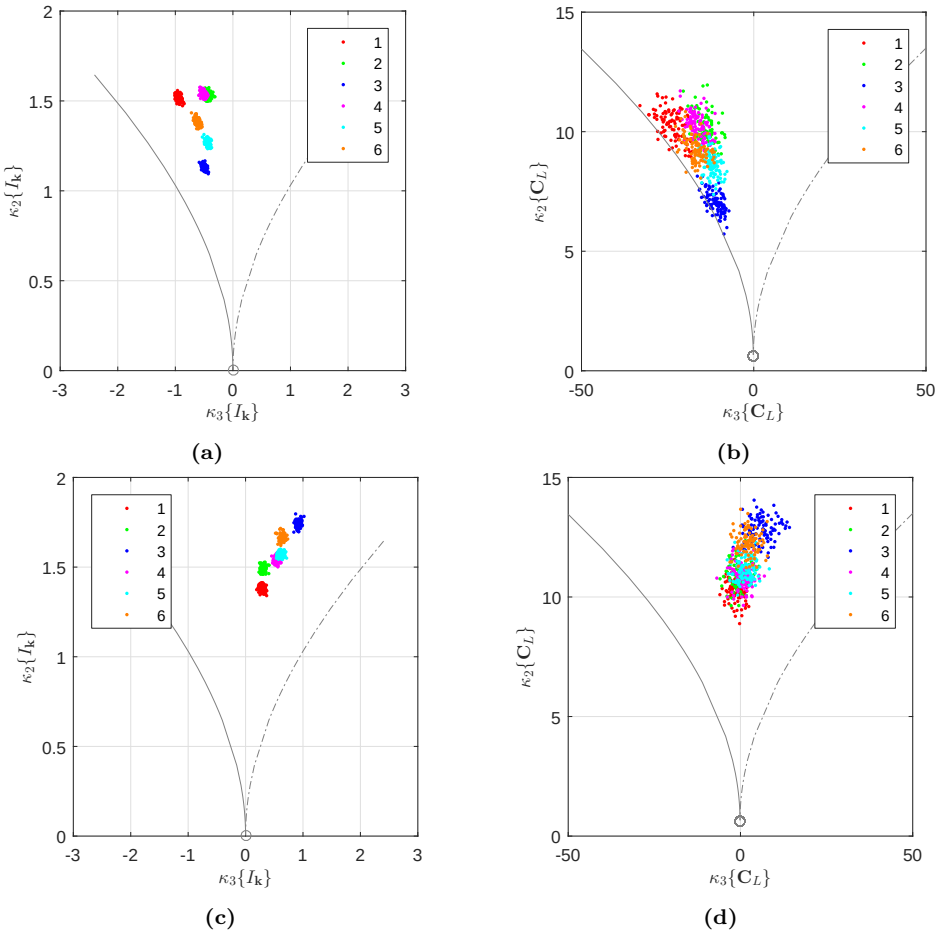

Figure 4.10: Log-cumulants of the test areas in Fig. 4.9. (a) Log-cumulants of the l_2-norms (first site). (b) Matrix variate log-cumulants (first site). (c) Log-cumulants of the l_2-norms (second site). (d) Matrix variate log-cumulants (second site).

4.4 Conclusions

Analyzing the statistical properties of PolSAR data is a difficult task due to the multi-dimensionality of the signal. A common way doing this is to study the statistics of each polarimetric channel separately. The correlation between different polarimetric channels are usually neglected, though it provides very useful information that makes the multidimensional SAR system differ from a single SAR system. In this chapter, the l_2-norm, or the Span, of the scattering vector is studied, and it is found to be a useful tool for texture analysis of PolSAR data, which takes into account both the intensities and correlations. In addition, the Span has a physical meaning, and it is polarimetrically invariant.

Two important kinds of statistics of the l_2-norm are studied. The normalized moments is an extension of the normalized intensity moments, which can be employed to evaluate

the non-Gaussian behavior of the data easily. The values of different orders could reveal the polarimetric properties of PolSAR data, as well as the texture properties. The log-cumulants can be used to identity the texture distribution of the data. No multilook processing is required to compute these values, which is an advantage in the analysis of high spatial resolution data or urban areas, since the statistical behavior may change and mixtures of targets may appear after a filtering. In addition, no ENL is required to obtain these quantities. Thus the difficult task, estimating the ENL, can be avoided.

Estimators for the normalized moments and log-cumulants are provided. The former is biased but the bias asymptotically vanishes as increasing the sample size. The latter is an unbiased estimator. The variances of the estimators are also given. One can further develop parameter estimators and design goodness-of-fit tests using these statistics.

Results on real SAR data show that texture information is of great importance. When different targets belong to a same category, saying crops or forest, the scattering mechanisms may be same, and similar polarimetric information will be observed. It is difficult to discriminate these targets by the polarimetric information only. Combining information conveyed by the texture, however, could give a better identification of targets. Crops of different types, and forests with trees of different characteristics can be further distinguished.

The statistics are derived based on the assumption that the texture for all polarimetric channels is the same. Multi-texture, where the correlations of polarimetric channels are important since the textures may be correlated, will be considered in the next step.

5

Chapter 5

Physical Interpretation of Data Models

Physically, the signal received by the SAR sensor from a resolution cell can be regarded as a sum of various complex phasors, each resulting from an individual scatterer. The addition of the independent and randomly located complex contributions gives rise to speckle. The classical model for homogeneous data assumes that the scatterer number in a resolution cell is big enough to give Gaussian distributed speckle [68]. However, the $\mathcal{K}$ distribution (Section 3.2.1.1) obtained by letting the scatterer number follow a negative binomial distribution, is demonstrated to be more accurate for the speckle in areas such as sea surface and forest [6,27,122]. As proved in [93], the $\mathcal{K}$ distribution can be formulated into a product of two independent random variables, one is gamma distributed, and the other follows a Gaussian distribution. The former is referred to as texture parameter and the latter as speckle [28,123]. Since then, a number of models have been proposed by altering the distribution of the texture parameter based on this product scheme, see Section 3.2 for more details.

However, unlike the Gaussian distribution and the $\mathcal{K}$ distribution, most of the texture models lack a physical explanation of the underlying scattering process. They give no clues about why data following a specific distribution is obtained. In this chapter, a simulator based on the random walk model [27, 68] is developed. With it, we can simulate data under certain scattering scenarios by controlling the factors that may appear in the data formation process. And then, a suitable texture model, $\mathcal{G}^0$ distribution (Section 3.2.1.2) for example, can be found for the simulated data via statistical analysis using the tools detailed in Chapter 4. The scattering process and the statistical data models, thus, are bridged, and possible physical explanations can be given to some models.

The remainder of this chapter is organized as follows. First of all, the two-dimensional random walk is introduced, which leads to the Gaussian distribution or $\mathcal{K}$ distribution by changing the distributions for the scatterer number in each resolution cell. Second, the PolSAR data simulator based on the multi-dimensional random walk is detailed. Algorithms on how to simulate different scatterer types and scatterer numbers are given, as well as mixtures of targets. At last, experimental results on both simulated data and real SAR data are shown.

5.1 Random Walk Model

Under the assumption of Born approximation or simple scattering approximation [124], the observing surface can be regarded as a collection of independent discrete scatterers. If the wavelength of the EM waves is much smaller than the dimension of a single resolution cell, it is impossible to separate the contributions from different scatterers in that cell [82]. This is related to the SAR data focus process that has been detailed in Section 2.1. As unveiled by (2.13), the received signal is a coherent sum of echoes from all the scatterers in the resolution cell. This sum of complex phasors can be described by a two-dimensional random walk as shown in Fig. 5.1b. Mathematically, it can be expressed as [68]:

$$\begin{aligned} Ae^{j\varphi} &= \sum_{i=1}^{N} a_i e^{j\varphi_i} \\ \text{Re}\left\{Ae^{j\varphi}\right\} &= \sum_{i=1}^{N} a_i \cos\varphi_i \\ \text{Im}\left\{Ae^{j\varphi}\right\} &= \sum_{i=1}^{N} a_i \sin\varphi_i \end{aligned} \tag{5.1}$$

where A is the amplitude of the signal and N refers to the number of targets within the resolution cell. The amplitude a_i and the phase φ_i of each phasor are statistically independent. This fact states that the strength of a given scattered wave bears no relation to its phase. Furthermore, the phases are uniformly distributed in the interval $(-\pi, \pi]$ by assuming the scatterers to be randomly located in the resolution cell.

With this model, it is possible to calculate a number of useful statistical properties of the resultant field. The average value of the signal can be seen immediately [125]

$$\mathrm{E}\{Ae^{j\varphi}\} = 0. \tag{5.2}$$

The correlation of two phasor echos is given by

$$\mathrm{E}\{a_i e^{j\varphi_i} a_k e^{-j\varphi_k}\} = a_i a_k \delta(i-k) \tag{5.3}$$

where $\delta(\cdot)$ is the Dirac function. From this it follows that the mean intensity of the received signal can be written as

$$\mathrm{E}\{I\} = \mathrm{E}\{a^2\} \sum_{i,k=1}^{N} \mathrm{E}\{e^{j(\varphi_i - \varphi_k)}\} = N\,\mathrm{E}\{a^2\}. \tag{5.4}$$

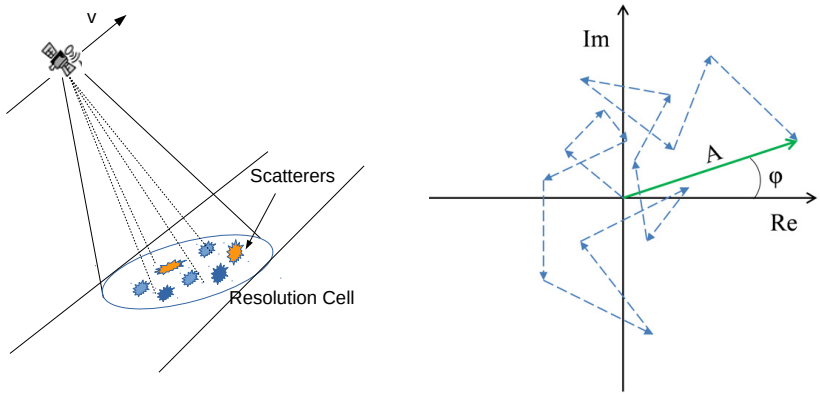

(a) **(b)**

Figure 5.1: Illustration of the received echo from a resolution cell. (a) SAR resolution cell. (b) The received data can be viewed as a two-dimensional random walk.

Here the amplitudes of all phasors are treated as observations of the same random variable a. The second moment of the intensity is

$$\begin{aligned} \mathrm{E}\{I^2\} &= \sum_{i,k,l,m=1}^{N} \mathrm{E}\{a_i a_k a_l a_m\}\, \mathrm{E}\{e^{j(\varphi_i-\varphi_k+\varphi_l-\varphi_m)}\} \\ &= 2N(N-1)\,\mathrm{E}^2\{a^2\} + N\,\mathrm{E}\{a^4\} \end{aligned} \tag{5.5}$$

due to the non-zero terms fall into two categories: the pairs $\{i = k, l = m\}$ and $\{i = m, k = l\}$ that give $2N(N-1)$ terms, and the special case $i = k = l = m$ that gives N terms [125]. The normalized moments of the second order takes the form

$$\frac{\mathrm{E}\{I^2\}}{\mathrm{E}^2\{I\}} = 2\left(1 - \frac{1}{N}\right) + \frac{1}{N}\frac{\mathrm{E}\{a^4\}}{\mathrm{E}^2\{a^2\}}. \tag{5.6}$$

When N is very large, we have the normalized intensity moment of the second order equal to 2, which is the same as an exponential distributed random variable, see Section 4.1.1 for more details.

As a matter of fact, when $N \to \infty$, equation (5.1) states that both real and imaginary parts of a distributed target have a zero-mean Gaussian distribution, as the number of scatterers inside the resolution cell is large enough to fulfill the CLT [68]. Each pixel of an image, therefore, can be described as a complex Gaussian random variable as characterized by (3.2). Its amplitude is defined by a Rayleigh distribution, and its intensity by an exponential distribution.

However, the condition that $N \to \infty$ does not hold in many circumstances:

- In high resolution SAR systems, only a few number of scatterers are present within the resolution cell, N is supposed to be small.

- In the extreme case of an isolated target inside the resolution cell, the intensity is given by the deterministic impulse response of the SAR system, this is the case of deterministic targets.
- In addition, the scatterer number is supposed to be random, since the imaging scene is usually a coarse surface with variations in height. The fluctuation of the scatterer number generally will give rise to non-Gaussian distributions.

For a certain N, the PDF of the intensity can be calculated from the random walk model, see Appendix B.1 or [125, Chapter 4], which is as follows:

$$p(I|N) = \frac{1}{2}\int_0^\infty uJ_0(u\sqrt{I})\,\mathrm{E}^N\{J_0(ua)\}du \tag{5.7}$$

where $J_0(z)$ is the Bessel function of the first kind [84], and the expectation $\mathrm{E}^N\{J_0(ua)\}$ is computed on the amplitudes of random phasors, a. Further, if N follows a negative binomial distribution

$$p(N;\alpha,p) = \binom{N+\alpha-1}{N}p^\alpha(1-p)^N \tag{5.8}$$

with a large mean value $\mu = \alpha(1-p)/p$, it can be proved (Appendix B.2) that the intensity will follow a $\mathcal{K}$ distribution [122]

$$p(I) = \frac{2\alpha}{\mu_I\Gamma(\alpha)}\left(\frac{\alpha I}{\mu_I}\right)^{\frac{\alpha-1}{2}}K_{\alpha-1}\left(2\sqrt{\frac{\alpha I}{\mu_I}}\right) \tag{5.9}$$

where $\mu_I = \mathrm{E}\{A^2\}$. The negative binomial distribution is a solution of the stable state of the birth-death-migration process [6, 27], which resembles the process of the scatterers going into and out a resolution cell.

5.2 PolSAR Data Simulator

5.2.1 PolSAR Data Model

Considering only the simple scattering again [124], if there are N individual scatterers randomly distributed inside a resolution cell, the received polarimetric SAR data can be written as the sum of their responses

$$\mathbf{k} = \frac{1}{\sqrt{N}}\sum_{i=1}^{N}\mathbf{s}_i \tag{5.10}$$

where $\mathbf{s}_i$ denotes the response from a single scatterer. The normalizing factor $1/\sqrt{N}$ is introduced to assure that the average intensity of the speckle is independent of N. When the pixels are correlated, N is the equivalent number of scatterers per resolution cell, which could be non-integers. But in this chapter only the uncorrelated cased is considered, where N is a positive integer. The dimension of $\mathbf{k}$ is taken to be 4, corresponding to the

polarimetric channels S_{hh}, S_{hv}, S_{vh} and S_{vv} respectively, where h denotes the horizontal polarization basis and v the vertical one. For the backscattering from a reciprocal medium (Section 2.2.2), the cross polarization channels are equal ($S_{hv} = S_{vh}$), and then the dimension is reduced to 3, which is the case mainly discussed here. The covariance matrix is given by

$$\mathbf{\Sigma} = E\{\mathbf{k}\mathbf{k}^{\dagger}\} = E\{\mathbf{s}\mathbf{s}^{\dagger}\}. \tag{5.11}$$

There are several factors having contribution to the statistics of the vector $\mathbf{k}$. The first one is the scatterer type that characterizes the response of each scatterer [126]. Let a denote the amplitude and ϕ the phase, a scatterer can be represented by

$$\mathbf{s} = \left[a_{hh}e^{j\phi_{hh}}, a_{hv}e^{j\phi_{hv}}, a_{vv}e^{j\phi_{vv}}\right]^T. \tag{5.12}$$

For each polarimetric channel, the amplitudes and the phases are statistically independent. Furthermore, the phases are assumed to be uniformly distributed over $(-\pi, \pi]$. This assumption arises from the fact that the differences of paths from scatterers in one resolution cell to the antenna are much greater than the wavelength, so that any value of phase is equally probable [28]. Different scatterer types can be distinguished by the distributions of their amplitudes. The variances of the amplitudes could reflect the roughness of the observing surface, large values meaning rough surface, whereas small values meaning smooth surface. In addition, the scatterer type can show the proportions of the weak scatterers and strong scatterers by means of skewness. The polarimetric information conveyed by the scatterers is determined by the covariance matrix $\mathbf{\Sigma}$.

The second factor is the scatterer number N. On one hand, a lot of research has shown that the fluctuation of scatterer numbers will give arise to texture [6, 27], which carries information that may enable a user to identify different cover types. On the other hand, for the high resolution data, where the scatterer number is finite and small, it is known that the classical models such as Gaussian distribution usually fail to give an accurate representation [127]. Therefore, the scatterer number could reveal the changing of the surface properties such as the height, as well as the features of the radar system.

At last, the heterogeneity appeared in PolSAR data can be resulted from the mixture of different targets. For instance, from an urban area which usually consists of discrete objects like houses, trees and roads, the backscattering is a combination of different scattering mechanisms. To represent this type of data, a simple model would be inappropriate [22]. Mixture models as introduced in Section 3.3, instead, could achieve reasonable level of accuracy [22, 23, 128].

To summarize, the random walk model is linked to the underlying scattering process, and (5.10) provides a physical insight into the scattering problem, as physical explanations can be given to the mentioned factors of the random walk model. Taking into account all the above aspects, a simulator that helps to study the statistics of PolSAR data is designed. Details of the implementation are given in the following sections, provided that the algorithms to sample the univariate uniform, Gaussian, gamma and beta distributions exist.

5.2.2 Scatterer Type

In this section, different distributions are introduced to describe the scatterers, with the purpose of exploiting different variations, which can be related to the physical properties of the observing surface. As detailed in Section 2.2.2, the scatterers can be classified into point (or coherent) ones and distributed ones depending on whether only one scattering matrix is enough to characterize the target or not. The Gaussian scatterer, K-scatterer, Constant scatterer and Beta scatterer shown as follows belong to the distributed targets.

5.2.2.1 Point Scatterer

Man-made targets can be treated as point like scatterers. It is important to simulate this type of targets when modeling urban areas. The response from a point scatterer to the incident wave should be deterministic. Consider several point scatterers of the same kind, however, the scattered waves are random due to their different positions. Let ϕ denote the phase difference due to the position and $\mathbf{s}'$ the scattering vector regardless of the position, the simulation of a point scatterer can be described as Algorithm 5.1. The phase difference is uniformly distributed over $[0, 2\pi)$ by assuming that the scatterers are randomly located.

Algorithm 5.1 Simulation of a Point Scatterer

1: **procedure** PointScatterer($\mathbf{s}'$)
2: $\quad\phi \sim U(0, 2\pi)$ ▷ U, uniform distribution
3: $\quad\mathbf{s} \leftarrow \mathbf{s}' \cdot e^{j\phi}$
4: $\quad$**return s**
5: **end procedure**

5.2.2.2 Gaussian Scatterer

A Gaussian scatterer can be represented by a vector that follows a multivariate complex Gaussian distribution with zero mean, as expressed by (3.1). For each polarimetric channel, the amplitude is Rayleigh distributed. Gaussian distributions are widely used to analyze random variables whose distributions are not known. Many complex problems can be derived analytically in explicit form when the relevant variables are assumed to follow Gaussian distributions, due to their mathematical tractability. Therefore, it is interesting to test Gaussian distributions as the distributions of scatterer responses. The procedure of simulating a Gaussian scatterer is shown in Algorithm 5.2.

5.2.2.3 K-Scatterer

A K-scatterer is defined by the multivariate $\mathcal{K}$ distribution given by (3.37). The $\mathcal{K}$ distribution has a wide range of shapes, which makes it well suited to describe scenes where there are scatterers with a variety of geometries and orientations [74]. As already mentioned, the $\mathcal{K}$ distributed random variable can be viewed as the product of two random variables, one follows a Gaussian distribution and the other a gamma distribution.

Algorithm 5.2 Simulation of a Gaussian Scatterer

procedure GaussianScatterer($\mathbf{\Sigma}$)
  $\mathbf{L} \leftarrow$ Cholesky decomposition on $\mathbf{\Sigma}$
  $R_{hh}, I_{hh}, R_{hv}, I_{hv}, R_{vv}, I_{vv} \sim N(0, 1/2)$ ▷ N, Normal distribution
  $\mathbf{u} \leftarrow [R_{hh} + jI_{hh}, R_{hv} + jI_{hv}, R_{vv} + jI_{vv}]^T$
  $\mathbf{s} \leftarrow \mathbf{Lu}$
  return s
end procedure

Therefore, to simulate a K-scatterer, we can first simulate a Gaussian scatterer, and then multiply it by a gamma distributed random variable τ characterized by (3.36), see Algorithm 5.3.

Algorithm 5.3 Simulation of a K-Scatterer

procedure KScatterer($\mathbf{\Sigma}$, α)
  $\mathbf{z} \leftarrow$ GaussianScatterer($\mathbf{\Sigma}$)
  $\tau \sim \Gamma(\alpha, 1/\alpha)$ ▷ Γ, Gamma distribution
  $\mathbf{s} \leftarrow \tau \cdot \mathbf{z}$
  return s
end procedure

5.2.2.4 Constant Scatterer

For each polarimetric channel, the response of a Constant scatterer to the incident wave has a nonrandom amplitude [126]. In reality it is difficult to find any Constant scatterers, but as a contrast to the variable amplitudes, the study of constant ones is instructive. The Constant scatterer is equivalent to the equal length component in the random walk model [129].

Consider the simplest case first, where the amplitudes of all polarimetric channels are equal to 1

$$\mathbf{u} = \left[e^{j\phi_{hh}}, e^{j\phi_{hv}}, e^{j\phi_{vv}}\right]^T \tag{5.13}$$

The covariance matrix is given by $\mathbf{R} = \mathrm{E}\{\mathbf{u}\mathbf{u}^\dagger\}$, which is also the correlation matrix. If all diagonal elements of the covariance matrix are equal to 1, like the $\mathbf{R}$, the corresponding scatterer is referred to as a normalized scatterer. To the best of our knowledge, there is neither closed form expression for the PDF, nor well known simulation algorithm of the random vector $\mathbf{u}$ for a given covariance matrix. A simulation procedure based on numerical analysis is designed.

Given a set of normalized Gaussian scatterers with covariance matrix $\mathbf{R}_g$, if we let all the amplitudes be 1, they are transformed into a set of normalized Constant scatterers with a different covariance matrix $\mathbf{R}$. From tests with different correlations, see Fig. 5.2a, it is found that for the matrix entries, $\mathbf{R}_g(i,k) = \rho_g e^{j\phi_g}$ and $\mathbf{R}(i,k) = \rho e^{j\phi}$,

the relationship is given approximately by

$$\begin{cases} \rho_g = 0.3701\rho^5 - 1.1215\rho^4 + 0.9406\rho^3 - 0.5643\rho^2 + 1.3875\rho - 0.0078 \\ \phi_g = \phi \end{cases} \tag{5.14}$$

This means a normalized Constant scatterer can be obtained by setting the amplitudes of a normalized Gaussian scatterer to 1, and the covariance matrix used to simulate the latter is calculated according to (5.14).

To simulate a scatterer for any covariance matrix $\mathbf{\Sigma}$, we first simulate a normalized Constant scatterer $\mathbf{u}$ with covariance matrix given by $\mathbf{R}$ with entries

$$\mathbf{R}(i,k) = \frac{\mathbf{\Sigma}(i,k)}{\sqrt{\mathbf{\Sigma}(i,i)\mathbf{\Sigma}(k,k)}} \tag{5.15}$$

where i and k are the row number and column number. Then multiply a factor for each polarimetric channel, $\mathbf{s} = (\text{diag}(\mathbf{\Sigma}))^{-1/2}\mathbf{u}$, where $\text{diag}(\mathbf{\Sigma})$ is a diagonal matrix with diagonal elements equal to those of $\mathbf{\Sigma}$. The total simulation process is described in Algorithm 5.4.

Algorithm 5.4 Simulation of a Constant Scatterer

```
procedure ConstantScatterer(Σ)
    R ← Calculate (5.15)
    R_g ← Calculate (5.14)
    z ← GaussianScatterer(R_g)
    u ← Set amplitudes of z to 1
    s ← (diag(Σ))^{-1/2} u
    return s
end procedure
```

5.2.2.5 Beta Scatterer

The amplitudes of the responses from Beta scatterers are assumed to follow a beta distribution. A useful property of the beta distribution is that it has nonzero value over only a finite interval, and therefore does not allow amplitudes larger than a certain maximum [126]. For $0 \leq a \leq 1$, and shape parameters $\alpha, \beta > 0$, the PDF of the beta distribution is given by (3.54). It has been shown that the statistic of the speckle will follow a beta distribution if introducing a constraint to the total wave intensity received by the sensor [130]. This is also known as the saturation effect. But here the introduction of the Beta scatterer is mainly because it allows exploration of the effects of various shapes of possible distributions, rather than a particular scattering problem.

A multivariate generalization of the beta distribution, known as the Dirichlet distribution, has a limited dependence structure, where the correlation coefficients are negative [131]. It is not suitable to model the amplitudes of different polarimetric channels. In order to model a more general correlation, the numerical method based on copulas theorem is employed, where correlated beta random variables are produced by transforming correlated normal random variables [132].

Similar as the Constant scatterers, Beta scatterers are obtained by replacing the amplitudes of Gaussian scatterers with correlated beta random variables. Through the Monte Carlo simulations, it is found that the inter-channel correlation of the normalized Beta scatterer ($\rho e^{j\phi}$) is a function of that of the normalized Gaussian scatterer ($\rho_g e^{j\phi_g}$) and the correlation of beta distributed amplitudes (ρ_b), see Fig. 5.2b. The relationship can be approximated by

$$\begin{cases} \rho = 0.6721\rho_b + 0.0050\rho_g - 0.2884\rho_b^2 + 0.145\rho_b\rho_g + 0.3563\rho_b^3 + 0.0756\rho_b^2\rho_g \\ \phi = \phi_g \end{cases} \tag{5.16}$$

By letting ρ_g be 1, the phases of Beta scatterers are obtained from Gaussian scatterers, and amplitudes from correlated beta distributions. The simulation procedure is described as Algorithm 5.5.

Algorithm 5.5 Simulation of a Beta Scatterer

procedure BetaScatterer($\mathbf{\Sigma}$, α, β)
  $\mathbf{R} \leftarrow$ Calculate (5.15)
  $\phi_g \leftarrow$ Calculate (5.16)
  $\mathbf{R}_g(i,k) \leftarrow 1 \times e^{j\phi_g}$
  $\mathbf{z} \leftarrow$ GaussianScatterer($\mathbf{R}_g$)
  $\rho_b \leftarrow$ Calculate (5.16), letting $\rho_g = 1$
  $\mathbf{a} \sim B(\alpha, \beta, \rho_b)$ ▷ B, Beta distribution
  $\mathbf{u} \leftarrow$ Set amplitudes of $\mathbf{z}$ as $\mathbf{a}$
  $\mathbf{s} \leftarrow (\text{diag}(\mathbf{\Sigma}))^{-1/2}\mathbf{u}$
  Return $\mathbf{s}$
end procedure

5.2.3 Scatterer Number

As the PolSAR sensor moves along the azimuth direction, the scatterers going in and out of the resolution cells can be modeled by a stochastic process. The number of scatterers, as a result, varies from one resolution cell to another. In addition, the changing of the surface height could also give rise to the variation of scatterer number. The fluctuation of the scatterer number plays an important role in characterizing the statistics of the scattering vector. Normally, the equivalent number of scatterers in different resolution cells could be any positive values due to the spatial correlation, but here only integers are considered regardless of the correlation, including the following cases.

5.2.3.1 Constant

For middle or low resolution data, it is reasonable to assume that there is a large number of scatterers inside each resolution cell, and in different resolution cells, the number keeps the same. At this point, the CLT can be brought to bear. No matter what distribution the scatterers follow, the resulting scattering vector will be asymptotically Gaussian distributed [68]. In contrast, the area covered by a resolution cell becomes smaller in

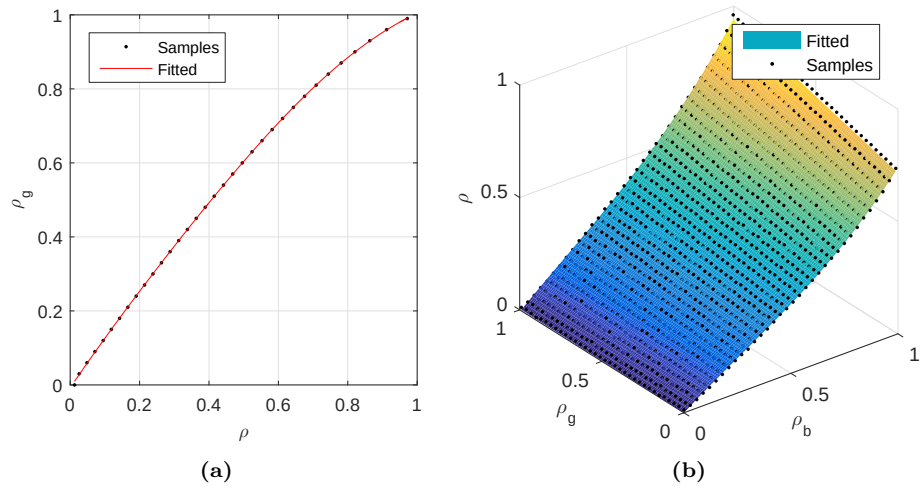

Figure 5.2: The relationship between the correlation coefficient of the amplitudes and that of Gaussian scatterers is approximated using Monte Carlo simulations. (a) Correlation relationship between the Constant scatterer (ρ) and the Gaussian scatterer (ρ_g). (b) Correlation relationship between the Beta scatterer (ρ) and the Gaussian scatterer (ρ_g), as well as correlated beta distribution (ρ_b).

the high resolution data, and the CLT doesn't hold any more. The distribution of the received data will be affected by the scatterer type [126]. To meet all these situations, any positive integer is allowed as the scatterer number.

5.2.3.2 Negative Binomial

In many cases of practical interest, the number of scatterers N is a random variable [27]. The distribution of the resulting field then is non-Gaussian. For example, if N follows a negative binomial distribution (5.8), the scattering vector will follow a multivariate $\mathcal{K}$ distribution [6]. The variation of the scatterer number is due to the changing of the radar cross section, which is related to the geometry properties (height for example) of the observing surface. It is supposed that the changing of the surface is not very fast. The scatterer number is fluctuating at a larger scale than the scale of a resolution cell.

5.2.3.3 Compound Distribution

In [133], the number of scatterers is modeled by a Poisson distribution [86] with the mean value λ also randomly distributed according to some other distribution $f(\lambda;\boldsymbol{\alpha})$. Integrating the intermediate parameter λ out, the distribution of the scatterer number is then given by

$$p(N;\boldsymbol{\alpha}) = \int_0^\infty \frac{\lambda^N e^{-\lambda}}{N!} f(\lambda;\boldsymbol{\alpha}) d\lambda. \tag{5.17}$$

There are several distributions from the Pearson's system suggested for f, including gamma distribution, inverse gamma distribution, beta distribution, and beta prime dis-

Table 5.1: Compounding Distributions

Distribution	PDF
Gamma	$f(\lambda;\alpha,\beta)=\frac{1}{\Gamma(\alpha)\beta^{\alpha}}\lambda^{\alpha-1}\exp(-\lambda/\beta)$
Inverse Gamma	$f(\lambda;\alpha,\beta)=\frac{\beta^{\alpha}}{\Gamma(\alpha)}\lambda^{-\alpha-1}\exp(-\beta/\lambda)$
Beta	$f(\lambda;\alpha,\beta)=\frac{\Gamma(\alpha+\beta)}{\Gamma(\alpha)\Gamma(\beta)}\lambda^{\alpha-1}(1-\lambda)^{\beta-1},\ \lambda\in[0,1]$
Beta Prime	$f(\lambda;\alpha,\beta)=\frac{\Gamma(\alpha+\beta)}{\Gamma(\alpha)\Gamma(\beta)}\lambda^{\alpha-1}(1+\lambda)^{-\alpha-\beta}$

tribution [133], see Table 5.1. They provide a wide variety of the scatterer number fluctuations. In particular, when λ is gamma distributed, the resulting distribution is equivalent to negative binomial distribution. Algorithm 5.6 shows the simulation process of a scatterer number that follows compound distributions. Notice that if $Y = 1/X$ where X is gamma distributed, then Y follows an inverse gamma distribution. And Y follows a beta prime distribution, if $Y = \frac{X}{1-X}$ and X is beta distributed. Therefore, it's possible to draw samples from inverse gamma distributions and beta prime distributions by transforming samples from gamma distributions.

Algorithm 5.6 Simulation of Compound Scatterer Number

1: **procedure** CompoundNum($\boldsymbol{\alpha}$)
2: Get a sample λ from $f(\lambda;\boldsymbol{\alpha})$.
3: Get a sample from Poisson distribution, $N \sim Po(\lambda)$.
4: **end procedure**

5.2.4 Mixture of Scatterers

Generally, the scatterers in (5.10) are assumed to belong to the same category, one of the Gaussian scatterer, K-scatterer, Constant scatterer or Beta scatterer. But there are many cases where more than one scatterer type appears in the same resolution cell. In addition, a region under analysis can be divided into several subregions on many occasions, each with a different scatterer type. These will be regarded as mixtures of scatterers at the pixel level (in the same resolution cell), or at the spatial level (in different resolution cells).

5.2.4.1 Mixture at Pixel Level

The mixture at pixel level assumes that each resolution cell contains scatterers from more than one type. Take urban areas for example, the backscattering can be viewed as the combination of echos from distributed targets (trees and grass), and point targets (buildings). Or according to scattering mechanisms, the scatterers inside a resolution cell can be classified into volume scattering, double-bounce scattering, surface scattering and

so on. In this case, the random walk model can be written as

$$\mathbf{k} = \sqrt{\frac{1}{N_1 + N_2 + \cdots}} \left(\sum_{i=1}^{N_1} \mathbf{s}_i^{(a)} + \sum_{i=1}^{N_2} \mathbf{s}_i^{(b)} + \cdots \right) \tag{5.18}$$

where $N = N_1 + N_2 + \cdots$ is the total number of scatterers.

5.2.4.2 Mixture at Spatial Level

In PolSAR data, the bright clutters and dark ones usually appear alternatively in the forest areas, corresponding to strong returns from the crowns of trees with shadows behind them. The similar phenomenon also appears in the sea surface when there exist wave crests and troughs. The received data can be treated as the mixture of two types of scatterers located alternatively. Assume that the region of interest can be modeled by a mixture of K components, then the overall PDF of the scattering vector can be written as (3.83). It has been shown that for complicated regions with more irregular histograms (multimodal, spiky), the mixture model is more accurate than a single distribution [22,23]. The mixture of pixel level and spatial level are illustrated by Fig. 5.3.

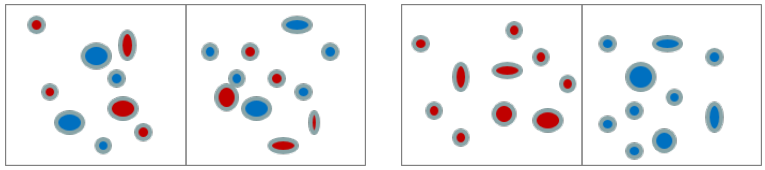

(a) **(b)**

Figure 5.3: Different types of mixtures. Rectangles represent resolution cells, whereas ellipses represent scatterers. Different colors mean different scatterer types. (a) Mixture at pixel level. (b) Mixture at spatial level.

5.3 Simulated SAR Data

5.3.1 High Resolution Data

In high resolution data, where the resolution cell is only a few wavelength wide, the usual hypothesis underlying the speckle phenomena, i.e., a large number of scatterers per resolution cell, may be not true [126]. The distribution of the data may depend on the distribution characterizing the individual scatterers. To validate this hypothesis, simulated data with different scatterer numbers and scatterer types are implemented, using the algorithms detailed in the previous section.

In each simulation, all the resolution cells have the same number of scatterers. Integer values from 1 to 10 are tested. Different scatterer types including Gaussian scatterer (`GS`), K-scatterer (`KS`), Constant scatterer (`CS`), as well as Beta scatterer (`BS`) are simulated,

Table 5.2: Parameters for Simulating High Resolution Data

Case	Covariance Matrix	Additional Parameters
`GS`	(5.19)	None
`KS1`	(5.19)	$\alpha = 3$
`KS2`	(5.19)	$\alpha = 6$
`CS`	(5.19)	None
`BS1`	(5.19)	$\alpha = 2, \beta = 2$
`BS2`	(5.19)	$\alpha = 2, \beta = 5$

with the same covariance matrix

$$\mathbf{C}_1 = \begin{bmatrix} 1 & \sqrt{3} \times 0.3e^{-j\frac{\pi}{2}} & \sqrt{2} \times 0.7e^{j\frac{\pi}{5}} \\ \sqrt{3} \times 0.3e^{j\frac{\pi}{2}} & 3 & \sqrt{6} \times 0.2e^{j\frac{\pi}{4}} \\ \sqrt{2} \times 0.7e^{-j\frac{\pi}{5}} & \sqrt{6} \times 0.2e^{-j\frac{\pi}{4}} & 2 \end{bmatrix} \tag{5.19}$$

The matrix is chosen for academic study only, with consideration of different values for the intensities, as well as different correlation coefficients between polarimetric channels. Simulation parameters are summarized in Table 5.2. For the K-scatterer, two values are chosen to test different variances, `KS1` with a large variance and `KS2` with a relatively small variance, the former represents a rougher surface than the latter. Two kinds of Beta scatterers, `BS1` with skewness equal to zero and `BS2` with a positive skewness, are simulated. The skewness indicates the relation between the number of strong scatterers and that of weak scatterers. In the first case, the number of strong scatterers and the number of weak scatterers are comparable, whereas there are more weak scatterers in the second case. For each testing case, a 300×300 pixel single look complex image is generated.

The first row of Fig. 5.4 shows the Pauli decomposition (Section 2.2.2) of the simulated data where the scatterer numbers are 1, 2 and 10, respectively. We can see that all simulated images are homogeneous, but there are rather different colors in the Pauli decompositions, especially for the Constant scatterers. The empirical PDF of the amplitudes are compared with the Rayleigh distributions. The results show that not all homogeneous data have Gaussian statistics. The statistic information plays an important role in defining the homogeneous data, besides the covariance matrix. As a consequence, covariance matrix is not enough to accomplish the analysis in some cases of homogeneous data, and higher order moments are necessary.

To quantitatively evaluate the fit of Rayleigh distribution to the simulated data, the KS distance (l), defined by (4.63), and the correlation coefficient (ρ) are employed [10,22]. The values are shown in Table 5.3. As it can be seen, the statistical distribution of the sum of N Gaussian scatterers is independent of the value of N. This is because the addition of Gaussian scatterers on an amplitude basis does not change the statistics. The results calculated from Gaussian scatterers provide a reference for the comparison. The largest KS distance, 0.0034, is choosen as the limit to determine whether the data can be modeled

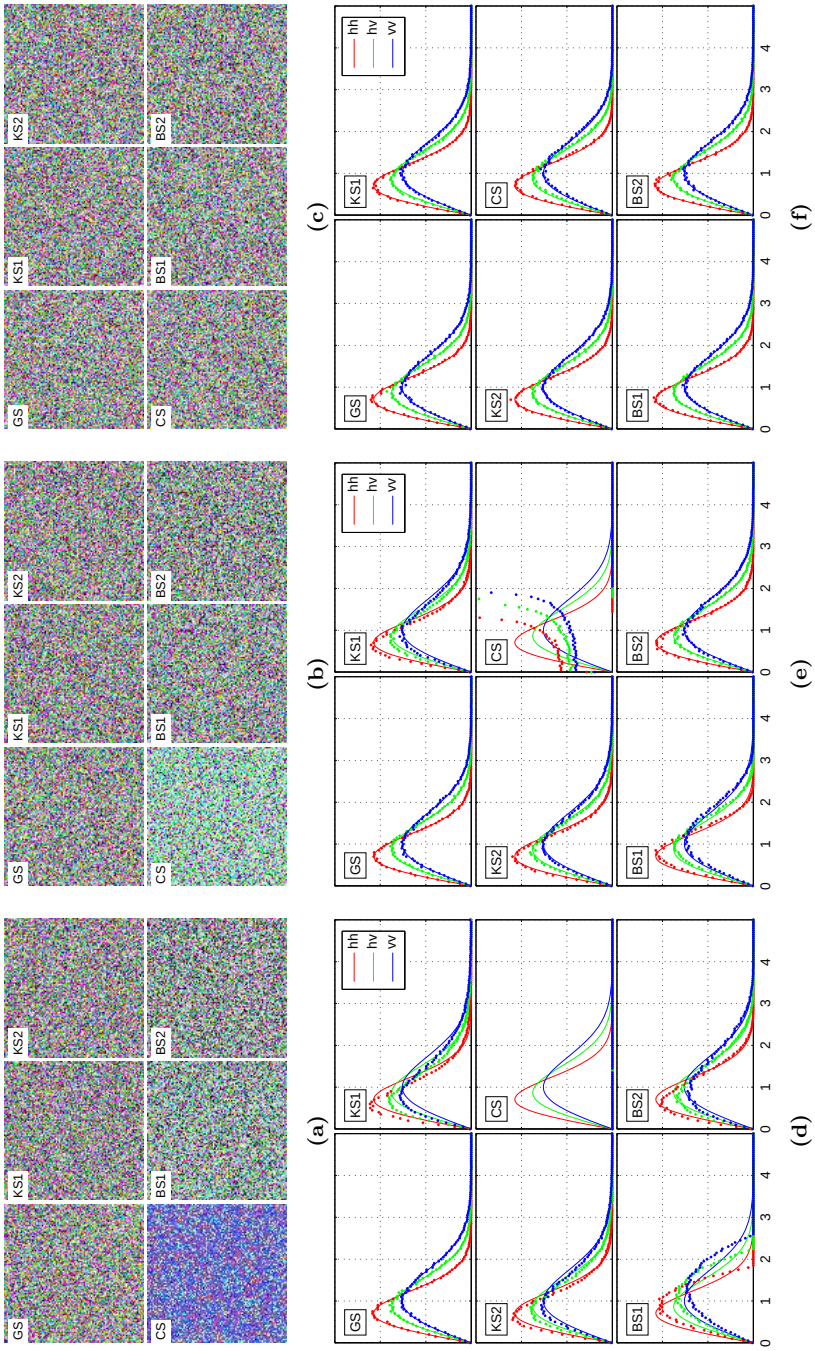

Figure 5.4: Pauli decomposition and PDFs of simulated high resolution data. The first row shows the Pauli decomposition and the second row shows the comparison between the histograms of the simulated data and Rayleigh distribution. From left to right, the scatterer number of each resolution cell is 1, 2, and 10. Testing scatter types include Gaussian scatterer (GS), K-scatterer (KS1 and KS2), Constant scatterer (CS) and Beta scatterer (BS1 and BS2).

Table 5.3: Correlation coefficients and KS distances on Simulated Data

Test	Number	GS	KS1	KS2	CS	BS1	BS2
l	1	0.0019	0.0713	0.0376	0.6088	0.0651	0.0348
	2	**0.0034**	0.0364	0.0179	0.1352	0.0264	0.0095
	3	0.0025	0.0262	0.0122	0.0580	0.0158	0.0046
	4	0.0022	0.0199	0.0114	0.0438	0.0129	0.0053
	5	0.0029	0.0164	0.0077	0.0250	0.0097	0.0037
	6	0.0031	0.0138	0.0068	0.0190	0.0080	0.0045
	7	0.0023	0.0118	0.0072	0.0184	0.0076	0.0042
	8	0.0027	0.0100	0.0069	0.0170	0.0057	**0.0032**
	9	0.0024	0.0095	0.0054	0.0138	0.0064	0.0034
	10	0.0034	0.0091	0.0052	0.0132	0.0054	0.0031
	50	0.0020	**0.0032**	**0.0034**	**0.0026**	**0.0032**	0.0031
	1000	0.0020	0.0030	0.0022	0.0025	0.0021	0.0028
ρ	1	99.96%	97.56%	99.29%	16.65%	96.79%	99.21%
	2	99.95%	99.31%	99.82%	61.81%	99.58%	99.92%
	3	99.96%	99.65%	99.90%	93.52%	99.83%	99.96%
	4	99.96%	99.78%	99.91%	98.44%	99.87%	99.95%
	5	99.96%	99.85%	99.94%	99.57%	99.93%	99.96%
	6	99.96%	99.88%	99.94%	99.73%	99.94%	99.95%
	7	99.96%	99.91%	99.95%	99.80%	99.95%	99.95%
	8	99.96%	99.93%	99.94%	99.82%	99.95%	99.96%
	9	**99.97%**	99.92%	99.95%	99.88%	99.94%	**99.97%**
	10	99.95%	99.94%	99.96%	99.88%	99.96%	99.96%
	50	99.97%	**99.97%**	**99.97%**	**99.97%**	**99.97%**	99.96%
	1000	99.96%	99.97%	99.97%	99.97%	99.96%	99.97%

by a Gaussian distribution or not. It can be seen that the value of N from where Rayleigh distribution can be concerned depends on the scatterer type. For the KS1, KS2, CS and BS1, when the scatterer number is equal or larger than 50, the resulted distributions can be well approximated by Rayleigh distributions. The correlation coefficients between the estimated and empirical distributions are higher than 99.97% and the KS distances are less than 0.035, but for the BS2, this value is 9. It has been shown that modern spaceborne SAR (e.g., TerraSAR-X) can record data with equivalent number of scatterers less than 10 based on the classical surface model [134]. In this case, the scatterer type should be concerned to understand the distribution of data.

Multilook PolSAR data are usually represented by sample covariance matrices, to which analyzing statistics such as matrix variate log-cumulants (Section 4.1.3) can be applied. As has been demonstrated in Chapter 4, special attention should be paid when performing the multilook processing on the high resolution data, as this procedure is

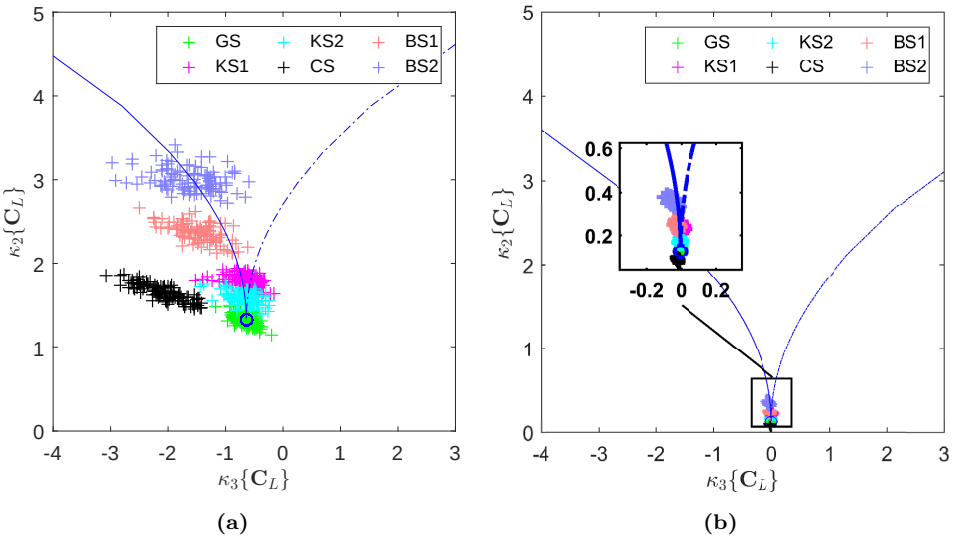

Figure 5.5: Matrix variate log-cumulants of the simulated high resolution data. (a) Multilook processing using a 2×2 window. (b) Multilook processing using a 5×5 window.

equivalent to increasing the number of scatterers in the resolution cells. In Fig. 5.5, we show the matrix variate log-cumulants of the sample covariance matrices which are obtained after applying the multilook processing with 2×2 and 5×5 sliding windows on the simulated data when $N = 1$. It shows that after applying the multilook process with a large window size, e.g. 5×5, the resulted sample covariance matrices can be approximated by a Wishart distribution, even if there are only one K-scatterer or Constant scatterer in each resolution cell. The statistics of the simulated PolSAR data approaches to Gaussian statistics more rapidly after the multilook procedure. Therefore, for high resolution data, preference should be given to the scattering vectors over the covariance matrices when coming to statistical analysis.

In addition, it is interesting to note that the sample covariance matrices of `BS2` after the multilook processing can be modeled by a $\mathcal{K}$ distribution. Accordingly, the $\mathcal{K}$ statistics of the sample covariance matrices may not come from texture at all, it is just a side effect of the multilook processing. The log-cumulants of the l_2-norms (Chapter 4) are also computed from the simulated data, see Fig. 5.6. It shows the log-cumulants from `BS2` is far away from the curve representing the $\mathcal{K}$ distributions.

5.3.2 Scatterer Number Fluctuation

In the middle or low spatial resolution data, a data cell covers a large area, and the number of scatterers inside it is considered to be large. Due to the variations of the properties of the targets and the roughness of the observing surface, the scatterer number will fluctuate from cell to cell. This situation will give rise to texture, bunching clutters in the data [93]. In the following, simulations of different distributions for the scatterer number are shown, including negative binomial distribution and compound Poisson distributions.

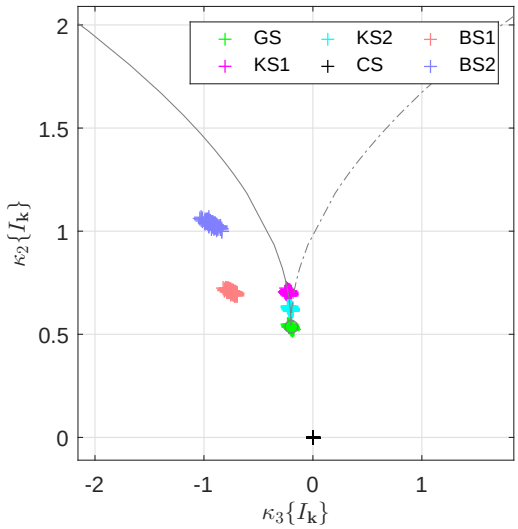

Figure 5.6: Log-cumulants of the l_2-norms on simulated high resolution data. The case that each resolution cell contains only one scatterer is simulated, this can be validated by the result of the Constant scatter (black + mark), where the value is non-random.

Table 5.4: Parameters for Simulating Textured Data

Case	Covariance Matrix	Additional Parameters
`NB1`	(5.19)	$\alpha = 5, p = 0.001$
`NB2`	(5.19)	$\alpha = 6, p = 0.001$
`C`	(5.19)	None
`IG`	(5.19)	$\alpha = 5, \beta = 0.001$
`B`	(5.19)	$\alpha = 5, \beta = 1000$
`BP`	(5.19)	$\alpha = 5, \beta = 1000$

Again, in each case, a 300×300 pixel single look image is generated to ensure there are enough samples. For the negative binomial distribution, two cases are tested, denoted as `NB1` and `NB2`, respectively. Inverse gamma, beta and beta prime distributions are examined as the compounding distribution in (5.17). To make results comparative, a same shape parameter is tested for each of them, denoted as `IG`, `B`, and `BP`, respectively. All the parameters are listed in Table 5.4. The average value of scatterer numbers is larger than 1000 by choosing a proper scale parameter β. The sample covariance matrices are obtained by applying a multilook process with 3×3 sliding windows. In the simulations, the randomness of scatterer numbers is assured to have a lower frequency than that of scatterers by letting the scatterer numbers of pixels inside a neighboring window be the same. Since we know the correlation length of the texture exactly, matrix variate log-cumulants are enough to analyze the data. They are the true statistics of the simulated

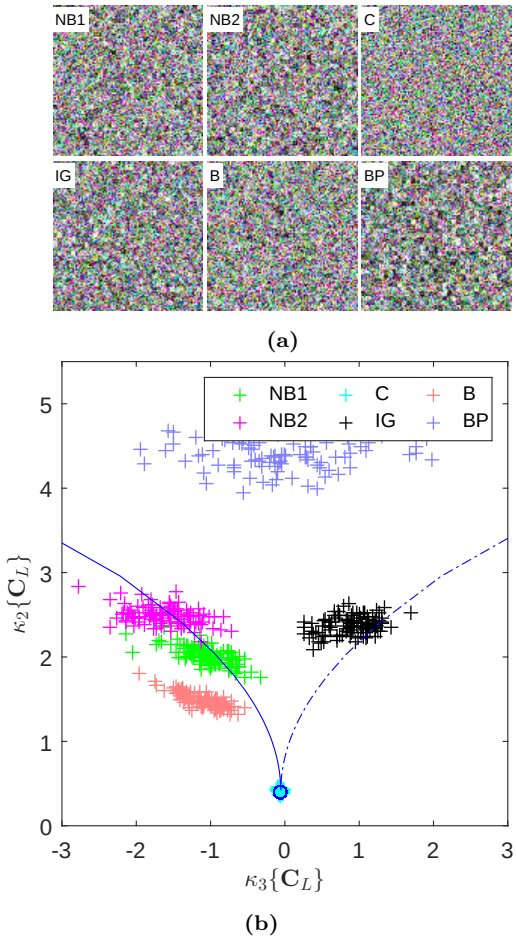

Figure 5.7: Simulated data and the matrix variate log-cumulants by employing different distributions for the scatterer number, including negative binomial distribution (`NB1` and `NB2`), compounding Poison distribution with inverse gamma (`IG`), beta (`B`) and beta prime (`BP`) distribution, as well as constant value (`C`). (a) Pauli decomposition of the data. (b) Log-cumulants of simulated data.

data if a window size less than the correlation length is chosen during the multilook processing.

Only the results of Gaussian scatterers are shown here, since the scatterer type has little influence on the final result when the scatterer number is large. From Fig. 5.7, it can be seen that $\mathcal{K}$, $\mathcal{G}^0$ and Kummer-$\mathcal{U}$ distributed data are obtained by varying the distributions of the scatterer number. In the results of Pauli decomposition, there are bunching of scatterers, which is known as texture. Altering the shape parameters of the distributions for the scatterer number, data with different texture parameters are obtained, see `NB1` and `NB2` for example.

5.3.3 Mixture

Mixtures of ground cover types within a resolution cell or a region are common in PolSAR images since the observing scene usually covers a large area. To see the influence on the statistical properties of PolSAR data, mixtures at pixel and spatial levels are simulated.

First, the simulation of mixing two Gaussian scatterers of different classes is implemented, one is given by the covariance matrix (5.19), and the other by (5.20). As we can see, the two covariance matrices have different elements. They are chosen only for academic study and no particular scattering mechanisms are considered. The polarimetric information they convey are different.

$$\mathbf{C}_2 = \begin{bmatrix} 1 & 0.5e^{j\pi/3} & 0.4e^{-j\pi/4} \\ 0.5e^{-j\pi/3} & 1 & 0.5e^{j\pi/6} \\ 0.4e^{j\pi/4} & 0.5e^{-j\pi/6} & 1 \end{bmatrix} \tag{5.20}$$

For the scatterer number, the negative binomial distributed random variables (`NB`), Poisson distribution compounding with inverse gamma distribution (`IG`), as well as constant values (`C`) are tested. Mixtures at both pixel level (`P`) and spatial level (`S`) are applied, where each class takes up 50% proportion. The simulated data and the matrix variate log-cumulants calculated from them are shown in Fig. 5.8. It is noticed that the mixture at spatial level gives heterogeneous data that follows Kummer-$\mathcal{U}$ distributions. The mixture of distributed scatterers at pixel level changes the covariance matrix, but the texture of the obtained data is determined by the fluctuations of the scatterer numbers, for instance, negative binomial distributed scatterer numbers give a $\mathcal{K}$ distribution.

Fig. 5.9 shows the matrix variate log-cumulants of the simulated data which are obtained by changing the mixing proportion of the first class, given by covariance matrix (5.19), from 0 to 100%. It is observed that changing the proportions leads the log-cumulants of the simulated data to cover all the $\kappa 2$-$\kappa 3$ space. This is also validated by Nicolas on single channel data [25]. From Fig. 5.7 and Fig. 5.9, we notice that changing either the distribution of scatterer numbers or mixing proportion can give $\mathcal{K}$, Kummer-$\mathcal{U}$, and $\mathcal{G}^0$ distributed data. However, they have rather different polarimetry meanings. In the first case, the data represents only one type of scattering mechanism, while the second case represents a complex combination of different polarimetric scattering mechanisms.

In urban areas, man-made targets and natural targets are usually arranged alongside each other. The received data of a PolSAR system will be a mixture of responses from both distributed scatterers and point scatterers. To show the statistics of these areas, distributed scatterers with covariance matrix given by (5.19) and point scatterers given by (5.21) are generated and mixed:

$$\begin{aligned} \mathbf{S}_1 &= [5, 0, 0]^T \\ \mathbf{S}_2 &= [0, 5, 0]^T \\ \mathbf{S}_3 &= [10, 0, 0]^T \end{aligned} \tag{5.21}$$

Different percentages of point scatterers are tested, from 0.1% to 90%. From Fig. 5.10a to Fig. 5.10c, the log-cumulants of the simulated data where the distributed scatterers are mixed with one point scatter $\mathbf{S}_1$, two point scatterers $\mathbf{S}_1$ and $\mathbf{S}_2$, and one point scatterer $\mathbf{S}_3$, respectively, are shown. As it can be seen, adding up point scatterers of different

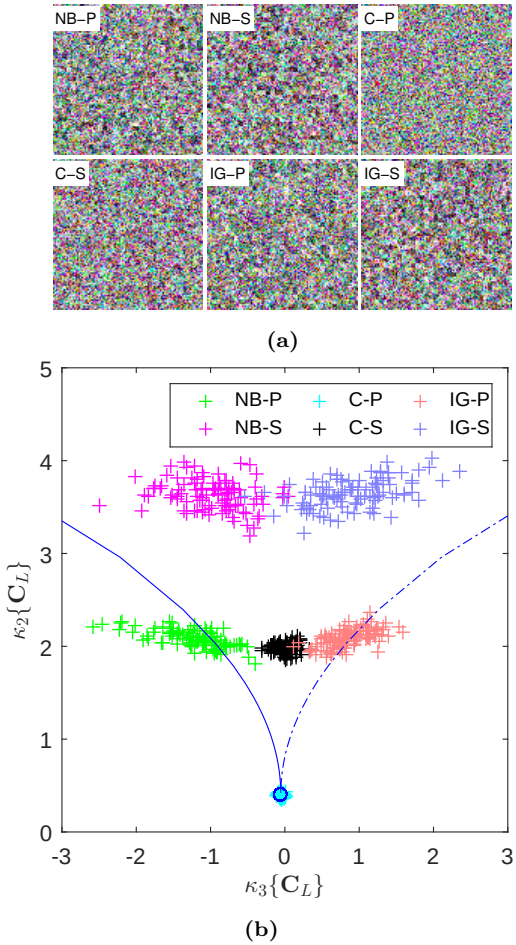

Figure 5.8: Simulated mixtures at spatial level and pixel level. Spatial mixtures with negative binomial distributed scatterer number (`NB-S`), constant scatterer number (`C-S`) and compound Poison distributed scatterer number (`IG-S`) are tested, as well as pixel level mixtures with the same scatterer number distributions, denoted by `NB-P`, `C-P`, and `IG-P`. The data are filtered using a 3×3 window.

types increases the heterogeneity of the simulated data, see Fig. 5.10a and Fig. 5.10b. By comparing Fig. 5.10a and Fig. 5.10c, we can see that increasing the amplitudes of the point scatterers result into more heterogeneity.

5.4 Experiments on Real SAR Data

Apart from simulated data, real PolSAR images, including the RADARSAT-2 Fine Quad-Pol data (`RST2`), the ALOS-2 level 1.1 data in High-sensitive Full-Pol mode (`ALOS2`), and the TerraSAR-X Stripmap Quad-Pol data (`TSX`) are analyzed. The first two images were

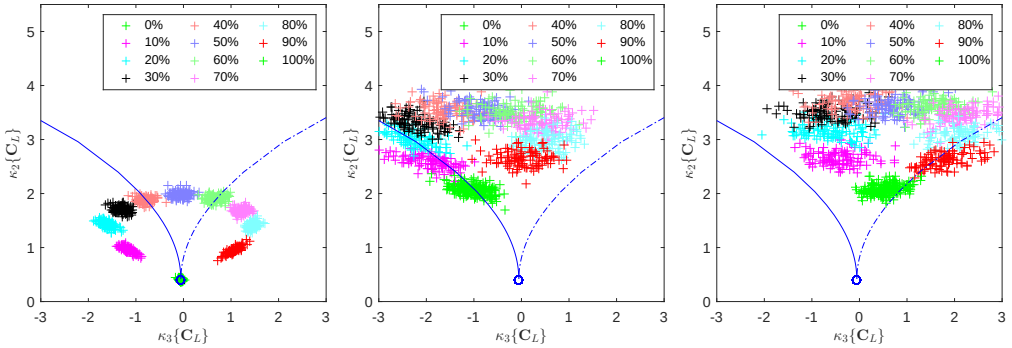

(a) **(b)** **(c)**

Figure 5.9: Simulated mixture of targets at spatial level with different mixing proportions. Matrix variate log-cumulants of the mixtures of scatterers specified by $\mathbf{C}_1$ and $\mathbf{C}_2$ are calculated. A 3×3 filtering is applied to simulated data. (a) Constant number. (b) Negative binomial distribution. (c) Compound Poison distribution.

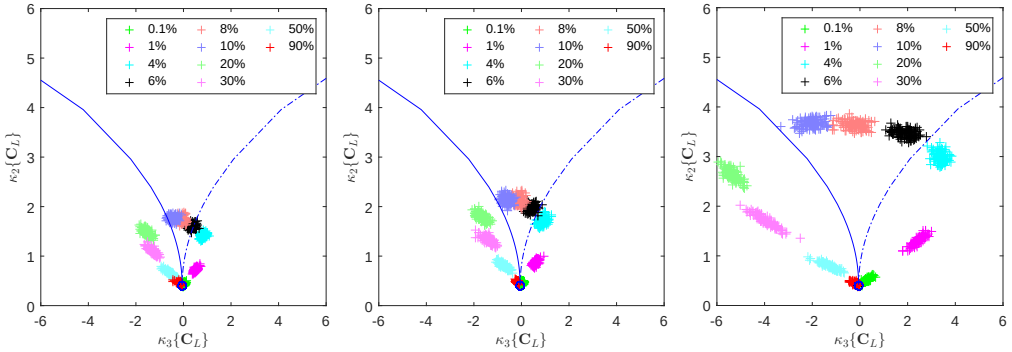

(a) **(b)** **(c)**

Figure 5.10: Simulated mixture of distributed targets and point targets. Log-cumulants cover the whole κ_2-κ_3 plane by changing the percentage of point scatterers. (a) Mixture with point scatterer $\mathbf{S}_1$. (b) Mixture with point scatterer $\mathbf{S}_1$ and $\mathbf{S}_2$. (c) Mixture with point scatterer $\mathbf{S}_3$.

acquired over Barcelona (Spain), and the third one over Vancouver (Canada). Original data are in the single look complex format, from which the sample covariance matrices are obtained after a multilook processing. Table 5.5 shows the size of the filtering window, as the pixels are correlated, the ENL is estimated using the log-determinant moment-based estimator [120]. Additional parameters such as the wave frequency, incidence angle, and the spatial resolution are also listed as a comparison. ROIs in the urban area, the agriculture area, the ocean and the forest area are selected to test, each covering 30×30 pixels. The Pauli decomposition and ROIs are shown in Fig. 5.11.

Fig. 5.12 shows the second-order and third-order matrix variate log-cumulants of the ROIs. The two ROIs in urban areas (`ROI 2` and `ROI 3`) of the `RST2` data and the `ALOS2` data represent two different urban structures, one is of tall and densely distributed apart-

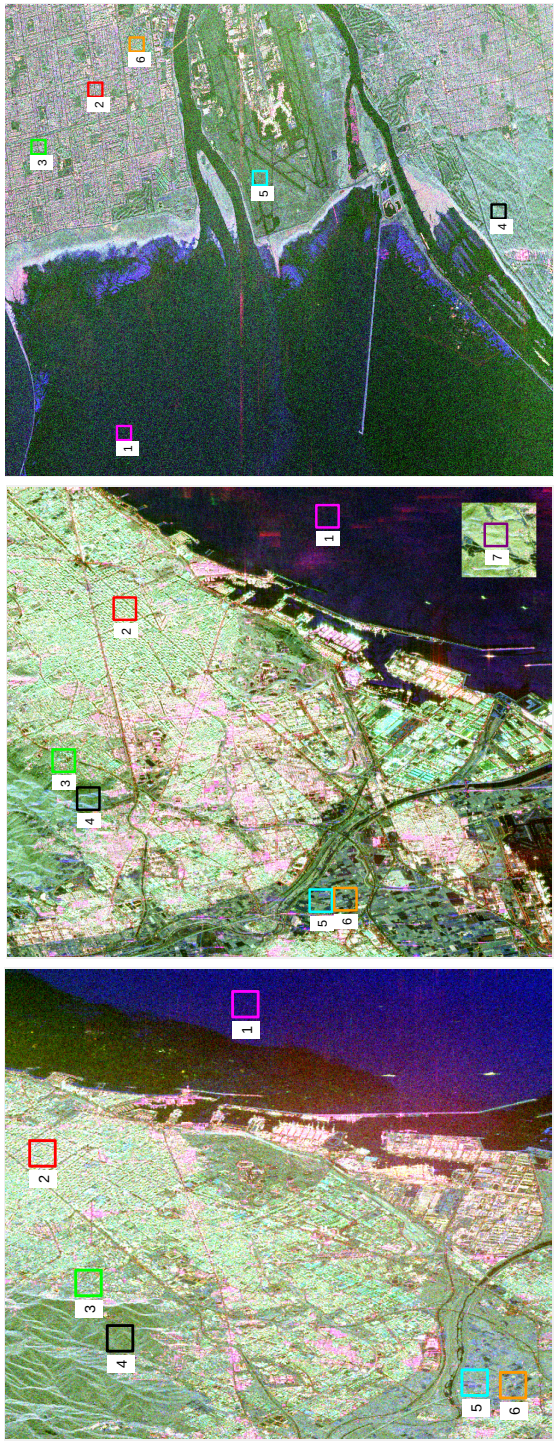

Figure 5.11: Pauli decomposition and test ROIs on real PolSAR data. The first two image were acquired over Barcelona, Spain, and the last one over Vancouver, Canada. (a) `RST2`. (b) `ALOS2`. (c) `TSX`.

Table 5.5: Parameters of Real PolSAR Data

ID	Freq.	Res. Rg × Az (m)	Incidence Angle (degs)	Window Size	ENL
RST2	C Band	11.1 × 7.6	28.9	3 × 3	5.61
ALOS2	L Band	3.49 × 3.84	33.9	5 × 5	15.15
TSX	X Band	1.18 × 6.60	32.6 / 24.6	5 × 5	7.77

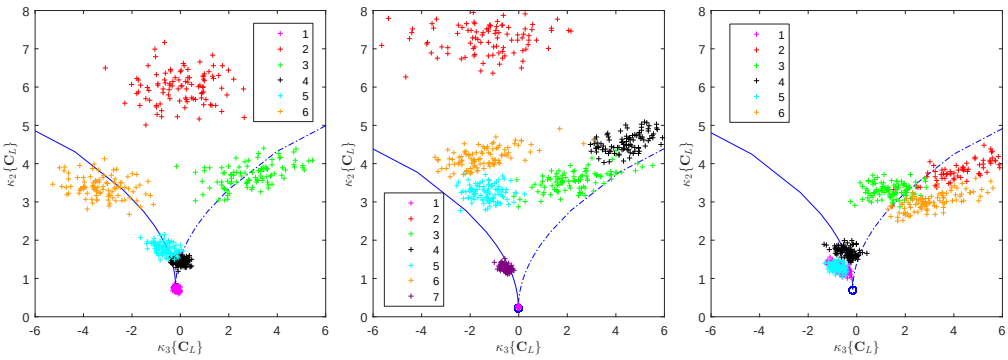

Figure 5.12: Matrix variate log-cumulants of real PolSAR data. Statistics show that the test ROIs can be modeled by different distributions, including $\mathcal{K}$, $\mathcal{G}^0$ and Kummer-$\mathcal{U}$ law. (a) RST2. (b) ALOS2. (c) TSX.

ments, the other is of short and sparse houses. This may be an explanation why different statistics, the $\mathcal{G}^0$ vs the Kummer-$\mathcal{U}$, are obtained. In agriculture areas (ROI 5 and ROI 6), $\mathcal{K}$ distribution is shown to be the most suitable model, due to the mixtures of different crop types. The forest area (ROI 4) shows weak texture in the RST2 and TSX data. But in the ALOS2 data, there is a strong fluctuation in the backscattering due to the radar foreshortening. To avoid the effect of radar image distortions, another forest region (purple rectangle) is analyzed, which is found to follow a $\mathcal{K}$ distribution. In most cases, texture is not observed in the sea areas. The results on the RST2 data and the ALOS2 data are similar, but quite different from that on the TXS data. One possible reason could be that they are calculated from different areas. In addition, the data of TerraSAR-X Stripmap Quad-Pol mode is an experimental product, before applying statistical analysis, a simple calibration is accomplished, where pixels with intensities below the noise level are discarded. This may be the reason why the results on the TSX data indicate a different behavior as those on RST2 and ALOS2 data.

Besides the space-borne sensors, data from a ground based SAR sensor, the UPC RiskSAR sensor [67], is also tested. More details about the RiskSAR system can be found in Section 2.3.3.1. The data was acquired in a small town called Sallent near Barcelona (Spain), see Fig. 5.13. Test ROIs covering different ground targets are chosen, including grass (ROI 1), houses (ROI 2 and ROI 3), trees (ROI 4 and ROI 5). There are

25×25 pixels in each ROI. The log-cumulants based on the l_2-norms are calculated, as shown in Fig. 5.14. We can see that the grass and the forest area show very weak texture, while the ROIs covering houses are extremely heterogeneous, where the second order log-cumulant can reach as large as 4. The backscattering from these areas are very strong [135], and the Pauli decomposition shows there exist very bright pixels as well as very dark pixels, see `ROI 2` for example.

5.5 Conclusions

The random walk model is studied, with the objective to give a physical insight of statistical PolSAR data texture models. Variable aspects of this model, including scatterer types, distributions of the scatterer number, as well as mixtures at pixel and spatial levels are considered, and corresponding simulation algorithms are provided. When simulating the scattering process, the scalar product model has been considered by assuming the same texture for all the polarimetric channels due to the complexity to properly simulate this type of variability. Statistical analysis are applied on simulated data obtained under different assumptions, as well as real SAR data acquired with different SAR sensors, wave frequencies and incidence angles.

From the simulated data, it is demonstrated that, according to the log-cumulants, i.e., the κ_2-κ_3 diagram, the same PolSAR data distribution could come from different scattering scenarios.

In the case of homogeneous data, it is demonstrated that the type of data distribution depends on both the scatterer number and the type of scatterer. Nevertheless, it is necessary to distinguish between low and high spatial resolution data. In the former case, the PolSAR data distribution is essentially determined by the distribution of the scatterer number, whereas in the later, the data distribution is affected by the distribution of the scatterer number as well as by the type of scatterer. The difference between these two cases is due to the number of scatterers inside the resolution cell. When this number is large, larger than N_{max} for example, the obtained data will be fully developed speckle. It has been also demonstrated that the value of N_{max} depends on the scatterer type. In addition, the effect of the scatterer type can be easily removed by the multilook processing. When a relatively large window is employed during the multilook processing, the non-Gaussianity mainly comes from the fluctuation of scatterer numbers.

In case of heterogeneous data, the PolSAR data distribution is determined by the mixture of different scatterers. This mixture can be considered at pixel, as well as at spatial level. The mixture of distributed scatterers at pixel level changes the covariance matrix, but the texture of the obtained data is determined by the fluctuations of the scatterer numbers. In the case of mixture at spatial level, the data distribution is determined not only by the distribution of scatterer number, but also by the proportion of the different scatter types in the mixture. Finally, the mixture of different targets will lead to extremely heterogeneous data, which provides a clue to analyze heterogeneous areas in PolSAR data, instead of introducing distributions with many parameters.

The configuration of a SAR sensor, for instance, frequency, incidence angle, and spatial resolution, could affect the distribution of some targets, as the information obtained by

(a)

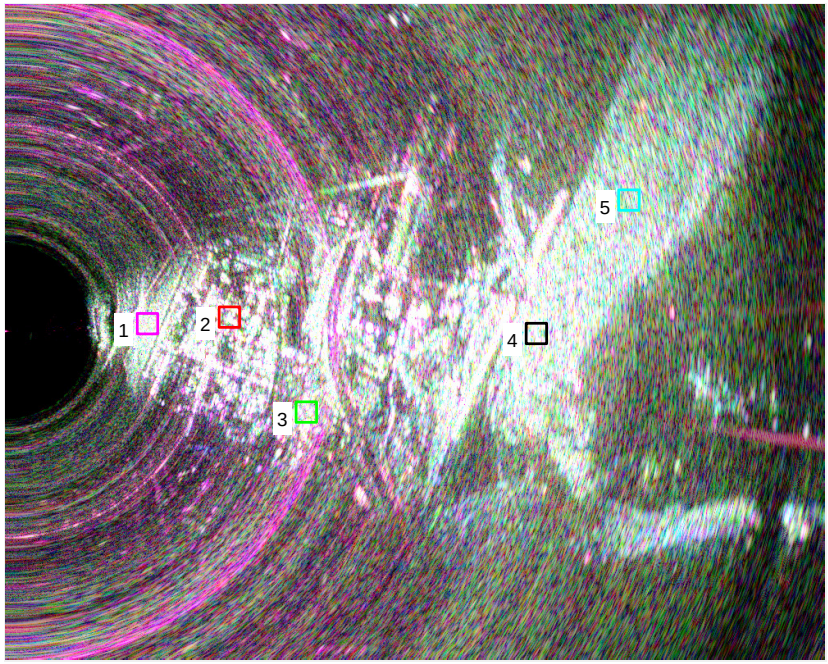

(b)

Figure 5.13: Test site of the RiskSAR data. (a) Photo of the test site. (b) Pauli decomposition of the SAR data and different ROIs.

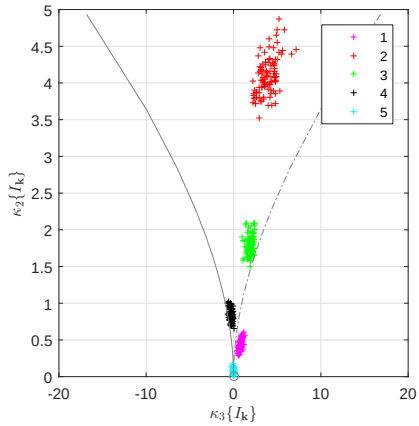

Figure 5.14: Log-cumulants of the l_2-norms on the RiskSAR data.

the different configurations is not the same. Normally, with higher frequency and higher resolution, more details could be observed, which will give stronger texture. A further thorough study on this topic is required.

It is observed that the same PolSAR data statistics can be obtained from different scattering scenarios. One possible physical explanation for different statistical PolSAR data models is the fluctuations of the scatterer numbers. Specially, negative binomial distributed scatterer number gives the $\mathcal{K}$ distribution, and compound Poisson distributed scatterer number gives the Kummer-$\mathcal{U}$ and the $\mathcal{G}^0$ distribution. Another possible explanation is the mixture of scatterers, where different data statistical models represent different mixture proportions. In other words, there is an ambiguity between the concept of texture and the concept of mixture in terms of the κ_2-κ_3 log-cumulants. How to distinguish these two explanations or to eliminate this ambiguity may require knowledge of the higher-order statistics or the spatial correlation.

6

Chapter 6

Higher Order Statistics for Data Analysis

It has been shown that non-gaussianity is a common fact in natural scenes of PolSAR data such as forests and wild open oceans, as well as human-made scenes like urban areas. There are two main ways to model the non-gaussian behavior of data: product model (or texture model) and finite mixture model. They represent two quite different scattering scenarios. Texture model describes targets from a single type. The polarimetric information (or scattering mechanism) conveyed by the targets is determined by the speckle vector, while the variation of radar cross section due to the changing of surface height or roughness is determined by the texture. On the contrary, finite mixture model describes combinations of various targets, each may give a specific scattering mechanism. More details about these models can be found in Chapter 3.

In the previous chapter, however, it was shown that the same log-cumulants of the second order and the third order may result from both of them. There is an ambiguity between the texture and the mixture according to those statistics. As they have different physical meanings, it is necessary to discriminate the two different concepts. In this chapter, higher order statistics, the fourth order log-cumulant in particular, are studied and they are found to be useful to accomplish this task.

The chapter is organized as follows. First, a simple review of texture models, scalar texture models specifically, is provided. Method on how to compute their log-cumulants is also reviewed. Then, log-cumulants of the finite mixture model are studied. A comparison with those of the texture models is drawn, which leads to an important finding that can be employed to distinguish the texture from the mixture. Experiments on both simulated data and real SAR data are presented in the last.

6.1 Non-Gaussian Models

As shown in Chapter 4, in order to visualize the fit of a statistical model to the testing data, some comparative statistics are required. The matrix variate log-cumulants are employed in this chapter. Log-cumulants of the texture model and finite mixture model are studied in the following sections.

6.1.1 Texture Model

The product model concerning various texture distributions was detailed in Section 3.2. Here, only the scalar texture distributions are considered as they provide explicit expressions of the PDFs and log-cumulants. The product model is also referred to as scale mixture of Gaussian distributions [74]. In fact, it can be viewed as some kind of mixture, where the mixture components have the same correlation structure. The correlation coefficients between different polarimetric channels are the same for all mixing components. The only difference is the radar cross section, which has the same effect on all channels. From the polarimetric point of view, all the mixing components can be viewed as the same kind of targets. The main objective of the product model is to describe the fluctuation radar cross section, also known as texture. Therefore, it is essentially different from the finite mixture model, as it will be shown later.

Theoretically, the texture could be modeled by any distribution, but first we confine ourselves to the Pearson ones, including gamma, inverse gamma, Fisher, beta and beta prime distributions, since they are the most common and widely studied distributions to model textures [12, 25, 26, 136]. The PDFs of the scattering vector or sample covariance matrix under the Pearson assumption are known as the $\mathcal{K}$, $\mathcal{G}^0$, Kummer-$\mathcal{U}$, $\mathcal{W}$ and $\mathcal{M}$ distributions, see Section 3.2.1. The vth order matrix variate log-cumulant of the sample covariance matrices is given by (Section 4.1.3)

$$\kappa_v\{\mathbf{C}_L\} = d^v \kappa_v\{\tau\} + \psi_d^{(v-1)}(L) + \delta(v-1)(\ln|\mathbf{\Sigma}| - d\ln L) \tag{6.1}$$

where $\mathbf{\Sigma}$ is the covariance matrix, $\delta(\cdot)$ is the Dirac function, and $\kappa_v\{\tau\}$ is the log-cumulants of the texture listed in Table 4.1. By varying the values of distribution parameters, the plotting of the second order log-cumulant against the third order log-cumulant will cover the whole 2D log-cumulant diagram, as shown in Fig. 6.1a. If we further consider the fourth order log-cumulant, the values could make up a continuous surface in the 3D space as illustrated in Fig. 6.1b. This 3D diagram will be called log-cumulant cube in the remainder of this chapter for simplicity.

Another well known distribution for the texture modeling is the GIG law, which leads to a $\mathcal{G}$ distribution for the product model [8]. PDFs about the $\mathcal{G}$ distribution can be found in Section 3.2.1.2. The matrix variate log-cumulants in this case can be calculated using [97]

$$\kappa_v\{\tau\} = \delta(v-1)\ln\eta + \ln K_p^{(v)}(\omega) \tag{6.2}$$

where

$$\ln K_p^{(v)}(\omega) = \left.\frac{d^v}{ds^v}\ln K_{p+s-1}(\omega)\right|_{s=1} \tag{6.3}$$

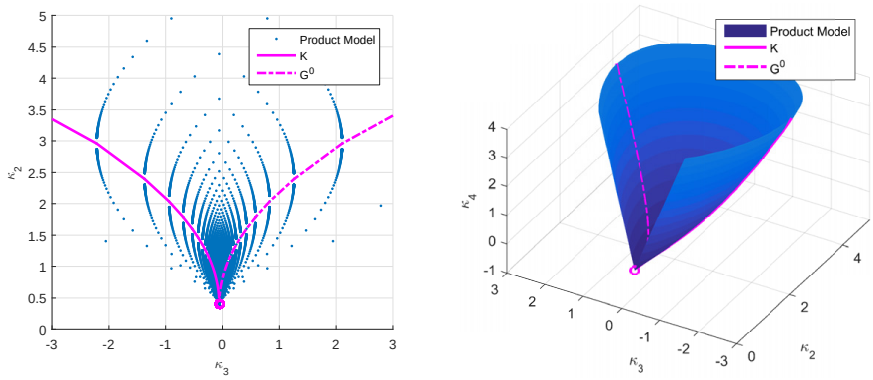

(a) (b)

Figure 6.1: Log-cumulant diagram and log-cumulant cube concerning the Pearson's distributions. The whole log-cumulant diagram is covered by distributions from Pearson's family. And they make up a continuous surface in the log-cumulant cube. (a) Log-cumulant diagram. (b) Log-cumulant cube.

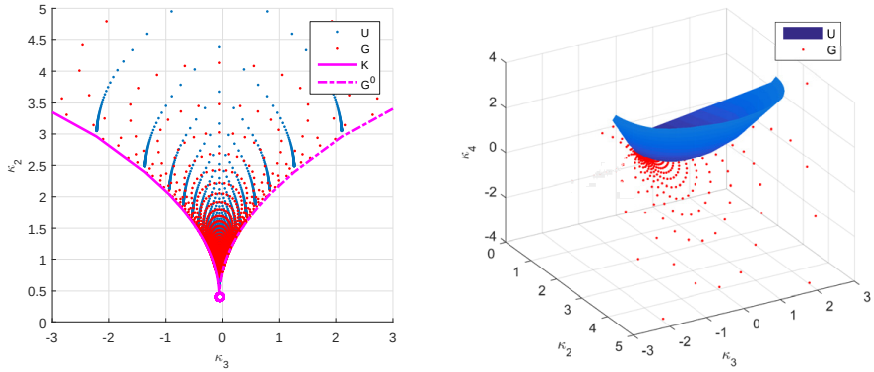

(a) (b)

Figure 6.2: Log-cumulant diagram and log-cumulant cube of the Kummer-$\mathcal{U}$ and the $\mathcal{G}$ laws. Same region is covered by the two distributions, but the fourth order log-cumulant is quite different. (a) Log-cumulant diagram. (b) Log-cumulant cube.

is the vth derivative of the logarithm of the modified Bessel function of the second kind, with respect to order. No special function exists for directly computing $\ln K_p^{(v)}(\omega)$, therefore, we must resort to numerical differentiation. It can be shown that the second order and the third order log-cumulants cover the same range as those of the Fisher distributed texture. And they share the same boundaries, the $\mathcal{K}$ distribution and the $\mathcal{G}^0$ distribution, as illustrated in Fig. 6.2a. However the fourth order log-cumulant is quite different. Fig. 6.2b shows that the points representing the GIG texture is below the surface representing the Fisher texture.

6.1.2 Finite Mixture Model

The finite mixture model was detailed in Section 3.3. Assume that the mixing components follow complex Wishart distributions such that the matrix-variate Mellin transform [26] of the PDF in (3.85) can be written as

$$\phi(s) = \left(\sum_{i=1}^{K} w_i |\mathbf{\Sigma}_i|^{s-d} \right) \frac{\Gamma_d(L+s-d)}{\Gamma_d(L)} \tag{6.4}$$

where $\mathbf{\Sigma}_i$ is the covariance matrix of the ith component, and $\Gamma_d(L)$ is the normalization factor given by (3.16). Let $|\mathbf{\Sigma}|_{min}$ denote the minimum determinant, $|\mathbf{\Sigma}|_{min} = \min(\{|\mathbf{\Sigma}_i|,\ i = 1, \cdots, K\})$, and $\rho_i = |\mathbf{\Sigma}_i|/|\mathbf{\Sigma}|_{min} \geq 1$, then the Mellin transform can be reformulated as

$$\phi(s) = \left(\sum_{i=1}^{K} w_i \rho_i^{s-d} \right) \frac{|\mathbf{\Sigma}|_{min}^{s-d} \Gamma_d(L+s-d)}{\Gamma_d(L)}. \tag{6.5}$$

By differentiating $\ln \phi(s)$ v times with respect to s and then letting $s = d$, the vth order log-cumulant is found to be

$$\kappa_v\{\mathbf{C}_L\} = \psi_d^{(v-1)}(L) + \beta_v + \delta(v-1) \ln |\mathbf{\Sigma}|_{min} \tag{6.6}$$

where $\psi_d^{(v-1)}(L)$ is the multivariate extension of the polygamma function, as expressed in (4.19), due to the multilook, and β_v is the result from the mixture which can be solved recursively by

$$\beta_v = r_v - \sum_{k=1}^{v-1} \binom{v-1}{k-1} \beta_k r_{v-k} \tag{6.7}$$

with $r_v = \sum_{i=1}^{K} w_i (\ln \rho_i)^v$. Some examples of expanded expressions for β_v are listed as follows:

$$\begin{aligned}
\beta_1 &= r_1 \\
\beta_2 &= r_2 - r_1^2 \\
\beta_3 &= r_3 - 3r_1 r_2 + 2r_1^3 \\
\beta_4 &= r_4 - 4r_1 r_3 - 3r_2^2 + 12 r_1^2 r_2 - 6 r_1^4 \\
\beta_5 &= r_5 - 5r_1 r_4 - 10 r_2 r_3 + 20 r_1^2 r_3 + 30 r_1 r_2^2 - 60 r_1^3 r_2 + 24 r_1^5
\end{aligned} \tag{6.8}$$

In the case of two mixing components, we have $r_v = w_1(\ln \rho_1)^v + w_2(\ln \rho_2)^v$, and either ρ_1 or ρ_2 is equal to 1 according to their definition. Ignoring the subscript, r_v is reduced to $w(\ln \rho)^v$, and the log-cumulants of the first several orders are

$$\begin{aligned}
\kappa_2\{\mathbf{C}_L\} &= \psi_d^{(1)}(L) + w(1-w)(\ln \rho)^2 \\
\kappa_3\{\mathbf{C}_L\} &= \psi_d^{(2)}(L) + w(1-w)(1-2w)(\ln \rho)^3 \\
\kappa_4\{\mathbf{C}_L\} &= \psi_d^{(3)}(L) + w(1-w)(1-6w+6w^2)(\ln \rho)^4 \\
\kappa_5\{\mathbf{C}_L\} &= \psi_d^{(4)}(L) + w(1-w)(1-2w)(1-12w+12w^2)(\ln \rho)^5
\end{aligned} \tag{6.9}$$

By changing the mixing proportions through w, the log-cumulants of the second order and the third order cover the whole κ_2-κ_3 plane, which has the same effect as by changing

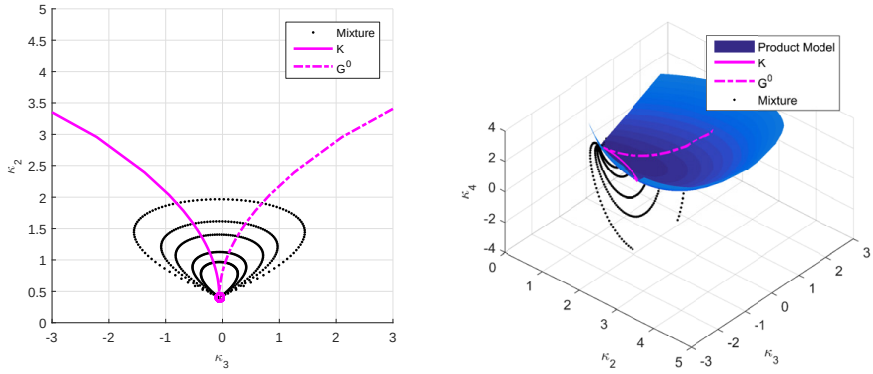

(a) (b)

Figure 6.3: Log-cumulant diagram and log-cumulant cube of mixtures of Wishart distributed components. (a) Log-cumulant diagram. The finite mixture model could cover the whole diagram by changing the mixing proportions and the ratio ρ. (b) Log-cumulant cube. Mixtures lie below the blue surface representing the product models concerning texture distribution from the Pearson's family.

the texture distribution of the product model as illustrated in Fig. 6.3a. However, they represent two rather different scattering scenarios, and there is a need to distinguish them.

The log-cumulants calculated from sample covariance matrices, $\kappa_v\{\mathbf{C}_L\}$, are represented by κ_v for short in the remainder of this chapter. Denote the log-cumulants of the product model by κ_v whereas those of the finite mixture model by $\tilde{\kappa}_v$ to avoid confusion. When there is an ambiguity between the product model and the finite mixture model, that is $\tilde{\kappa}_2 = \kappa_2$ and $\tilde{\kappa}_3 = \kappa_3$, the difference of the fourth order log-cumulant can be calculated from (6.1) and (6.9), giving

$$f = \tilde{\kappa}_4 - \kappa_4 = \frac{k_3^2 - 2k_2^3 - k_2 k_4}{k_2} \tag{6.10}$$

where $k_v = \kappa_v\{\tau\} - \psi_d^{(v-1)}(L)$. For all the Pearson's distributions in Table 4.1, it can be shown numerically that $f \leq 0$ holds for all the possible values of distribution parameters. Therefore, if we employ the log-cumulant cube, the result from the finite mixture models will be always below that from the product models considering Pearson texture, as shown in Fig. 6.3b, where the blue surface represents the log-cumulants of the product model and the points represent examples of mixtures of two components with different mixing proportions. Same result can be obtained from the $\mathcal{G}$ distribution, statistics from a finite mixture model always lie below those from the $\mathcal{G}$ distribution in the log-cumulant cube, see Fig. 6.4.

To determine whether the product model or the finite mixture model is better for the testing data, a simple approach based on the estimation error is proposed. By the central limit theorem, the estimation $\hat{\kappa}_4$ is Gaussian distributed when the sample size N is large, with variance given by (see [110] and Section 4.1.3 for more details)

$$\sigma^2 = \frac{1}{N}\left[\kappa_8 + 16\kappa_2\kappa_6 + 48\kappa_3\kappa_5 + 34\kappa_4^2 + 72\kappa_2^2\kappa_4 + 144\kappa_2\kappa_3^2 + 24\kappa_2^4\right]. \tag{6.11}$$

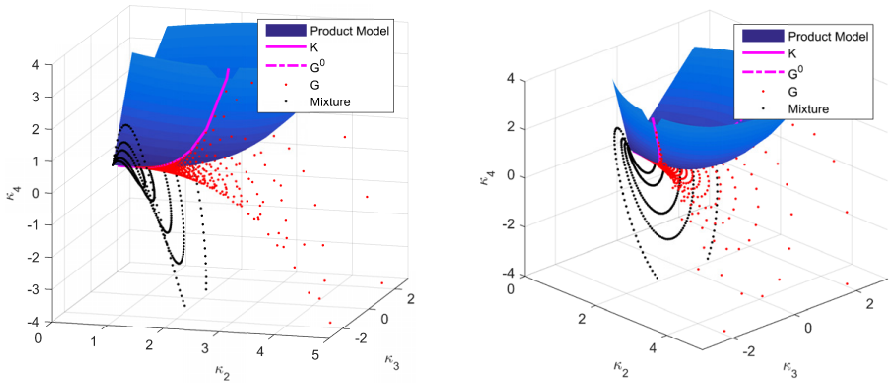

(a) **(b)**

Figure 6.4: Log-cumulant cube of mixtures and product models. Texture distribution from the Pearson's family and the GIG distribution are compared with the log-cumulants of discrete mixtures. They can be easily distinguished using the log-cumulant cube because the fourth order log-cumulants are quite different.

The theoretical log-cumulants κ_v are calculated from the product model distribution, where the distribution parameters are estimated using $\hat{\kappa}_2$ and $\hat{\kappa}_3$ [26] (see also Section 4.1.2). A test statistic to quantitatively evaluate the fit of a product model to the data can be defined as

$$T = \hat{\kappa}_4 - \kappa_4. \tag{6.12}$$

The absolute value $|T|$ can be interpreted as the vertical distance from a point representing the estimated statistics to the product model surface in the log-cumulant cube. If $|T| \leq \sigma$, we can justify that the product model is appropriate for the data, otherwise, the choice of the finite mixture model is preferable. The whole procedure is described in Algorithm 6.1.

Algorithm 6.1 Texture or Mixture

procedure TextureMixture($\mathbf{C}_L$)
  $\hat{\kappa}_v \leftarrow$ Estimate log-cumulants (Section 4.1.3)
  $\theta \leftarrow$ Estimate distribution parameters (Section 4.1.2)
  $\kappa_v \leftarrow$ Calculate (6.1)
  $\sigma^2 \leftarrow$ Calculate (6.11)
  $|T| \leftarrow$ Calculate (6.12)
  if $|T| \leq \sigma$ **then**
    Return "Texture"
  else
    Return "Mixture"
  end if
end procedure

6.2 Experiments

The log-cumulants of different orders, including the fourth order, are tested on both simulated and real SAR data. In the following sections, only distributions from the Pearson's family are considered, as the same procedure can be implemented on GIG distributed texture.

6.2.1 Simulated Data

First, we mix two Wishart distributed targets with different proportions. The covariance matrix of the first type is given by (6.13), which represents an X-Bragg surface scattering with a moderate roughness and a moisture of 40% [137]. The other covariance matrix is given by (6.14), representing a simple volume scattering. For each covariance matrix, 10000 samples are simulated.

$$\mathbf{C}_{xbragg} = \begin{bmatrix} 1.41 & 0 & 1.89 - 0.05j \\ 0 & 0.08 & 0 \\ 1.89 + 0.05j & 0 & 2.57 \end{bmatrix} \tag{6.13}$$

$$\mathbf{C}_{vol} = \frac{1}{8} \begin{bmatrix} 3 & 0 & 1 \\ 0 & 2 & 0 \\ 1 & 0 & 3 \end{bmatrix} \tag{6.14}$$

Log-cumulants calculated from the simulated data using the bootstrap method as introduced in Section 4.1.3 are shown in Fig. 6.5a. The result is in agreement with the description of the log-cumulants of the finite mixture model in the previous section, where the sample log-cumulants assume a manifold similar to those in Fig. 6.3b. Mixture of targets can be easily discriminated from the product model by the fourth order log-cumulants κ_4.

Mixtures of three targets are also simulated, with an additional covariance matrix given by (6.15), which is estimated from a forest area of an AirSAR data acquired over the Netherlands

$$\mathbf{C}_{real} = 10^{-3} \times \begin{bmatrix} 161 & -7 - 4j & 39 - j \\ -7 + 4j & 82 & -4 + 4j \\ 39 + j & -4 - 4j & 100 \end{bmatrix}. \tag{6.15}$$

Again, the proportions of the mixing components are changed to see their effect on the log-cumulants. It demonstrates once more that the mixture of targets have $\tilde{\kappa}_4$ smaller than κ_4 of the product model for the same κ_2 and κ_3 as shown in Fig. 6.5b.

The κ_2 and κ_3 are frequently employed to determine the texture distribution of SAR data. However, when the data are very heterogeneous, the use of only the κ_2 and κ_3 is not enough, as the data may be also a mixture of different targets. To show this, a pure target following the Kummer-$\mathcal{U}$ distribution, the mixture of two targets, and the mixture of three targets are simulated, each containing 10000 samples. From Fig. 6.6a, we can see that all the simulated data have similar values of κ_2 and κ_3. In this case, wrong conclusions will be drawn from the log-cumulant diagram, as the discrete mixtures will be interpreted as Kummer-$\mathcal{U}$ distributed data. Using the log-cumulant cube, the mixtures

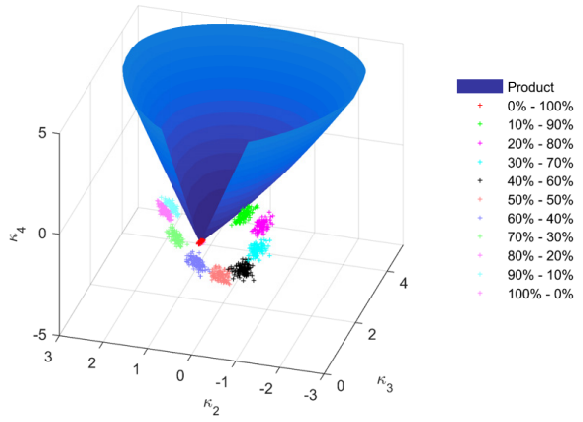

(a)

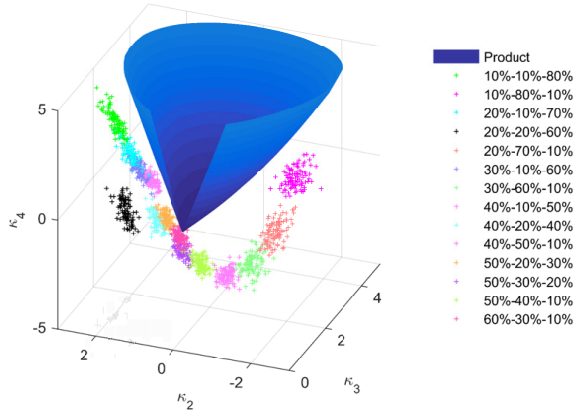

(b)

Figure 6.5: The log-cumulants of the mixture of 2 components as well as mixture of 3 components. (a) Mixture of 2 targets ($\mathbf{C}_{xbragg}$ - $\mathbf{C}_{vol}$). The point clouds representing different mixtures lie below the product model surface. (b) Mixture of 3 targets ($\mathbf{C}_{xbragg}$-$\mathbf{C}_{vol}$-$\mathbf{C}_{real}$). Mixture of 3 targets also have κ_4 smaller than the product models that have the same κ_2 and κ_3.

are distinguished from the pure target by the κ_4, see Fig. 6.6b. This is also validated by the quantitative assessment as shown in Table 6.1, where the mixtures have $|T|$ larger than σ.

The PDF contains complete information to characterize a distribution, all statistics including the moments and the cumulants are derived from the PDFs. In principle, the histograms would give a useful indication as to where the product model and the finite mixture model are different when κ_2 and κ_3 are equal. Fig. 6.7 shows the intensity histograms of the simulated data for each polarimetric channel separately. Indeed, there are some differences between the histograms from the pure targets and the mixtures. This is mainly due to the different mean values. But it is impossible to determine which one

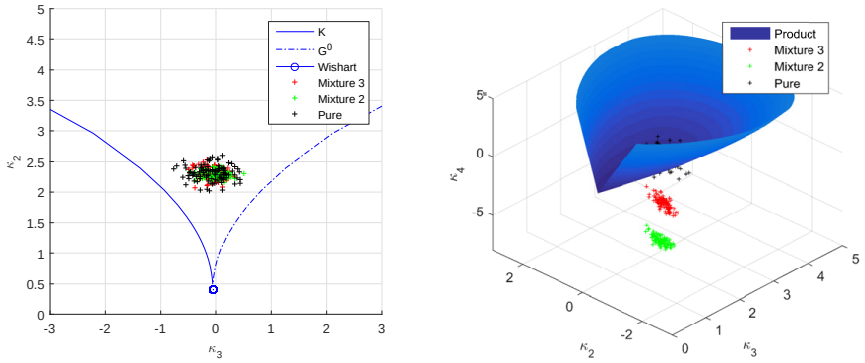

(a) **(b)**

Figure 6.6: The use of κ_4 to distinguish texture from mixture. (a) Log-cumulant diagram. Both textured data and mixtures produce the similar κ_2 and κ_3. (b) Log-cumulant cube. The textured data and mixtures have different κ_4.

Table 6.1: Quantitative Assessment on Simulated Data

Test	$\hat{\kappa}_4$	κ_4	$\lvert T \rvert$	σ^2	σ
Pure	0.2772	0.3910	0.1138	0.0841	0.2900
Mixture 2	-7.0766	0.3863	**7.4629**	0.0827	**0.2876**
Mixture 3	-3.7337	0.3982	**4.1319**	0.0861	**0.2934**

represents the mixture only from the histograms, since all of them are unimodal. If we approximate the data using one-dimensional Kummer-$\mathcal{U}$ distributions with different mean values (Section 3.2.1.3), the HH and HV channels of all simulated data seem to be well fitted. But for discrete mixtures, there is a large discrepancy between the histogram and the PDF of the VV channel data, especially for the mixture of 3 components. Although, histograms can be employed in this case, we need additional information about the data such as the knowledge of the Kummer-$\mathcal{U}$ distributions. As detailed in Chapter 4, statistics like Mellin kind statistics, or log-cumulants, are preferable. That's why here the log-cumulants are studied to discriminate the different concepts of texture and mixture.

6.2.2 Real SAR Data

Log-cumulants are also tested on an ALOS-2 High-sensitive Full-Pol mode data, which was acquired over Barcelona (Spain) in March 2015. The original data are in single-look complex format with processing level 1.1 and spatial resolution $3.49m \times 3.84m$ (Range $\times$ Azimuth). Before calculating the log-cumulants, a multilook process is applied using a 5×5 sliding window. The estimated equivalent number of looks is 14.46. Several ROIs over the urban area and sea area are tested, each covers 20×20 pixels.

The results are shown in Fig. 6.8. According to the log-cumulant diagram, the urban areas could be modeled by different distributions, depending on the composition of the area. For instance, the area with lots of trees (`ROI 4`) follows a $\mathcal{K}$ distribution, the

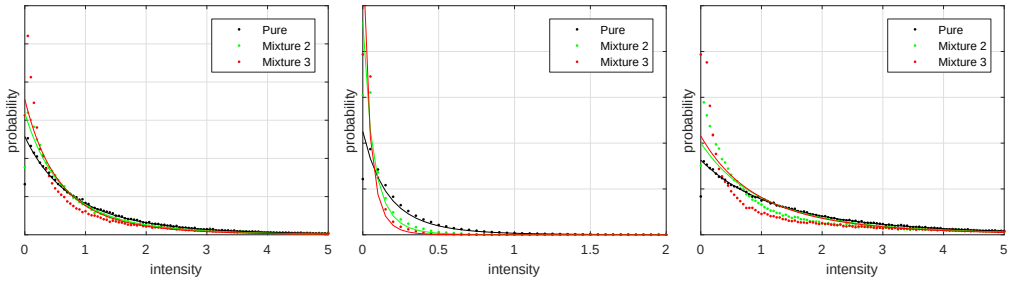

Figure 6.7: Histograms of the simulated pure target and mixtures. Histograms are represented by points and PDFs of the Kummer-$\mathcal{U}$ distributions by solid lines. All PDFs are unimodal, and they are not very spiky. It is difficult to tell which one represents the mixture and which one represents pure targets. (a) HH. (b) HV. (c) VV.

Table 6.2: Quantitative Assessment on ALOS-2 Data

ROI	$\hat{\kappa}_4$	κ_4	$\lvert T\rvert$	σ^2	σ
1-Blue	9.7922	9.4141	0.3781	116.8194	10.8083
2-Cyan	5.0368	3.1012	1.9356	27.0272	5.1988
3-Black	-6.3097	15.6604	**21.9701**	376.4956	**19.4035**
4-Red	-1.9748	3.4908	**5.4656**	22.5360	**4.7472**
5-Green	-0.0097	0.0028	0.0125	2.3339×10^{-4}	0.0153

area with tall apartments (`ROI 2` and `ROI 3`) follows a Kummer-U distribution, and area with short houses (`ROI 1`) can be modeled by a $\mathcal{G}^0$ distribution. The sea area is very homogeneous, which can be modeled by the Wishart distribution. However, the log-cumulant cube shows that the product model is not appropriate for some urban areas. There are two ROIs (`ROI 3` and `ROI 4`) producing a κ_4 smaller than 0, which is far below the surface representing the product model. Two ROIs (`ROI 1` and `ROI 2`) have part of points above the product model surface as well as part below it, and the quantitative assessment demonstrates that they can be modeled by product models, see Table 6.2. Note that the differences between $|T|$ and σ of the `ROI 3` and `ROI 4` are not so significant as those of the mixtures in Table 6.1, the main reason is that the sample size here is 400, which gives a larger estimation error.

Another experiment is performed on an airborne SAR data, a UAVSAR image (NASA 2010, retrieved from ASF DAAC 12 May 2016). The test site is in the West Panhandle of Florida (USA), and the data is in the multilook cross-product slant range format, with number of looks in the range dimension and azimuth dimension equal to 3 and 12 respectively. The ENL is estimated as 12.73 over a homogeneous ocean area. Four ROIs covering land types in ocean area (`ROI 1`), forest (`ROI 2`), wetland (`ROI 3`), and urban area (`ROI 4`), are analyzed, see Fig. 6.9. Thanks to a higher spatial resolution, $1.67m \times 0.8m$ (Range $\times$ Azimuth), each ROI contains 90×70 pixels, much more samples than the experiment on ALOS-2 data.

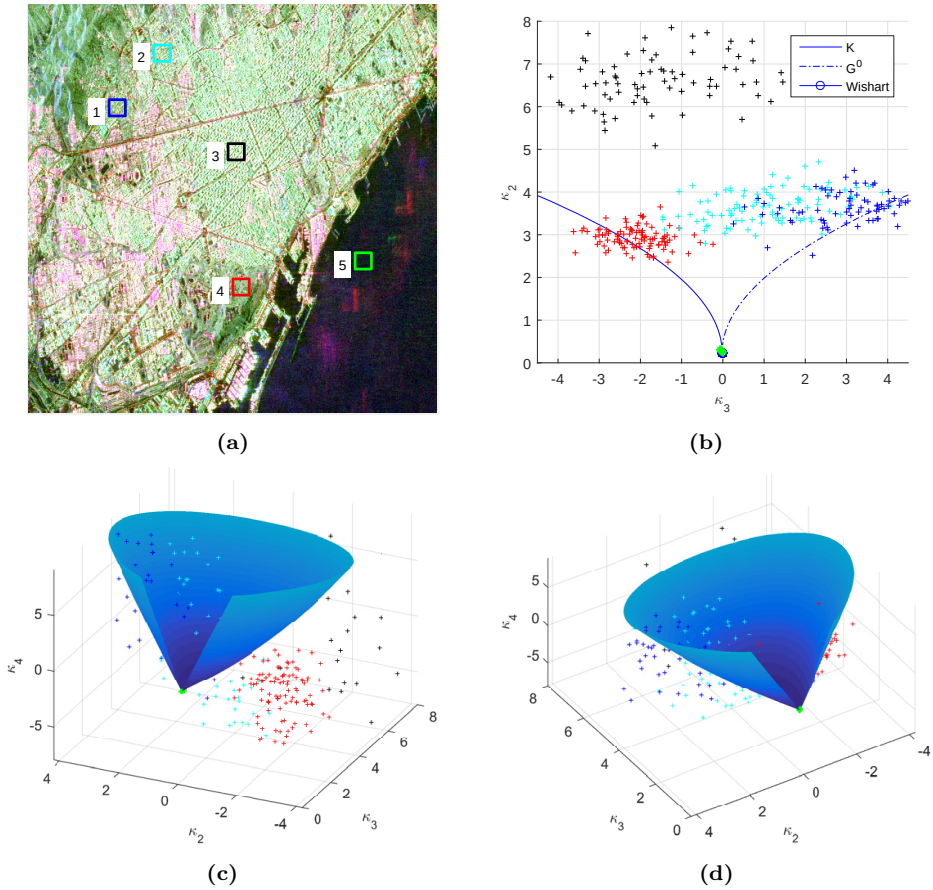

Figure 6.8: The log-cumulants on the ALOS-2 data. (a) Regions of interest. (b) Log-cumulant diagram. ROIs show different statistics depending on their composition. (c) and (d) Log-cumulant cube at two different perspectives. It shows some ROIs can be modeled by product models, while others should be represented using finite mixture model as $\kappa_4 < 0$.

The log-cumulants are shown in Fig. 6.10. From the log-cumulant diagrams, we can see that different ROIs show different statistical behaviors. The ocean area can be modeled by a Wishart distribution, and the forest by a $\mathcal{K}$ distribution. The wetland and the urban area are very heterogeneous, especially the urban area, which has a very small κ_3. The point clouds representing estimated statistics are less widely spread than those in Fig. 6.8b. This is because more samples are used to estimate the values. From the log-cumulant cubes, we can say that product models are proper for the sea area and forest area, while a finite mixture model make a better representation than a product model for the wetland area and the urban area, because the point clouds estimated from `ROI 1` and `ROI 2` are on the product model surface, whereas those from the `ROI 3` and `ROI 4` produce are below the surface. Actually, the Pauli decomposition in Fig. 6.9 shows that the first two ROIs are very homogeneous and `ROI 3` consists of different targets. Urban area, made up of distributed targets and point targets usually, has very large variance.

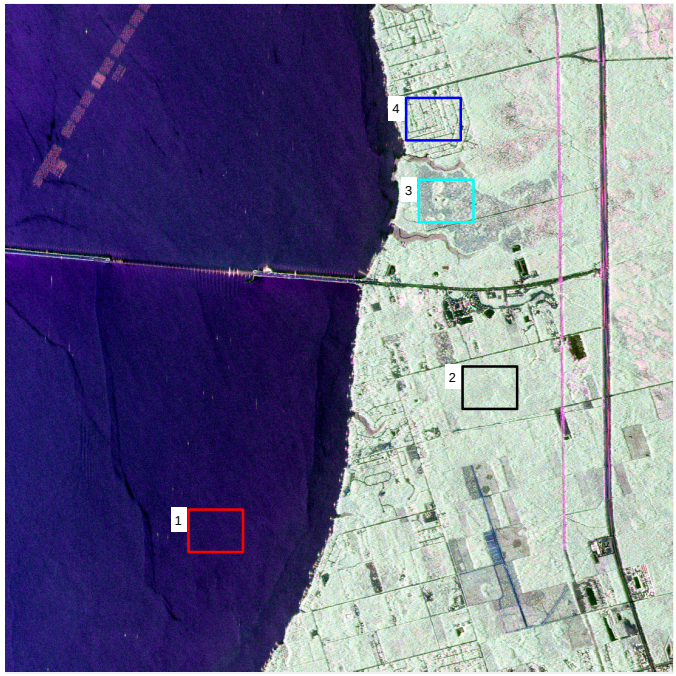

Figure 6.9: Test regions on the UAVSAR data. Four ROIs over different land types are tested, including sea, forest, wetland and urban area.

Table 6.3: Quantitative Assessment on UAVSAR Data

ROI	$\hat{\kappa}_4$	κ_4	$\lvert T \rvert$	σ^2	σ
1-Red	0.0001	0.0044	0.0042	2.7551×10^{-5}	0.0052
2-Black	0.5103	0.2521	**0.2582**	0.0229	**0.1512**
3-Cyan	-3.1126	3.6393	**6.7520**	2.4089	**1.5521**
4-Blue	27.8549	67.0174	**39.1626**	294.2683	**17.1542**

This can be verified by the log-cumulant cube in Fig. 6.10d, where both of the absolute values of κ_3 and κ_4 are very large.

A further validation by quantitative values is also performed. As shown in Table 6.3, the difference $|T|$ is large for both `ROI 3` and `ROI 4`, much larger than the estimation error. The values also show that a finite mixture model is more accurate than a product model for `ROI 2`. But from the log-cumulant cube, we can say that the area can be modeled by a $\mathcal{K}$ distribution, because the point cloud passes through the surface representing product models. As a matter of fact, when the fourth order log-cumulant is very small, the comparison using the estimation error is not quite effective. More robust methods must be introduced.

6.3 Conclusions

Higher order statistics are important to characterize PolSAR data, but there is little knowledge about how to make use of them. In this chapter, it is demonstrated that the fourth order log-cumulant is able to discriminate between different scattering scenarios. In particular, it can be physically interpreted to distinguish the scattering from a single type of target from a mixture of targets. As demonstrated both theoretically and experimentally, the mixture of two Wishart distributed components will have a smaller fourth order log-cumulant than the product model distributions with the same second and third order log-cumulants. This result is also extended to other mixtures covering more than two components. As a consequence, it is important to use higher order statistics for texture analysis of PolSAR data, especially when the data are very heterogeneous, as it may result from a mixture of different targets. A diagram combining the second, third and fourth order log-cumulants is proposed to distinguish the product model from finite mixture models, where texture distributions from the Pearson's family as well as the GIG distribution are considered.

The way to distinguish different models according to log-cumulants can be summarized as follows. For some product models, the use of κ_2 and κ_3 is enough to distinguish them, the $\mathcal{K}$ distribution and the Kummer-$\mathcal{U}$ distribution for example. To distinguish a product model from a finite mixture model, κ_4 is required, based on the results from the tested distributions ($\mathcal{K}$ distribution, Kummer-$\mathcal{U}$ distribution, the $\mathcal{G}^0$ distribution, the $\mathcal{M}$ and the $\mathcal{W}$ distribution). Regarding to how to distinguish the product models when the κ_2 and the κ_3 are the same, the Kummer-$\mathcal{U}$ distribution and the $\mathcal{G}$ distribution for instance, κ_4 also seems to be helpful, several validations show that the surface representing the $\mathcal{G}$ distribution is below that representing the Kummer-$\mathcal{U}$ distribution, but above the finite mixtures.

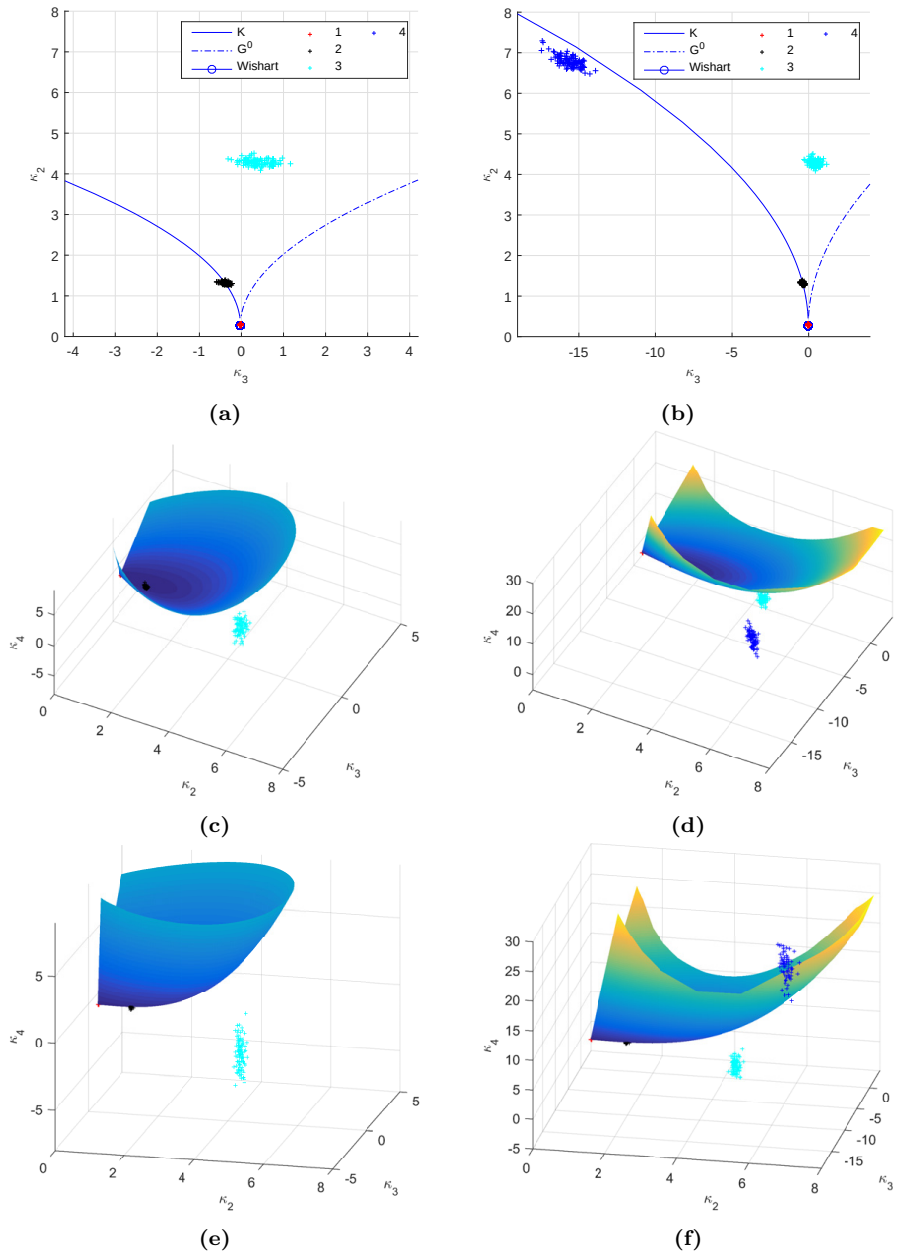

Figure 6.10: Log-cumulants on the UAVSAR data. The right column and left column are the same results but with different axes limits. (a) and (b), Log-cumulant diagrams. ROIs over different ground targets show different statistics. (c), (d), (e), and (f), Log-cumulant cubes. It shows some ROIs can be modeled by product models, while others should be represented using finite mixture model. (f) may be confusing because the blue point cloud seems to be over the product surface. But it is below the surface actually if we extend the surface.

7

Chapter 7
Conclusions and Future Lines

7.1 Conclusions

This thesis is dedicated to the study of texture analysis and physical interpretation of PolSAR data. It starts with a thorough review of the statistical models proposed in the literature. As exhibited, many models have been proposed. How to choose the most accurate one for a test data is a big challenge. In this thesis, the l_2-norms of the scattering vectors are studied, and they are found to be useful to extract statistical information from PolSAR data. Statistics based on the l_2-norms can be utilized to determine what distribution the data actually follow. As also noticed, more and more complex distributions are suggested by introducing various distributions to model the texture in the framework of the product model. Does these complex models make sense from the physical point of view? To answer this question, the random walk model is studied with the objective to obtain physical explanations for data statistics. It is found that both the mixture and the texture could give the same statistics such as log-cumulants of the second order and the third order. The two concepts, texture and mixture, represent two quite different scenarios. A further study was carried on to see if it is possible to distinguish them. And higher order statistics are demonstrated to be favorable in this task.

Knowledge of the exact statistical properties of the signal plays an important role in the applications of PolSAR data, such as speckle filtering, ground cover classification, etc. In the last two decades, a considerable research effort has been dedicated to finding accurate and efficient data models. As the starting point, a survey of the statistical models proposed to model PolSAR data is made. All the models are classified into three

categories: Gaussian, texture models, and finite mixture models. The texture models, widely studied due to their mathematical tractability, are the main concern of this thesis. They assume that the randomness of the SAR data is commonly due to two unrelated factors, texture and speckle, which are incorporated with a product operation leading to a doubly stochastic model called product model. The PDFs of the scattering vector and the sample covariance matrix in different models are reviewed.

The statistical properties of PolSAR data are characterized totally by the PDFs of the scattering vectors or the sample covariance matrices. However, it is difficult to use these PDFs directly, because they are multivariate ones. Normally, the statistics of each polarimetric channel are studied separately, and the correlation between different polarimetric channels are neglected. Another way is to analyze the determinant of sample covariance matrices. The widely used matrix variate log-cumulant is an example. But we need to filter the data to obtain the sample covariance matrices, which could change the true statistical properties of the data. To overcome these problems, the l_2-norms of the scattering vectors are investigated, and they are found to be a useful tool for texture analysis of PolSAR data. There are several advantages of using the l_2-norms.

- The polarimetric channels are not analyzed separately, and the correlations between polarimetric channels are considered.
- No filter is required which may average out the texture or give rise to mixture in certain scenes like urban areas.
- No estimation of the ENL, which is a difficult task in the analysis of PolSAR data, is needed.
- The norm is polarimetrically invariant, and the statistics are consistent when the scattering vectors are expressed in different polarization basis.

Two important statistics of the l_2-norm are studied, the normalized intensity and the log-cumulant. The former is an extension of the normalized intensity moments, which can be employed to evaluate the non-Gaussian behavior of the data easily. The values of different orders could reveal the polarimetric properties of PolSAR data, as well as the texture properties. The latter can be employed to identity the texture distribution of the data. Well established tools such as log-cumulant diagram can be reused. Estimators for those statistics are also provided. The estimator of normalized moments is biased, but the bias asymptotically vanishes as increasing the sample size. The estimator of log-cumulants is an unbiased one. For a given sample set, the variance of these estimators are deducted, therefore, further applications exploiting estimation error can be developed.

With the l_2-norm, we can extract statistical information from the measured data by most PolSAR sensors, scattering vectors, directly.

Based on the product model, a number of models have been proposed by introducing various distributions to model the texture, and more and more are coming. However, most of them are just results of pure mathematical calculations. In this thesis, the random walk model, which can be interpreted as a discrete analog of the SAR data focusing process, is studied with the objective to explain the statistical behavior of PolSAR data. Variations in the scatterer number and individual scatterers are introduced, as well as mixtures. By

simulating data under different circumstances, and analyzing them using tools such as log-cumulants based on the l_2-norms or matrix variate log-cumulants, several interesting ideas are found, as listed in the following.

- In the case of homogeneous data, it is demonstrated that the type of data distribution depends on both the scatterer number and the type of scatterer. For data of low or moderate spatial resolution, the statistics are essentially determined by the distribution of the scatterer number, whereas in high resolution data, the data distribution is affected by the distribution of the scatterer number as well as by the type of scatterer. The difference between the two cases is due to the average number of scatterers inside resolution cells. When this number is large, larger than N_{max} for example, the obtained data can be treated as fully developed speckle. It has been also demonstrated that the value of N_{max} depends on the scatterer type.

- In case of heterogeneous data, the PolSAR data distribution is determined by the mixture of different scatterers. The mixture can be considered at pixel and at spatial level as well. The mixture of distributed scatterers at pixel level changes the covariance matrix, but the texture of the obtained data is determined by the fluctuations of the scatterer numbers. When there is a mixture at spatial level, the data distribution is determined not only by the distribution of scatterer number, but also by the proportion of the different scatter types in the mixture.

- According to the second order and the third order log-cumulants, the same data statistics can be obtained by different scattering scenarios. One possible physical explanation for different statistical PolSAR data models is the fluctuations of the scatterer number in different resolution cells, in particular, negative binomial distribution for the $\mathcal{K}$ distribution, and compound Poisson distribution for Kummer-$\mathcal{U}$ and $\mathcal{G}^0$ distributions. Another possible explanation is the mixture of scatterers, where different data statistical models represent different mixture proportions. In other words, there is an ambiguity between the concept of texture and the concept of mixture in terms of the log-cumulants κ_2 and κ_3.

Same values of the statistics such as κ_2 and κ_3 can physically interpreted as either mixtures of targets or texture of the data. Models suggested to represent textured data in the literature may be just validated on mixtures instead of texture, especially those models proposed to model extremely heterogeneous data, as the mixture of different targets usually gives rise to very heterogeneous data.

Higher order statistics are important to characterize PolSAR data, but there is little knowledge about how to make use of them. In this thesis, it is demonstrated that the fourth order log-cumulant is able to discriminate between different scattering scenarios. In particular, it can be physically interpreted to distinguish the scattering from a single type of target from a mixture of targets. As demonstrated both theoretically and experimentally, the mixture of two Wishart distributed components will have a smaller fourth order log-cumulant than the product model distributions with the same second and third order log-cumulants. This result is also extended to other mixtures covering more than two components. Higher order statistics, as a consequence, are important to texture analysis, especially when the data are very heterogeneous, as it may result from a mixture of different targets. A diagram combining the second, third and fourth order

log-cumulants is proposed to distinguish the product model from finite mixture models, where texture distributions from the Pearson's family as well as the GIG distribution are considered.

Log-cumulants are of great value to texture analysis since the contribution of the texture and that of the speckle can be separated. The way to distinguish different models according to log-cumulants of the first several orders is summarized as follows.

- For some product models, the use of κ_2 and κ_3 is enough to distinguish them, the $\mathcal{K}$ distribution and the Kummer-$\mathcal{U}$ distribution for example.

- To distinguish a product model from a finite mixture model, κ_4 is required, based on the results from the tested distributions ($\mathcal{K}$ distribution, Kummer-$\mathcal{U}$ distribution, the $\mathcal{G}^0$ distribution, the $\mathcal{M}$ and the $\mathcal{W}$ distribution).

- Regarding how to distinguish the product models when the κ_2 and the κ_3 are the same, the Kummer-$\mathcal{U}$ distribution and the $\mathcal{G}$ distribution for instance, κ_4 also seems to be helpful. Several validations show that the surface representing the $\mathcal{G}$ distribution is below that representing the Kummer-$\mathcal{U}$ distribution, but above the finite mixtures.

In this thesis, several experiments on real SAR data are also implemented. The results confirm further that statistical information or texture information is of great importance. When different targets belong to a same category, saying crops or forest, the scattering mechanisms may be same, and similar polarimetric information will be observed. It is difficult to discriminate these targets by the polarimetric information only. Combining information conveyed by the texture, however, could give a better identification of targets. Crops of different types, and forests with trees of different characteristics can be further distinguished. In addition, the configuration of a SAR sensor, for instance, frequency, incidence angle, and spatial resolution, could affect the distribution of some targets, as the information obtained by the different configurations is not the same. Normally, with higher frequency and higher resolution, more details could be observed, which will give stronger texture.

7.2 Future Research Lines

There are several important topics in the field of statistical analysis of PolSAR data but not discussed in detail in this thesis, with a few examples listed as follows.

- This thesis details how to extract texture information from PolSAR data. It demonstrates that the statistical information is very important in characterizing SAR data by experiments on simulated data and real SAR data. But how to exploit the texture information in applications such as classification is not involved. Apparently, combining polarimetric information and texture information could improve the performance of classification algorithms as more knowledge is introduced. Therefore, a further study in this aspect is of great value.

- In many works, it is demonstrated that different polarimetric channels may have different textures and the correlation of texture parameters could be an important feature. Models exploiting this concept are referred to as multi-texture models. In this thesis, the multi-texture models are not studied intensively. Many results are based on the assumption of a scalar texture parameter. To make a more sound conclusion, some further work in multi-texture models is in need, especially in the direction of physical explanation of texture correlations between different polarimetric channels.
- In the finite mixture model, only Gaussian distributed components are considered in this thesis. So a further step is to take into account various mixing components. Robust algorithms to estimate the mixing number and the mixing weight are also necessary.

In summary, texture analysis of PolSAR data covers a wide range of topics. To make a better understanding of texture and to make good use of it, we still have a lot of work to do. The texture analysis and statistical modeling of PolSAR data is worthy of a further investigation.

A

Appendix A
Statistics of the l_2-Norm

A.1 Distribution of The Norm

Assume that $\mathbf{z}$ follows a complex Gaussian distribution, $\mathbf{z} \sim \mathcal{N}(0, \mathbf{\Sigma})$, where the covariance matrix can be diagonalized by $\mathbf{\Sigma} = \mathbf{P}^T\mathbf{D}\mathbf{P}$ with $\mathbf{P}$ orthogonal and $\mathbf{D} = \text{diag}(\lambda_1, \cdots, \lambda_d)$ diagonal. Then if $\mathbf{u} = \mathbf{P}\mathbf{z}$, by changing the variables, we have $\mathbf{u} \sim \mathcal{N}(0, \mathbf{D})$. The square of the l_2-norm of $\mathbf{u}$ can be written as a sum

$$I_{\mathbf{u}} = \mathbf{u}^\dagger\mathbf{u} = \sum_{i=1}^{d} I_i \tag{A.1}$$

where I_i follows an exponential distribution

$$p(I_i) = \frac{1}{\lambda_i} \exp\left(-\frac{I_i}{\lambda_i}\right) \tag{A.2}$$

with Moment Generating Function (MGF) given by

$$M_i(t) = \frac{1}{1 - \lambda_i t} \tag{A.3}$$

Since all I_is are independent (as the covariance matrix D is diagonal), the MGF of $I_{\mathbf{u}}$ is then the product of all components

$$M(t) = \prod_{i=1}^{d} \frac{1}{1 - \lambda_i t} = \sum_{i=1}^{d} \frac{p_i}{1 - \lambda_i t} \tag{A.4}$$

where

$$p_i = \frac{\lambda_i^{d-1}}{\prod_{j=1,j\neq i}^{d}(\lambda_i - \lambda_j)} \tag{A.5}$$

The PDF of $I_{\mathbf{u}}$, therefore, can be obtained from the MGF as

$$p(I_{\mathbf{u}}) = \sum_{i=1}^{d} \frac{p_i}{\lambda_i} \exp\left(-\frac{I_{\mathbf{u}}}{\lambda_i}\right). \tag{A.6}$$

The square of the l_2-norm of $\mathbf{z}$ can be calculated by

$$I_{\mathbf{z}} = (\mathbf{P}^{-1}\mathbf{u})^{\dagger}(\mathbf{P}^{-1}\mathbf{u}) = I_{\mathbf{u}} \tag{A.7}$$

which means $p(I_{\mathbf{z}}) = p(I_{\mathbf{u}})$.

A.2 Estimation Mean and Variance

In the following text, all the moments and normalized moments are calculated on the l_2-norm of the scattering vector. For simplicity, $m_v\{I_{\mathbf{k}}\}$ and $nm_v\{I_{\mathbf{k}}\}$ are replaced by m_v and nm_v. The mean value of $\hat{m}_v$ is given by [110]

$$\mathrm{E}\{\hat{m}_v\} = \mathrm{E}\left\{\frac{1}{N}\sum_{i=1}^{N}(\mathbf{k}_i^{\dagger}\mathbf{k}_i)^v\right\} = m_v \tag{A.8}$$

and the covariance by

$$\begin{aligned}\mathrm{Cov}\{\hat{m}_v, \hat{m}_\nu\} &= E\left\{\left(\frac{1}{N}\sum_{i=1}^{N}(\mathbf{k}_i^{\dagger}\mathbf{k}_i)^v - m_v\right)\left(\frac{1}{N}\sum_{i=1}^{N}(\mathbf{k}_i^{\dagger}\mathbf{k}_i)^\nu - m_\nu\right)\right\} \\ &= -m_v m_\nu + \frac{1}{N^2}E\left\{\sum_{i=1}^{N}(\mathbf{k}_i^{\dagger}\mathbf{k}_i)^{v+\nu} + \sum_{i=1}^{N}\sum_{j=1,j\neq i}^{N}(\mathbf{k}_i^{\dagger}\mathbf{k}_i)^v(\mathbf{k}_j^{\dagger}\mathbf{k}_j)^\nu\right\} \\ &= \frac{1}{N}(m_{v+\nu} - m_v m_\nu)\end{aligned} \tag{A.9}$$

Let $\nu = v$, the variance of $\hat{m}_v$ is obtained as

$$\mathrm{Var}\{\hat{m}_v\} = \frac{1}{N}(m_{2v} - m_v^2). \tag{A.10}$$

Define a function $f(x, y)$ as

$$f(x, y) = \frac{x}{y^v}, \tag{A.11}$$

then it can be expanded at (μ_x, μ_y) using the Taylor series [102]

$$\begin{aligned} f(x,y) =& \frac{\mu_x}{\mu_y^v} + (x-\mu_x)\frac{\partial f}{\partial x}\bigg|_{\mu_x,\mu_y} + (y-\mu_y)\frac{\partial f}{\partial y}\bigg|_{\mu_x,\mu_y} + \\ & \frac{1}{2}(x-\mu_x)^2\frac{\partial^2 f}{\partial x^2}\bigg|_{\mu_x,\mu_y} + \frac{1}{2}(y-\mu_y)^2\frac{\partial^2 f}{\partial y^2}\bigg|_{\mu_x,\mu_y} \\ & + (x-\mu_x)(y-\mu_y)\frac{\partial^2 f}{\partial x \partial y}\bigg|_{\mu_x,\mu_y} \\ & + O\left(\left((x-\mu_x)\frac{\partial}{\partial x} + (y-\mu_y)\frac{\partial}{\partial y}\right)^3 f\right) \end{aligned} \tag{A.12}$$

Ignoring all the terms higher than two and applying the expectation to individual terms gives the expectation of the function f

$$\mathrm{E}\{f(x,y)\} = \frac{\mu_x}{\mu_y^v} - Cov\{x,y\}\frac{v}{\mu_y} + Var\{y\}\frac{v(v+1)\mu_x}{2\mu_y^{v+2}} \tag{A.13}$$

Similarly, the variance of f can be obtained using the first-order terms of the Taylor series expansion:

$$\mathrm{Var}\{f(x,y)\} = Var\{x\}\frac{1}{\mu_y^{2v}} + Var\{y\}\frac{v^2\mu_x^2}{\mu_y^{2(v+1)}} - Cov\{x,y\}\frac{2v\mu_x}{\mu_y^{2v+1}} \tag{A.14}$$

Let $x = \hat{m}_v$, $y = \hat{m}_1$, $\mu_x = m_v$ and $\mu_y = m_1$, we have the mean value and variance of the estimator $n\hat{m}_v$ as

$$\mathrm{E}\{n\hat{m}_v\} = \frac{m_v}{m_1^v} + \frac{1}{N}\left(\frac{v(v+1)m_2 m_v}{2m_1^{v+2}} - \frac{v m_{v+1}}{m_1^{v+1}} + \frac{v(1-v)m_v}{2m_1^v}\right) \tag{A.15}$$

and

$$\begin{aligned} \mathrm{Var}\{n\hat{m}_v\} &= \frac{1}{N m_1^{2v}}\left[\frac{v^2 m_2 m_v^2}{m_1^2} - (v-1)^2 m_v^2 + m_{2v} - \frac{2v \cdot m_v m_{v+1}}{m_1}\right] \\ &= \frac{1}{N}[v^2 \cdot nm_2 \cdot nm_v^2 - (v-1)^2 \cdot nm_v^2 + nm_{2v} - 2v \cdot nm_v \cdot nm_{v+1}] \end{aligned} \tag{A.16}$$

As we can see, the bias of the estimator $n\hat{m}_v$ is given by

$$\begin{aligned} B =& \frac{1}{N}\left(\frac{v(v+1)m_2 m_v}{2m_1^{v+2}} - \frac{v m_{v+1}}{m_1^{v+1}} + \frac{v(1-v)m_v}{2m_1^v}\right) \\ =& \frac{1}{2N}(v(v+1)\cdot nm_2 \cdot nm_v - 2v \cdot nm_{v+1} - v(v-1)\cdot nm_v) \end{aligned} \tag{A.17}$$

which asymptotically goes to 0 when increasing the sample size N.

A.3 Log-Cumulant of the Speckle

The $\varphi_{I_\mathbf{z}}(s)$ shown in (4.47) consists of two parts. The first part is the logarithm of the gamma function, and there is a well known solution to the differential of it, the polygamma

function [25, 26]. For the second part, the logarithm of the CHSP (4.29), we can write it as

$$G(s) = \ln h_{s-1}(\lambda_1, \cdots, \lambda_d) \tag{A.18}$$

which leads to

$$h_{s-1}(\lambda_1, \cdots, \lambda_d) = e^{G(s)}. \tag{A.19}$$

Calculating the differential on both sides, the following is obtained

$$\begin{aligned} h'_{s-1}(\lambda_1, \cdots, \lambda_d) &= e^{G(s)} G'(s) \\ &= h_{s-1}(\lambda_1, \cdots, \lambda_d) G'(s) \end{aligned} \tag{A.20}$$

and according to the Leibniz's Rule, the $(v-1)$th order differential of the above equation is

$$h^{(v)}_{s-1}(s) = \sum_{k=0}^{v-1} \binom{v-1}{k} h^{(k)}_{s-1}(s) G^{(v-k)}(s) \tag{A.21}$$

with the differential of the CHSP is given by

$$h^{(v)}_{s-1}(s) = \sum_{i=1}^{d} p_i \lambda_i^{s-1} (\ln \lambda_i)^v. \tag{A.22}$$

Rearranging the result we get

$$G^{(v)}(s) = h^{(v)}_{s-1}(\lambda_1, \cdots, \lambda_d) - \sum_{k=1}^{v-1} \binom{v-1}{k} h^{(k)}_{s-1}(\lambda_1, \cdots, \lambda_d) G^{(v-k)}(s) \tag{A.23}$$

Let $\beta_v = G^{(v)}(s)\big|_{s=1}$ and $\tilde{h}(v) = h^{(v)}_{s-1}(\lambda_1, \cdots, \lambda_d)\Big|_{s=1}$, the result shown as (4.46) is obtained.

A.4 K-Statistics

This section list the k-statistics upto the fifth order. In the following, $\hat{\kappa}_v\{I_{\mathbf{k}}\}$ is denoted by $\hat{\kappa}_v$ for brevity. Let $N^{[v]} = \prod_{i=0}^{v-1}(N-i)$, the fourth order and the fifth order k-statistics are

$$\begin{aligned} \hat{\kappa}_4 &= \frac{1}{N^{[4]}}[(N^3+N^2)M_4 - 4(N^2+N)M_3M_1 - 3(N^2-N)M_2^2 + 12NM_2M_1^2 - 6M_1^4] \\ \hat{\kappa}_5 &= \frac{1}{N^{[5]}}[(N^4+5N^3)M_5 - 5(N^3+5N^2)M_4M_1 - 10(N^3-N^2)M_3M_2 + \\ &\quad 20(N^2+2N)M_3M_1^2 + 30(N^2-N)M_2^2M_1 - 60NM_2M_1^3 + 24M_1^5] \end{aligned} \tag{A.24}$$

The variances are given by

$$\begin{aligned}
\mathrm{Var}\{\hat{\kappa}_4\} &= \frac{\kappa_8}{N} + \frac{16\kappa_6\kappa_2}{N-1} + \frac{48\kappa_5\kappa_3}{N-1} + \frac{34\kappa_4^2}{N-1} + \frac{72N\kappa_4\kappa_2^2}{(N-1)(N-2)} \\
\mathrm{Var}\{\hat{\kappa}_5\} &= \frac{\kappa_{10}}{N} + \frac{25\kappa_8\kappa_2}{N-1} + \frac{100\kappa_7\kappa_3}{N-1} + \frac{200\kappa_6\kappa_4}{N-1} + \\
&\quad \frac{125\kappa_5^2}{N-1} + \frac{200N\kappa_6\kappa_2^2}{(N-1)(N-2)} + \frac{1200N\kappa_5\kappa_3\kappa_2}{(N-1)(N-2)} + \\
&\quad \frac{850N\kappa_4^2\kappa_2}{(N-1)(N-2)} + \frac{1500N\kappa_4\kappa_3^2}{(N-1)(N-2)} + \frac{600N^2(N+1)\kappa_4\kappa_2^3}{N^{[4]}} + \\
&\quad \frac{1800N^2(N+1)\kappa_3^2\kappa_2^2}{N^{[4]}} + \frac{120N^3(N+5)\kappa_2^5}{N^{[5]}}
\end{aligned} \tag{A.25}$$

The covariances are

$$\begin{aligned}
\mathrm{Cov}\{\hat{\kappa}_2, \hat{\kappa}_4\} &= \frac{\kappa_6}{N} + \frac{8\kappa_4\kappa_2}{N-1} + \frac{6\kappa_3^2}{N-1} \\
\mathrm{Cov}\{\hat{\kappa}_2, \hat{\kappa}_5\} &= \frac{\kappa_7}{N} + \frac{10\kappa_5\kappa_2}{N-1} + \frac{20\kappa_4\kappa_3}{N-1} \\
\mathrm{Cov}\{\hat{\kappa}_3, \hat{\kappa}_4\} &= \frac{\kappa_7}{N} + \frac{12\kappa_5\kappa_2}{N-1} + \frac{30\kappa_4\kappa_3}{N-1} + \frac{36N\kappa_3\kappa_2^2}{(N-1)(N-2)} \\
\mathrm{Cov}\{\hat{\kappa}_3, \hat{\kappa}_5\} &= \frac{\kappa_8}{N} + \frac{15\kappa_6\kappa_2 + 45\kappa_5\kappa_3 + 30\kappa_4^2}{N-1} + \frac{N(60\kappa_4\kappa_2^2 + 90\kappa_3^2\kappa_2)}{(N-1)(N-2)} \\
\mathrm{Cov}\{\hat{\kappa}_4, \hat{\kappa}_5\} &= \frac{\kappa_9}{N} + \frac{20\kappa_7\kappa_2 + 70\kappa_6\kappa_3 + 120\kappa_5\kappa_4}{N-1} \\
&\quad \frac{N(120\kappa_5\kappa_2^2 + 600\kappa_4\kappa_3\kappa_2 + 180\kappa_3^3)}{(N-1)(N-2)} + \frac{240N^2(N+1)\kappa_3\kappa_2^3}{N^{[4]}}
\end{aligned} \tag{A.26}$$

B

Appendix B

Statistics of the Random Walk Model

B.1 PDF of Intensity

Let the complex reflectivity of a resolution cell be $\tilde{R} = \sum_{k=1}^{N} a_k e^{i\varphi_k} = R_r + jR_i$, then the joint characteristic function of the real part and the imaginary part of R is

$$
\begin{aligned}
C(\tilde{u}) &= \mathrm{E}\left\{\exp\left(j(u_r R_r + u_i R_i)\right)\right\} \\
&= \mathrm{E}\left\{\exp\left(\sum_{k=1}^{N} j a_k (u_r \cos\varphi_k + u_i \sin\varphi_k)\right)\right\} \qquad \leftarrow \tilde{R} = \sum_{k=1}^{N} a_k e^{i\varphi_k} \\
&= \mathrm{E}\left\{\exp\left(\sum_{k=1}^{N} j u a_k (\cos\phi\cos\varphi_k + \cos\phi\sin\varphi_k)\right)\right\} \qquad \leftarrow u = |\tilde{u}|, \phi = \arg\tilde{u} \\
&= \mathrm{E}\left\{\exp\left(\sum_{k=1}^{N} j u a_k \cos(\varphi_k - \phi)\right)\right\} \\
&= \mathrm{E}\left\{\prod_{k=1}^{N} \exp\left[j u a_k \cos(\varphi_k - \phi)\right]\right\}
\end{aligned}
$$

with complex parameter $\tilde{u} = u_r + ju_i$. Using the Jacobi-Anger Expansion [102, p933, Eq 8.511-4]

$$e^{jz\cos\theta} = J_0(z) + 2\sum_{n=1}^{\infty} j^n J_n(z)\cos(n\theta)$$

where $J_0(z)$ is the Bessel function of the first kind, the following is obtained

$$\begin{aligned} C(\tilde{u}) &= \mathrm{E}\left\{\prod_{k=1}^{N}\left[J_0(ua_k) + 2\sum_{n=1}^{\infty} j^n J_n(ua_k)\cos(n(\varphi_k - \phi))\right]\right\} \\ &= \mathrm{E}\left\{\prod_{k=1}^{N} J_0(ua_k)\right\} \qquad \leftarrow p(\varphi_k) = \frac{1}{2\pi}, \varphi_k \in (0, 2\pi] \\ &= \mathrm{E}^N\left\{J_0(ua)\right\} \qquad \leftarrow a_k \text{ are independent} \end{aligned}$$

Here the samples a_k are replaced with the random variable a. Apply the inverse Fourier Transform on characteristic function

$$\begin{aligned} p(\tilde{R}; N) &= \left(\frac{1}{2\pi}\right)^2 \int_{-\infty}^{\infty}\int_{-\infty}^{\infty} \exp[-j(u_r R_r + u_i R_i)]\,\mathrm{E}^N\left\{J_0\left(\sqrt{u_r^2 + u_i^2}a\right)\right\} du_r du_i \\ &= \left(\frac{1}{2\pi}\right)^2 \int_0^{2\pi}\int_0^{\infty} u\exp[-j(uR_r\cos\phi + uR_i\sin\phi)]\,\mathrm{E}^N\{J_0(ua)\}dud\phi \end{aligned}$$

Letting $\tilde{R} = A\exp(\varphi)$ yields

$$\begin{aligned} p(A, \varphi; N) &= \left(\frac{1}{2\pi}\right)^2 \int_0^{2\pi}\int_0^{\infty} Au\exp\left[-juA(\cos\varphi\cos\phi + \sin\varphi\sin\phi)\right]\mathrm{E}^N\{J_0(ua)\}dud\phi \\ &= \left(\frac{1}{2\pi}\right)^2 \int_0^{2\pi}\int_0^{\infty} Au\exp[-juA\cos(\varphi - \phi)]\,\mathrm{E}^N\{J_0(ua)\}dud\phi \\ &= \left(\frac{1}{2\pi}\right)^2 \int_0^{\infty} Au\,\mathrm{E}^N\{J_0(ua)\}\left(\int_0^{2\pi}\exp[-juA\cos(\varphi - \phi)]d\phi\right)du \\ &= \left(\frac{1}{2\pi}\right)^2 \int_0^{\infty} Au\,\mathrm{E}^N\{J_0(ua)\}\left(\int_0^{2\pi} J_0(uA)d\phi\right)du \;\leftarrow \text{Jacobi-Anger Expansion} \\ &= \frac{1}{2\pi}\int_0^{\infty} AuJ_0(uA)\,\mathrm{E}^N\{J_0(ua)\}du \end{aligned}$$

As a result, the PDF of the amplitude and the intensity can be obtained as

$$\begin{aligned} p(A; N) &= \int_0^{2\pi} p_{A,\varphi}(A, \varphi; N)d\varphi \\ &= \int_0^{\infty} AuJ_0(uA)\,\mathrm{E}^N\{J_0(ua)\}du \end{aligned}$$

$$p(I; N) = \frac{1}{2}\int_0^{\infty} uJ_0(u\sqrt{I})\,\mathrm{E}^N\{J_0(ua)\}du$$

B.2 $\mathcal{K}$ Distribution

Let μ_N denote the mean value, the negative binomial distribution shown as (5.8) can be written as

$$p(N) = \binom{N+\alpha-1}{N} \frac{(\mu_N/\alpha)^N}{(1+\mu_N/\alpha)^{N+\alpha}}$$

Averaging the scatterer number, the PDF of the intensity becomes

$$\begin{aligned} p(I) &= \frac{1}{2}\int_0^\infty uJ_0(u\sqrt{I}) \left(\sum_{N=0}^{\infty} \mathrm{E}^N\{J_0(ua)\} p(N) \right) du \\ &= \frac{1}{2}\int_0^\infty uJ_0(u\sqrt{I}) \left(\frac{1}{(1+\mu_N/\alpha)^\alpha} \sum_{N=0}^{\infty} \binom{N+\alpha-1}{N} \frac{\mathrm{E}^N\{J_0(ua)\}(\mu_N/\alpha)^N}{(1+\mu_N/\alpha)^N} \right) du \end{aligned}$$

With the Binomial Theorem

$$\frac{1}{(1-x)^s} = \sum_{k=0}^{\infty} \binom{s+k-1}{k} x^k$$

the following can be obtained

$$\begin{aligned} p(I) &= \frac{1}{2}\int_0^\infty \frac{uJ_0(u\sqrt{I})}{(1+\mu_N/\alpha)^\alpha} \frac{1}{\left(1-\frac{\mathrm{E}\{J_0(ua)\}\mu_N/\alpha}{1+\mu_N/\alpha}\right)^\alpha} du \\ &= \frac{1}{2}\int_0^\infty \frac{uJ_0(u\sqrt{I})du}{(1+\mu_N[1-\mathrm{E}\{J_0(ua)\}]/\alpha)^\alpha} \end{aligned}$$

The Bessel function of first kind can be written in the form of power series [102, p918, Eq 8.440]

$$J_0(z) = \sum_{k=0}^{\infty} \left(-\frac{z^2}{4}\right)^k \left(\frac{1}{k!}\right)^2$$

It follows that the expectation $\mathrm{E}\{J_0(ua)\}$ takes the form

$$\begin{aligned} \mathrm{E}\{J_0(ua)\} &= \mathrm{E}\left\{ \sum_{k=0}^{\infty} \left(-\frac{u^2a^2}{4}\right)^k \left(\frac{1}{k!}\right)^2 \right\} \\ &= \sum_{k=0}^{\infty} \mathrm{E}\{a^{2k}\} \left(-\frac{u^2}{4}\right)^k \left(\frac{1}{k!}\right)^2 \end{aligned}$$

From the random walk model (5.1), the mean intensity of the complex phasors can be calculated by

$$\mathrm{E}\{a^2\} = \frac{\mu_I}{\mu_N}$$

where $\mu_I = \mathrm{E}\{A^2\}$ is the mean intensity from a resolution cell. As a matter of fact, the moments of the phasor amplitudes can be written as a function of μ_N^k

$$\mathrm{E}\{a^{2k}\} \propto \left(\frac{1}{\mu_N}\right)^k$$

when μ_N is very large, we have the following approximation by keeping only the first two terms in the sum

$$\mathrm{E}\{J_0(ua)\} \approx 1 - \frac{u^2\mu_I}{4\mu_N}$$

The distribution of the intensity then becomes

$$\begin{aligned} p_I(I) &\approx \frac{1}{2}\int_0^\infty \frac{uJ_0(u\sqrt{I})du}{(1+u^2\mu_I/4\alpha)^\alpha} \\ &= \frac{1}{2}\left(\frac{4\alpha}{\mu_I}\right)^\alpha \int_0^\infty \frac{uJ_0(u\sqrt{I})du}{(4\alpha/\mu_I+u^2)^\alpha} \end{aligned}$$

and following the integral identity [102, p678, Eq 6.565-4]

$$\int_0^\infty \frac{J_v(bx)x^{v+1}}{(x^2+a^2)^{\mu+1}}dx = \frac{a^{v-\mu}b^\mu}{2^\mu\Gamma(\mu+1)}K_{v-\mu}(ab)$$

gives

$$p(I) = \frac{2\alpha}{\mu_I\Gamma(\alpha)}\left(\frac{\alpha I}{\mu_I}\right)^{\frac{\alpha-1}{2}} K_{\alpha-1}\left(2\sqrt{\frac{\alpha I}{\mu_I}}\right)$$

Bibliography

[1] C. R. Jackson, J. R. Apel *et al.*, *Synthetic aperture radar marine user's manual*. US Department of Commerce, National Oceanic and Atmospheric Administration, National Environmental Satellite, Data, and Information Serve, Office of Research and Applications, 2004. (Cited on pages 1, 7, and 8.)

[2] Y. K. Chan and V. C. Koo, "An introduction to synthetic aperture radar (SAR)," *Progress In Electromagnetics Research B*, vol. 2, pp. 27–60, 2008. (Cited on pages 2, 8, and 9.)

[3] J.-S. Lee and E. Pottier, *Polarimetric radar imaging: from basics to applications*. CRC press, 2009. (Cited on pages 2, 7, 8, 12, 13, 14, 16, 18, 19, 32, 55, 61, and 63.)

[4] J. S. Lee, R. G. Mitchell, and R. Kwok, "Classification of multi-look polarimetric SAR imagery based on complex Wishart distribution," *International Journal of Remote Sensing*, vol. 15, no. 11, pp. 2299–2311, 1994. (Cited on pages 2, 31, 32, 36, 37, and 53.)

[5] J.-S. Lee, M. Grunes, T. Ainsworth, L.-J. Du, D. Schuler, and S. Cloude, "Unsupervised classification using polarimetric decomposition and the complex Wishart classifier," *IEEE Transactions on Geoscience and Remote Sensing*, vol. 37, no. 5, pp. 2249–2258, Sep 1999. (Cited on pages 2 and 31.)

[6] S. H. Yueh, J. A. Kong, J. K. Jao, R. T. Shin, and L. M. Novak, "K-distribution and polarimetric terrain radar clutter," *Journal of Electromagnetic Waves and Applications*, vol. 3, no. 8, pp. 747–768, 1989. (Cited on pages 2, 31, 37, 39, 75, 78, 79, and 84.)

[7] J. S. Lee, D. L. Schuler, R. H. Lang, and K. J. Ranson, "K-distribution for multi-look processed polarimetric SAR imagery," in *Geoscience and Remote Sensing Symposium, 1994. IGARSS '94. Surface and Atmospheric Remote Sensing: Technologies, Data Analysis and Interpretation., International*, vol. 4, Pasadena, USA, 1994, pp. 2179–2181. (Cited on pages 2, 31, 37, 38, and 39.)

[8] A. C. Frery, H. J. Muller, C. C. F. Yanasse, and S. J. S. Sant'Anna, "A model for extremely heterogeneous clutter," *IEEE Transactions on Geoscience and Remote Sensing*, vol. 35, no. 3, pp. 648–659, 1997. (Cited on pages 2, 31, 38, 39, 40, 41, 53, and 102.)

[9] C. C. Freitas, A. C. Frery, and A. H. Correia, "The polarimetric G distribution for SAR data analysis," *Environmetrics*, vol. 16, no. 1, pp. 13–31, 2005. (Cited on pages 2, 31, 38, and 39.)

[10] L. Bombrun and J.-M. Beaulieu, "Fisher distribution for texture modeling of polarimetric SAR data," *IEEE Geoscience and Remote Sensing Letters*, vol. 5, no. 3, pp. 512–516, 2008. (Cited on pages 2, 31, 38, 41, 42, 53, 54, and 87.)

[11] L. Bombrun, G. Vasile, M. Gay, and F. Totir, "Hierarchical segmentation of polarimetric SAR images using heterogeneous clutter models," *IEEE Transactions on Geoscience and Remote Sensing*, vol. 49, no. 2, pp. 726–737, 2011. (Cited on pages 2 and 31.)

[12] L. Bombrun, S. N. Anfinsen, and O. Harant, "A complete coverage of log-cumulant space in terms of distributions for Polarimetric SAR data," in *Proc. PolInSAR*, Frascati, Italy, 2011, pp. 1–8. (Cited on pages 3, 38, 42, 43, 54, 57, and 102.)

[13] G. Vasile, J.-P. Ovarlez, F. Pascal, and C. Tison, "Coherency matrix estimation of heterogeneous clutter in high-resolution polarimetric SAR images," *IEEE Transactions on Geoscience and Remote Sensing*, vol. 48, no. 4, pp. 1809–1826, 2010. (Cited on pages 3, 37, 38, and 61.)

[14] G. De Grandi, J.-S. Lee, D. Schuler, and E. Nezry, "Texture and speckle statistics in polarimetric SAR synthesized images," *IEEE Transactions on Geoscience and Remote Sensing*, vol. 41, no. 9, pp. 2070–2088, 2003. (Cited on pages 3, 4, 45, and 53.)

[15] P. Lombardo and A. Farina, "Coherent radar detection against K-distributed clutter with partially correlated texture," *Signal Processing*, vol. 48, no. 1, pp. 1–15, 1996. (Cited on pages 3, 46, and 47.)

[16] Y. Yu, S. Huan, and A. Torre, "Partially correlated K-distribution for multi-look polarimetric SAR images," in *Proc. CIE Symp.* IEEE, 1996, pp. 317–320. (Cited on page 3.)

[17] Y. Yu, "Textural-partially correlated polarimetric K-distribution," in *Geoscience and Remote Sensing Symposium Proceedings, 1998. IGARSS '98. 1998 IEEE International*, vol. 1, 1998, pp. 60–62. (Cited on pages 3, 45, and 46.)

[18] S. Khan and R. Guida, "The new dual-texutre G distribution for single-look PolSAR data," in *Geoscience and Remote Sensing Symposium (IGARSS), 2012 IEEE International*, Munich, Germany, 2012, pp. 1469–1472. (Cited on pages 3, 46, and 47.)

[19] T. Eltoft, S. N. Anfinsen, and A. P. Doulgeris, "A multitexture model for multilook polarimetric radar data," in *Geoscience and Remote Sensing Symposium (IGARSS), 2011 IEEE International*. Vancouver, Canada: IEEE, 2011, pp. 1048–1051. (Cited on pages 3, 45, and 46.)

[20] A. P. Doulgeris, S. N. Anfinsen, and T. Eltoft, "Segmentation of polarimetric SAR data with a multi-texture product model," in *Geoscience and Remote Sensing Symposium (IGARSS), 2012 IEEE International*, Munich, Germany, 2012, pp. 1437–1440. (Cited on pages 3 and 45.)

[21] Q. Zou, Y. Pi, and G. Liu, "Polarimetric speckle reduction by using multi-texture maximum likelihood method," in *Geoscience and Remote Sensing Symposium, 2000. Proceedings. IGARSS 2000. IEEE 2000 International*, vol. 5. IEEE, 2000, pp. 2287–2289. (Cited on page 3.)

[22] G. Moser, J. Zerubia, and S. B. Serpico, "Dictionary-based stochastic expectation-maximization for SAR amplitude probability density function estimation," *Geoscience and Remote Sensing, IEEE Transactions on*, vol. 44, no. 1, pp. 188–200, 2006. (Cited on pages 3, 47, 48, 53, 79, 86, and 87.)

[23] V. Krylov, G. Moser, S. B. Serpico, J. Zerubia *et al.*, "Modeling the statistics of high resolution SAR images," Institut national de recherche en informatique et en automatique, INRIA, Tech. Rep., 2008. (Cited on pages 3, 47, 48, 79, and 86.)

[24] Y. Wang, T. L. Ainsworth, and J. Lee, "On characterizing high-resolution SAR imagery using kernel-based mixture speckle models," *IEEE Geosci. Remote Sensing Lett.*, vol. 12, no. 5, pp. 968–972, 2015. [Online]. Available: http://dx.doi.org/10.1109/LGRS.2014.2370095 (Cited on pages 3, 47, and 48.)

[25] J.-M. Nicolas, "Introduction aux statistiques de deuxième espèce: applications des logs-moments et des logs-cumulants à l'analyse des lois d'images radar," *TS. Traitement du signal*, vol. 19, no. 3, pp. 139–167, 2002. (Cited on pages 4, 54, 55, 56, 57, 64, 93, 102, and 124.)

[26] S. N. Anfinsen and T. Eltoft, "Application of the matrix-variate Mellin transform to analysis of polarimetric radar images," *IEEE Transactions on Geoscience and Remote Sensing*, vol. 49, no. 6, pp. 2281–2295, 2011. (Cited on pages 4, 37, 54, 55, 56, 57, 58, 59, 64, 69, 102, 104, 106, and 124.)

[27] E. Jakeman and P. Pusey, "Significance of K distributions in scattering experiments," *Physical Review Letters*, vol. 40, no. 9, pp. 546–550, 1978. (Cited on pages 4, 31, 37, 39, 75, 78, 79, and 84.)

[28] C. Oliver, "The interpretation and simulation of clutter textures in coherent images," *Inverse Problems*, vol. 2, no. 4, pp. 481–518, 1986. (Cited on pages 4, 75, and 79.)

[29] G. Mercier, G. Moser, and S. B. Serpico, "Conditional copulas for change detection in heterogeneous remote sensing images," *IEEE Transactions on Geoscience and Remote Sensing*, vol. 46, no. 5, pp. 1428–1441, 2008. (Cited on page 4.)

[30] J.-S. Lee, M. R. Grunes, D. L. Schuler, E. Pottier, and L. Ferro-Famil, "Scattering-model-based speckle filtering of polarimetric SAR data," *IEEE Transactions on Geoscience and Remote Sensing*, vol. 44, no. 1, pp. 176–187, Jan 2006. (Cited on page 4.)

[31] A. P. Doulgeris, V. Akbari, and T. Eltoft, "Automatic PolSAR segmentation with the U-distribution and Markov random fields," in *Proc. EUSAR 2012 - 9th Eur. Conf. on Synthetic Aperture Radar*. VDE, 2012, pp. 183–186. (Cited on pages 4 and 31.)

[32] C. Tison, J.-M. Nicolas, F. Tupin, and H. Maître, "A new statistical model for markovian classification of urban areas in high-resolution SAR images," *Geoscience and Remote Sensing, IEEE Transactions on*, vol. 42, no. 10, pp. 2046–2057, 2004. (Cited on pages 4, 41, and 42.)

[33] O. Regniers, L. Bombrun, V. Lafon, and C. Germain, "Supervised classification of very high resolution optical images using wavelet-based textural features," *IEEE Transactions on Geoscience and Remote Sensing*, vol. 54, no. 6, pp. 3722–3735, June 2016. (Cited on page 4.)

[34] J. Curlander and R. McDonough, *Synthetic Aperture Radar: Systems and Signal Processing*, ser. Wiley Series in Remote Sensing and Image Processing. Wiley, 1991. (Cited on pages 7, 8, 9, 10, and 11.)

[35] J. van Zyl and Y. Kim, *Synthetic Aperture Radar Polarimetry*, ser. JPL Space Science and Technology Series. Wiley, 2011. (Cited on pages 9, 19, and 20.)

[36] D. Griffiths, *Introduction to Electrodynamics*, ser. Always learning. Pearson, 2013. (Cited on page 12.)

[37] S. Cloude, *Polarisation: Applications in Remote Sensing*. Oxford University Press, 2009. (Cited on page 15.)

[38] S. R. Cloude and E. Pottier, "A review of target decomposition theorems in radar polarimetry," *Geoscience and Remote Sensing, IEEE Transactions on*, vol. 34, no. 2, pp. 498–518, 1996. (Cited on page 16.)

[39] DLR, "TerraSAR-X." [Online]. Available: http://www.dlr.de/dlr/en/desktopdefault.aspx/tabid-10377/565_read-436/#/gallery/350 (Cited on page 20.)

[40] eoPortal Directory, "TerraSAR-X." [Online]. Available: https://directory.eoportal.org/web/eoportal/satellite-missions/content/-/article/terrasar-x#foot1%29 (Cited on page 20.)

[41] W. Pitz and D. Miller, "The TerraSAR-X satellite," *IEEE Transactions on Geoscience and Remote Sensing*, vol. 48, no. 2, pp. 615–622, Feb 2010. (Cited on page 20.)

[42] S. Buckreuss and B. Schattler, "The TerraSAR-X ground segment," *IEEE Transactions on Geoscience and Remote Sensing*, vol. 48, no. 2, pp. 623–632, Feb 2010. (Cited on page 20.)

[43] J. M. Irena Hajnsek and K. Papathanassiou, "Polarization capabilities and status of TerraSAR-X," in *Proceedings of the 4th International POLinSAR 2009 Workshop, Jan. 26-30, 2009, ESA/ESRIN, Frascati, Italy*, 2009. [Online]. Available: http://earth.esa.int/workshops/polinsar2009/participants/441/pres_9_hajnsek_441.pdf (Cited on page 20.)

[44] CSA, "RADARSAT-2." [Online]. Available: http://www.asc-csa.gc.ca/eng/satellites/radarsat2/ (Cited on page 21.)

[45] eoPortal Directory, "RADARSAT-2." [Online]. Available: https://directory.eoportal.org/web/eoportal/satellite-missions/r/radarsat-2 (Cited on page 21.)

[46] C. Livingstone, I. Sikaneta, C. Gierull, S. Chiu, and P. Beaulne, "RADARSAT-2 system and mode description," DTIC Document, Tech. Rep., 2006. [Online]. Available: http://dtic.mil/dtic/tr/fulltext/u2/a469927.pdf (Cited on page 21.)

[47] L. Brule and H. Baeggli, "RADARSAT-2 mission update," in *Geoscience and Remote Sensing Symposium, 2001. IGARSS '01. IEEE 2001 International*, vol. 6, 2001, pp. 2581–2583 vol.6. (Cited on page 21.)

[48] T. N. A. Hannevik, "RADARSAT-2 new modes," FFI (Norwegian Defence Research Establishment), Tech. Rep., July 10, 2012. [Online]. Available: http://www.ffi.no/no/Rapporter/12-01094.pdf (Cited on page 21.)

[49] JAXA, "ALOS-2 overview." [Online]. Available: http://www.eorc.jaxa.jp/ALOS-2/en/about/overview.htm (Cited on page 22.)

[50] eoPortal Directory, "ALOS-2." [Online]. Available: https://directory.eoportal.org/web/eoportal/satellite-missions/a/alos-2 (Cited on page 22.)

[51] Y. Kankaku, Y. Osawa, S. Suzuki, and T. Watanabe, "The overview of the L-band SAR onboard ALOS-2," in *Proceedings of Progress in Electromagnetics Research Symposium*, 2009, pp. 735–738. (Cited on page 22.)

[52] Y. Kankaku, S. Suzuki, and Y. Osawa, "ALOS-2 mission and development status," in *2013 IEEE International Geoscience and Remote Sensing Symposium - IGARSS*, July 2013, pp. 2396–2399. (Cited on page 22.)

[53] DLR, "F-SAR - the new airborne SAR system." [Online]. Available: http://www.dlr.de/hr/en/desktopdefault.aspx/tabid-2326/3776_read-5691/ (Cited on pages 23 and 24.)

[54] A. Reigber, R. Horn, A. Nottensteiner, P. Prats, R. Scheiber, K.-H. Bethke, and S. Baumgartner, "Current status of DLR's new F-SAR sensor," in *Synthetic Aperture Radar (EUSAR), 2010 8th European Conference on*. VDE, 2010, pp. 1–4. (Cited on page 23.)

[55] A. Reigber, K. Papathanassiou, M. Jger, and R. Scheiber, "First results of multispectral polarimetry and single-pass PolInSAR with the F-SAR airborne SAR instrument," in *2013 IEEE International Geoscience and Remote Sensing Symposium - IGARSS*, July 2013, pp. 2305–2308. (Cited on page 24.)

[56] A. Nadai, S. Uratsuka, T. Umehara, T. Matsuoka, T. Kobayashi, and M. Satake, "Development of X-band airborne polarimetric and interferometric SAR with submeter spatial resolution," in *2009 IEEE International Geoscience and Remote Sensing Symposium*, vol. 2, July 2009, pp. II–913–II–916. (Cited on pages 24 and 25.)

[57] S. Uratsuka, T. Kobayashi, T. Umehara, T. Matsuoka, A. Nadai, M. Satake, and J. Uemoto, "Airborne SAR development at NICT: Concept for new generation," *International Archives of the Photogrammetry, Remote Sensing and Spatial Information Science*, vol. XXXVIII, no. Part 8, pp. 133–136, 2010. (Cited on pages 24 and 25.)

[58] JAXA, "Pi-SAR-L2." [Online]. Available: http://www.eorc.jaxa.jp/ALOS/Pi-SAR-L2/about_pisar.html (Cited on page 24.)

[59] M. Shimada, N. Kawano, M. Watanabe, T. Motooka, and M. Ohki, "Calibration and validation of the Pi-SAR-L2," in *Synthetic Aperture Radar (APSAR), 2013 Asia-Pacific Conference on*, Sept 2013, pp. 194–197. (Cited on pages 24 and 25.)

[60] C. N. Koyama and M. Sato, "Estimation of soil moisture and debris pile volume from Pi-SAR2X and Pi-SAR-L2 square-flight data," in *2014 IEEE Geoscience and Remote Sensing Symposium*, July 2014, pp. 1516–1519. (Cited on page 25.)

[61] S. Hensley, K. Wheeler, G. Sadowy, C. Jones, S. Shaffer, H. Zebker, T. Miller, B. Heavey, E. Chuang, R. Chao, K. Vines, K. Nishimoto, J. Prater, B. Carrico, N. Chamberlain, J. Shimada, M. Simard, B. Chapman, R. Muellerschoen, C. Le, T. Michel, G. Hamilton, D. Robison, G. Neumann, R. Meyer, P. Smith, J. Granger, P. Rosen, D. Flower, and R. Smith, "The UAVSAR instrument: Description and first results," in *2008 IEEE Radar Conference*, May 2008, pp. 1–6. (Cited on page 25.)

[62] JPL, "UAVSAR." [Online]. Available: http://uavsar.jpl.nasa.gov/ (Cited on page 25.)

[63] Y. Lou, S. Hensley, R. Chao, E. Chapin, B. Heavy, C. Jones, T. Miller, C. Naftel, and D. Fratello, "UAVSAR instrument: Current operations and planned upgrades," in *Earth Science Technology Forum, Pasadena, California, June 21, 2011*, 2011. (Cited on page 25.)

[64] NASA, "EcoSAR." [Online]. Available: http://neptune.gsfc.nasa.gov/bsb/index.php?section=301 (Cited on page 25.)

[65] R. F. Rincon, T. Fatoyinbo, B. Osmanoglu, S. Lee, K. J. Ranson, G. Sun, M. Perrine, and C. D. Toit, "ECOSAR: P-band digital beamforming polarimetric and single pass interferometric SAR," in *2015 IEEE Radar Conference (RadarCon)*, May 2015, pp. 0699–0703. (Cited on page 26.)

[66] A. Aguasca, A. Broquetas, J. J. Mallorqui, and X. Fabregas, "A solid state L to X-band flexible ground-based SAR system for continuous monitoring applications," in *Geoscience and Remote Sensing Symposium, 2004. IGARSS '04. Proceedings. 2004 IEEE International*, vol. 2, Sept 2004, pp. 757–760. (Cited on pages 26 and 27.)

[67] R. Iglesias, A. Aguasca, X. Fabregas, J. Mallorqui, D. Monells, C. Lopez-Martinez, and L. Pipia, "Ground-based polarimetric SAR interferometry for the monitoring of terrain displacement phenomena-part I: Theoretical description," *Selected Topics in Applied Earth Observations and Remote Sensing, IEEE Journal of*, vol. 8, no. 3, pp. 980–993, March 2015. (Cited on pages 27 and 97.)

[68] J. W. Goodman, "Some fundamental properties of speckle," *JOSA*, vol. 66, no. 11, pp. 1145–1150, 1976. (Cited on pages 31, 32, 75, 76, 77, and 83.)

[69] C. López-Martínez and X. Fàbregas, "Model-based polarimetric SAR speckle filter," *Geoscience and Remote Sensing, IEEE Transactions on*, vol. 46, no. 11, pp. 3894–3907, 2008. (Cited on page 31.)

[70] A. Alonso-González, C. López-Martínez, and P. Salembier, "Filtering and segmentation of polarimetric sar data based on binary partition trees," *Geoscience and Remote Sensing, IEEE Transactions on*, vol. 50, no. 2, pp. 593–605, 2012. (Cited on pages 31 and 36.)

[71] S. Foucher and C. Lopez-Martinez, "Analysis, evaluation, and comparison of polarimetric SAR speckle filtering techniques," *Image Processing, IEEE Transactions on*, vol. 23, no. 4, pp. 1751–1764, 2014. (Cited on page 31.)

[72] J.-S. Lee, M. R. Grunes, and G. De Grandi, "Polarimetric SAR speckle filtering and its implication for classification," *Geoscience and Remote Sensing, IEEE Transactions on*, vol. 37, no. 5, pp. 2363–2373, 1999. (Cited on page 31.)

[73] P. R. Kersten, J.-S. Lee, and T. L. Ainsworth, "Unsupervised classification of polarimetric synthetic aperture radar images using fuzzy clustering and EM clustering," *Geoscience and Remote Sensing, IEEE Transactions on*, vol. 43, no. 3, pp. 519–527, 2005. (Cited on page 31.)

[74] A. P. Doulgeris, S. N. Anfinsen, and T. Eltoft, "Classification with a non-Gaussian model for PolSAR data," *IEEE Transactions on Geoscience and Remote Sensing*, vol. 46, no. 10, pp. 2999 – 3009, 2008. (Cited on pages 31, 37, 39, 80, and 102.)

[75] E. Jakeman and P. N. Pusey, "A model for non-Rayleigh sea echo," *IEEE Transactions on Antennas and Propagation*, vol. 24, no. 6, pp. 806–814, 1976. (Cited on pages 31, 53, and 55.)

[76] C. Oliver and S. Quegan, *Understanding synthetic aperture radar images*. SciTech Publishing, 2004. (Cited on page 32.)

[77] H. J. Rabal and R. A. Braga Jr, *Dynamic laser speckle and applications*. CRC Press, 2008. (Cited on page 32.)

[78] V. S. Frost, J. A. Stiles, K. S. Shanmugan, and J. C. Holtzman, "A model for radar images and its application to adaptive digital filtering of multiplicative noise," *IEEE Transactions on Pattern Analysis and Machine Intelligence*, vol. PAMI-4, no. 2, pp. 157–166, March 1982. (Cited on page 32.)

[79] J. Kong, S. Yueh, H. Lim, R. Shin, and J. Van Zyl, "Classification of earth terrain using polarimetric synthetic aperture radar images," *Progress In Electromagnetics Research*, vol. 3, pp. 327–370, 1990. (Cited on page 32.)

[80] K. Sarabandi, "Derivation of phase statistics from the Mueller matrix," *RADIO SCIENCE-WASHINGTON-*, vol. 27, pp. 553–553, 1992. (Cited on page 32.)

[81] F. Ulaby, K. Sarabandi, and A. Nashashibi, "Statistical properties of the Mueller matrix of distributed targets," in *Radar and Signal Processing, IEE Proceedings F*, vol. 139, no. 2. IET, 1992, pp. 136–146. (Cited on page 32.)

[82] N. R. Goodman, "Statistical analysis based on a certain multivariate complex Gaussian distribution (an introduction)," *The Annals of Mathematical Statistics*, vol. 34, no. 1, pp. 152–177, 1963. (Cited on pages 32, 35, and 76.)

[83] R. J. A. Tough, D. Blacknell, and S. Quegan, "A statistical description of polarimetric and interferometric synthetic aperture radar data," in *Proc. R. Soc. Lond. A, Math. Phys. Sci.*, vol. 449, no. 1937, 1995, pp. 567–589. (Cited on pages 33 and 34.)

[84] M. Abramowitz and I. A. Stegun, *Handbook of mathematical functions: with formulas, graphs, and mathematical tables*. Courier Corporation, 1964, vol. 55. (Cited on pages 34, 36, 41, 42, 43, 49, and 78.)

[85] J.-S. Lee, K. W. Hoppel, S. A. Mango, and A. R. Miller, "Intensity and phase statistics of multilook polarimetric and interferometric SAR imagery," *IEEE Transactions on Geoscience and Remote Sensing*, vol. 32, no. 5, pp. 1017–1028, 1994. (Cited on page 34.)

[86] C. Walck, *Hand-book on statistical distributions for experimentalists*. University of Stockholm, 2007. (Cited on pages 35, 39, 41, 42, 43, 61, 65, and 84.)

[87] C. López-Martínez and X. Fabregas, "Polarimetric sar speckle noise model," *Geoscience and Remote Sensing, IEEE Transactions on*, vol. 41, no. 10, pp. 2232–2242, 2003. (Cited on page 36.)

[88] C. Lopez-Martinez, E. Pottier, and S. R. Cloude, "Statistical assessment of eigenvector-based target decomposition theorems in radar polarimetry," *Geoscience and Remote Sensing, IEEE Transactions on*, vol. 43, no. 9, pp. 2058–2074, 2005. (Cited on page 36.)

[89] S. N. Anfinsen, T. Eltoft, and A. P. Doulgeris, "A relaxed wishart model for polarimetric SAR data," in *Proc. PolInSAR*, Frascati, Italy, 2009, pp. 26–30. (Cited on page 36.)

[90] P. R. Kersten and S. N. Anfinsen, "A flexible and computationally efficient density model for the multilook polarimetric covariance matrix," in *Proc. EUSAR 2012 - 9th Eur. Conf. on Synthetic Aperture Radar*, Nuremberg, Germany, 2012, pp. 760–763. (Cited on page 36.)

[91] P. R. Kersten, S. N. Anfinsen, and A. P. Doulgeris, "The Wishart-Kotz classifier for multilook polarimetric SAR data," in *Geoscience and Remote Sensing Symposium (IGARSS), 2012 IEEE International*, Munich, Germany, 2012, pp. 3146–3149. (Cited on page 36.)

[92] J.-M. Beaulieu and R. Touzi, "Segmentation of textured polarimetric SAR scenes by likelihood approximation," *IEEE Transactions on Geoscience and Remote Sensing*, vol. 42, no. 10, pp. 2063–2072, Oct 2004. (Cited on page 37.)

[93] K. Ward, "Compound representation of high resolution sea clutter," *Electronics Letters*, vol. 17, no. 16, pp. 561–563, 1981. (Cited on pages 37, 75, and 90.)

[94] F. Gini and M. Greco, "Covariance matrix estimation for CFAR detection in correlated heavy tailed clutter," *Signal Processing*, vol. 82, no. 12, pp. 1847–1859, 2002. (Cited on pages 37 and 38.)

[95] F. Pascal, P. Forster, J. Ovarlez, and P. Larzabal, "Performance analysis of covariance matrix estimates in impulsive noise," *IEEE Transactions on Signal Processing*, vol. 56, no. 6, pp. 2206–2217, 2008. (Cited on pages 37 and 38.)

[96] A. E. Koudou, C. Ley *et al.*, "Characterizations of GIG laws: A survey," *Probability Surveys*, vol. 11, pp. 161–176, 2014. (Cited on page 39.)

[97] S. Khan and R. Guida, "Application of Mellin-kind statistics to polarimetric G distribution for SAR data," *IEEE Transactions on Geoscience and Remote Sensing*, vol. 52, no. 6, pp. 3513–3528, June 2014. (Cited on pages 40 and 102.)

[98] W. Song, M. Li, P. Zhang, Y. Wu, L. Jia, and L. An, "The WGΓ distribution for multilook polarimetric SAR data and its application," *IEEE Geoscience and Remote Sensing Letters*, vol. 12, no. 10, pp. 2056–2060, Oct 2015. (Cited on pages 43 and 44.)

[99] Y. Bian and B. Mercer, "Multilook polarimetric SAR data probability density function estimation using a generalized form of multivariate K-distribution," *Remote Sensing Letters*, vol. 5, no. 7, pp. 682–691, 2014. (Cited on page 44.)

[100] T. Eltoft, S. N. Anfinsen, and A. P. Doulgeris, "A multitexture model for multilook polarimetric synthetic aperture radar data," *IEEE Transactions on Geoscience and Remote Sensing*, vol. 52, no. 5, pp. 2910–2919, 2014. (Cited on pages 45 and 46.)

[101] S. Frühwirth-Schnatter, *Finite mixture and Markov switching models*. Springer Science & Business Media, 2006. (Cited on pages 47, 48, and 61.)

[102] A. Jeffrey and D. Zwillinger, *Table of Integrals, Series, and Products (Seventh Edition)*, seventh edition ed. Boston: Academic Press, 2007. (Cited on pages 48, 49, 50, 56, 123, 128, 129, and 130.)

[103] C. Oliver, "Fundamental properties of high-resolution sideways-looking radar," in *IEE Proceedings F (Communications, Radar and Signal Processing)*, vol. 129, no. 6. IET, 1982, pp. 385–402. (Cited on pages 53 and 55.)

[104] E. Makhoul, C. López-Martínez, and A. Broquetas, "Exploiting polarimetric TerraSAR-X data for sea clutter characterization," *IEEE Transactions on Geoscience and Remote Sensing*, vol. PP, no. 99, pp. 1–15, 2015. (Cited on page 53.)

[105] R. A. Horn and C. R. Johnson, *Matrix analysis (Second Edition)*. Cambridge university press, 2013. (Cited on pages 54 and 60.)

[106] A. D. Poularikas, *Transforms and applications handbook*. CRC press, 2010. (Cited on page 55.)

[107] H. Wilf, *Generatingfunctionology: Third Edition*. CRC Press, 2005. (Cited on page 56.)

[108] L. Comtet, *Advanced Combinatorics: The Art of Finite and Infinite Expansions*. Springer Netherlands, 1974. (Cited on page 57.)

[109] A. Stuart and K. Ord, *Kendall's Advanced Theory of Statistics: Volume 1: Distribution Theory*, ser. Kendall's Advanced Theory of Statistics. Wiley, 2009, no. v. 1; v. 1994. (Cited on pages 57, 64, and 65.)

[110] S. N. Anfinsen, A. P. Doulgeris, and T. Eltoft, "Goodness-of-fit tests for multilook polarimetric radar data based on the Mellin transform," *IEEE Transactions on Geoscience and Remote Sensing*, vol. 49, no. 7, pp. 2764–2781, 2011. (Cited on pages 57, 59, 65, 105, and 122.)

[111] E. Weisstein, "k-statistic," From MathWorld–A Wolfram Web Resource, accessed: 2010-09-30. [Online]. Available: http://mathworld.wolfram.com/k-Statistic.html (Cited on pages 57 and 64.)

[112] F. Kenney and E. S. Keeping, *Mathematics of statistics - part one*. D. Van Nostrand Company, Inc Princeton,; New Jersey; Toronto; New York; London, 1951. (Cited on page 57.)

[113] B. Efron and R. Tibshirani, *An Introduction to the Bootstrap*, ser. Chapman & Hall/CRC Monographs on Statistics & Applied Probability. Taylor & Francis, 1994. (Cited on page 59.)

[114] L. N. Singh and G. R. Dattatreya, "Estimation of the hyperexponential density with applications in sensor networks," *International Journal of Distributed Sensor Networks*, vol. 3, no. 3, pp. 311–330, 2007. (Cited on page 61.)

[115] A. Mathai, "Storage capacity of a dam with gamma type inputs," *Annals of the Institute of Statistical Mathematics*, vol. 34, no. 1, pp. 591–597, 1982. (Cited on page 61.)

[116] E. Cornelius Jr, "Identities for complete homogeneous symmetric polynomials," *JP J. Algebra Number Theory Appl*, vol. 21, pp. 109–116, 2011. (Cited on page 62.)

[117] I. G. Macdonald, *Symmetric functions and Hall polynomials*. Oxford university press, 1998. (Cited on page 62.)

[118] I. P. David and B. Sukhatme, "On the bias and mean square error of the ratio estimator," *Journal of the American Statistical Association*, vol. 69, no. 346, pp. 464–466, 1974. (Cited on page 63.)

[119] G. Van Kempen and L. Van Vliet, "Mean and variance of ratio estimators used in fluorescence ratio imaging," *Cytometry*, vol. 39, no. 4, pp. 300–305, 2000. (Cited on page 63.)

[120] S. N. Anfinsen, A. P. Doulgeris, and T. Eltoft, "Estimation of the equivalent number of looks in polarimetric synthetic aperture radar imagery," *IEEE Transactions on Geoscience and Remote Sensing*, vol. 47, no. 11, pp. 3795–3809, Nov 2009. (Cited on pages 71 and 95.)

[121] L. Tao, C. Hao-gui, X. Ze-min, and G. Jun, "Texture-invariant estimation of equivalent number of looks based on trace moments in polarimetric radar imagery," *Geoscience and Remote Sensing Letters, IEEE*, vol. 11, no. 6, pp. 1129–1133, June 2014. (Cited on page 71.)

[122] E. Jakeman, "On the statistics of K-distributed noise," *Journal of Physics A: Mathematical and General*, vol. 13, no. 1, pp. 31–48, 1980. (Cited on pages 75 and 78.)

[123] F. T. Ulaby, F. Kouyate, B. Brisco, and T. L. Williams, "Textural infornation in SAR images," *IEEE Transactions on Geoscience and Remote Sensing*, vol. 24, no. 2, pp. 235–245, 1986. (Cited on page 75.)

[124] J. R. Taylor, *Scattering theory: the quantum theory of nonrelativistic collisions*. Courier Dover Publications, 2012. (Cited on pages 76 and 78.)

[125] E. Jakeman and K. D. Ridley, *Modeling fluctuations in scattered waves*. CRC Press, 2006. (Cited on pages 76, 77, and 78.)

[126] J. W. Goodman, "Speckle with a finite number of steps," *Applied Optics*, vol. 47, no. 4, pp. A111–A118, Feb 2008. [Online]. Available: http://ao.osa.org/abstract.cfm?URI=ao-47-4-A111 (Cited on pages 79, 81, 82, 84, and 86.)

[127] E. Jakeman, "Speckle statistics with a small number of scatterers," *Optical Engineering*, vol. 23, no. 4, pp. 234 453–234 453, 1984. (Cited on page 79.)

[128] S. N. Anfinsen, "Statistical unmixing of SAR images," Munin Open Research Archive, University of Tromsø– The Arctic University of Norway, Tromsø, Norway, Tech. Rep., Feb. 2016. [Online]. Available: http://hdl.handle.net/10037/8425 (Cited on page 79.)

[129] J. W. Goodman, *Speckle phenomena in optics: theory and applications*. Roberts and Company Publishers, 2007. (Cited on page 81.)

[130] J. W. Goodman and E. G. Rawson, "Statistics of modal noise in fibers: a case of constrained speckle," *Optics Letters*, vol. 6, no. 7, pp. 324–326, 1981. (Cited on page 82.)

[131] S. Magnussen, "An algorithm for generating positively correlated beta-distributed random variables with known marginal distributions and a specified correlation," *Computational statistics & data analysis*, vol. 46, no. 2, pp. 397–406, 2004. (Cited on page 82.)

[132] C. T. d. S. Dias, A. Samaranayaka, and B. Manly, "On the use of correlated beta random variables with animal population modelling," *ecological modelling*, vol. 215, no. 4, pp. 293–300, 2008. (Cited on page 82.)

[133] Y. Delignon and W. Pieczynski, "Modeling non-Rayleigh speckle distribution in SAR images," *IEEE Transactions on Geoscience and Remote Sensing*, vol. 40, no. 6, pp. 1430–1435, 2002. (Cited on pages 84 and 85.)

[134] G. Di Martino, A. Iodice, D. Riccio, and G. Ruello, "Equivalent number of scatterers for SAR speckle modeling," *IEEE Transactions on Geoscience and Remote Sensing*, vol. 52, no. 5, pp. 2555–2564, 2014. (Cited on page 89.)

[135] L. Pipia, X. Fabregas, A. Aguasca, and C. López-Martínez, "Polarimetric temporal analysis of urban environments with a ground-based SAR," *Geoscience and Remote Sensing, IEEE Transactions on*, vol. 51, no. 4, pp. 2343–2360, 2013. (Cited on page 98.)

[136] Y. Delignon, R. Garello, and A. Hillion, "Etude statistique d'images SAR de la surface de la mer," in *13?Colloque sur le traitement du signal et des images, FRA, 1991*. GRETSI, Groupe d'Etudes du Traitement du Signal et des Images, 1991. (Cited on page 102.)

[137] I. Hajnsek, E. Pottier, and S. R. Cloude, "Inversion of surface parameters from polarimetric SAR," *IEEE Transactions on Geoscience and Remote Sensing*, vol. 41, no. 4, pp. 727–744, 2003. (Cited on page 107.)

List of Publications

Journal Articles

J1 **X. Deng**, C. López-Martínez and E. M. Varona, "A Physical Analysis of Polarimetric SAR Data Statistical Models," *IEEE Transactions on Geoscience and Remote Sensing*, vol. 54, no. 5, pp. 3035-3048, May 2016.

J2 **X. Deng** and C. López-Martínez, "Higher Order Statistics for Texture Analysis and Physical Interpretation of Polarimetric SAR Data," *IEEE Geoscience and Remote Sensing Letters*, vol.13, no.7, pp.912-916, July 2016.

J3 **X. Deng** and C. López-Martínez, "On the Use of the l_2-Norm for Texture Analysis of Polarimetric SAR Data," *IEEE Transactions on Geoscience and Remote Sensing*, accepted.

J4 A. Alonso-González, C. López-Martínez, P. Salembier and **X. Deng**, "Bilateral distance based filtering for polarimetric SAR data". *Remote Sensing*, 5(11), pp.5620-5641, 2013.

J5 G. Sheng, W. Yang, **X. Deng**, C. He, Y. Cao and H. Sun, "Coastline detection in synthetic aperture radar (SAR) images by integrating watershed transformation and controllable gradient vector flow (GVF) snake model," *IEEE Journal of Oceanic Engineering*, 37(3), pp.375-383, 2012.

Conference Papers

C1 **X. Deng**, C. López-Martínez, "Analysis of texture distributions of polarimetric SAR data," *IGARSS 2015, Milan, Italy*, pp. 3802-3805.

C2 **X. Deng**, C. López-Martínez, "A Physical Explanation of Texture for Polarimetric SAR Data," *PolinSAR 2015, Frascati, Italy.*

C3 **X. Deng**, C. López-Martínez, "Statistical Analysis of Polarimetric SAR Data Based on The Random Walk Model," *GOLD 2015, Barcelona, Spain.*

C4 **X. Deng**, C. López-Martínez, "The Use of the L_2-Norm for the Analysis of Texture on PolSAR Data," *EUSAR 2016, Hamburg, Germany.*